# 論文 / 著書情報
# Article / Book Information

| | |
|---|---|
| 題目(和文) | |
| Title(English) | Mode-evolution-based integrated magneto-optical isolators and circulators on silicon platforms |
| 著者(和文) | Shuyuan Liu |
| Author(English) | Shuyuan Liu |
| 出典(和文) | 学位:博士(学術),<br>学位授与機関:東京工業大学,<br>報告番号:甲第12587号,<br>授与年月日:2023年9月22日,<br>学位の種別:課程博士,<br>審査員:庄司 雄哉,植之原 裕行,中川 茂,宮本 智之,西山 伸彦,齊藤 晋聖 |
| Citation(English) | Degree:Doctor (Academic),<br>Conferring organization: Tokyo Institute of Technology,<br>Report number:甲第12587号,<br>Conferred date:2023/9/22,<br>Degree Type:Course doctor,<br>Examiner:,,,,, |
| 学位種別(和文) | 博士論文 |
| Type(English) | Doctoral Thesis |

# Mode-evolution-based integrated magneto-optical isolators and circulators on silicon platforms

by

Shuyuan Liu

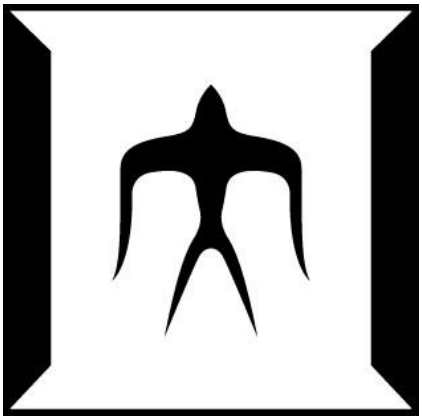

Department of Electrical and Electronic Engineering

School of Engineering

Tokyo Institute of Technology

**Doctoral Dissertation**

Supervisor: Associate professor Yuya Shoji

**July 2023**

# Catalogue

# Chapter I

# Introduction

## 1.1 Introduction

Microelectronics technology has transformed electronic components from discrete to integrated, whose integration density and performance have essentially followed "Moore's Law" for decades. However, as fabrication sizes approach physical limits, it becomes difficult to further increase the integration density and performance of electronic components by an order of magnitude [1]. Simultaneously, the proliferation of mobile electronic devices and Internet of Things technology has led people to exchange real-time data with databases distributed around the world almost all the time, and the enormous amount of data poses great challenges not only to long-distance wired and wireless communication technologies but also to the interconnection on-chip and inter-chips [2]. Traditional integrated circuit technology, which uses only electronics as the information carrier, cannot meet the current application requirements [3].

In recent decades, the optical communication system has attracted broad research interest as an effective means for solving the above challenge [4]. An optical communication system not only has a high transmission speed and a large bandwidth but also has no Joule heat loss [5]. With the development of optical communication systems, miniaturization of optical components; integration on chips; realization of wideband and high-speed integrated optical modules; and use in optical communication and optical interconnection are the research direction of new-generation communication systems. ***Silicon photonics*** came into being [6].

Silicon photonics has developed rapidly in recent years, and optical components such as photodetectors, optical modulators, wavelength division multiplexing, and mode multiplexing devices, *et al.* have already completed high-performance

integration on silicon platforms [7-10]. However, nonreciprocal optical components represented by optical circulators and optical isolators have not yet been effectively integrated. As the “missing link” in the photonics integrated circuits (PICs), the integration of nonreciprocal components is of great significance to realize the complex functions of PICs [11].

## 1.2 Nonreciprocal optical devices

Nonreciprocal optical devices are the key devices of optical systems. Taking an optical isolator as an example, its main function is to prevent the reflected light in the light path from entering the resonation cavity of the laser source or amplifier and to suppress intensity noise and phase noise in the system [12]. At present, optical isolators are widely used in optical fiber communication systems such as backbone networks, metropolitan area networks, and access networks, playing an irreplaceable role [13].

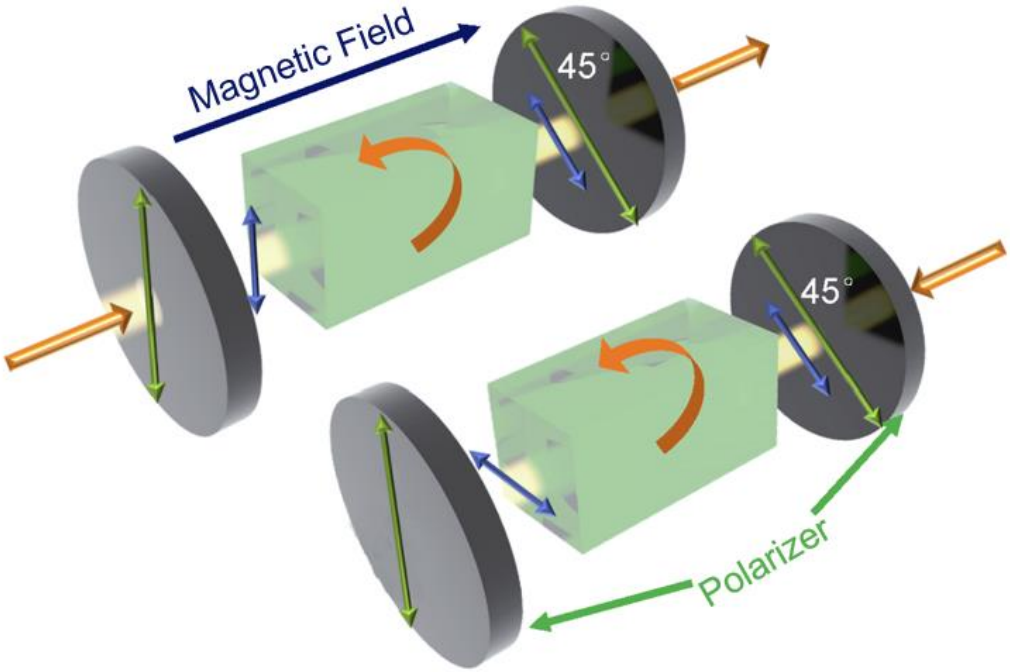


Fig.1-1 Schematic of an MO isolator based on Faraday rotation [15].

Currently, commercially available nonreciprocal optical devices are mainly

designed based on the magneto-optical (MO) Faraday rotation (FR) effect of MO materials, such as rare-earth iron garnet (RIG), *e.g.*, the widely used discrete MO isolators as shown in Fig.1-1 [14,15]. In such a device, the FR effect in a magnetic medium will rotate the polarization direction of the incident linear polarized light by 45° in the forward propagation, and then propagate through a 45° polarizer at the output side. And for the reflected light, the polarization direction instead of returning to the polarization direction of the incident light but will continue to rotate 45° and be orthogonal to the polarizer at the input side, thereby achieving isolation operation [16]. The key component of this device is a RIG crystal that is grown by liquid phase epitaxy (LPE) on gadolinium gallium garnet (GGG) substrates [17,18]. Since it is necessary to employ a RIG film with a thickness of several hundred microns to achieve the rotation of 45°, the material fabrication process is difficult and costly [19,20].

In recent years, with the development of silicon photonics technology, the optical communication and optical interconnection system has gradually developed towards PICs with miniaturized, low cost, and high performance. There is an urgent need to achieve integrated, low-cost, and high-performance nonreciprocal devices on silicon platforms. Decades of international research have been carried out, but this problem has not been completely overcome. The main difficulties in this area of research lie in the following three aspects:

(1) Difficult to integrate high-crystallized MO materials on a silicon platform. Lattice mismatch (yttrium iron garnet (YIG): 12.4 Å, Si: 5.4 Å) leads to the poor crystallinity of MO materials on a silicon substrate, which leads to weaker MO effects and higher material absorption.

(2) Difficult to compatibly process. MO materials require high growth and annealing temperature, leading to poor temperature compatibility with other on-chip devices during back-end integration.

(3) Difficult to employ the FR effect in waveguide-integrated devices. Because of the different propagation constants of transverse electric (TE) and transverse magnetic (TM) modes in a waveguide, *i.e.*, the birefringence. An optical waveguide, however long, cannot achieve a rotation of 45°. Although the integration of MO

FR effect devices can be integrated by quasi-phase-matching design, the processing is difficult, and the performance of the devices is not good as that of the discrete devices [21,22].

In recent years, some non-magnetic solutions such as nonlinear effects and dynamic modulation have been reported, but several limitations such as device bandwidth, power consumption, dynamic reciprocity, *et al.* led to a certain distance from the application [23-28], the integrated nonreciprocal devices based on the MO ***nonreciprocal phase shift*** (NRPS) effect have been considered the most promising technical approach to industrialization [29,30]. Herein, we will discuss the integrated nonreciprocal devices based on the NRPS effect from three aspects: MO materials, integration technology, and device design.

## 1.3 Magnetic garnet

Magnetic garnet is a high figure of merit (FoM) medium with excellent magnetic and optical properties in the infrared communication band, which has advantages such as high Curie temperature, strong MO effect, and low optical absorption loss [31]. Therefore, it is suitable for designing and processing high-performance nonreciprocal integrated devices.

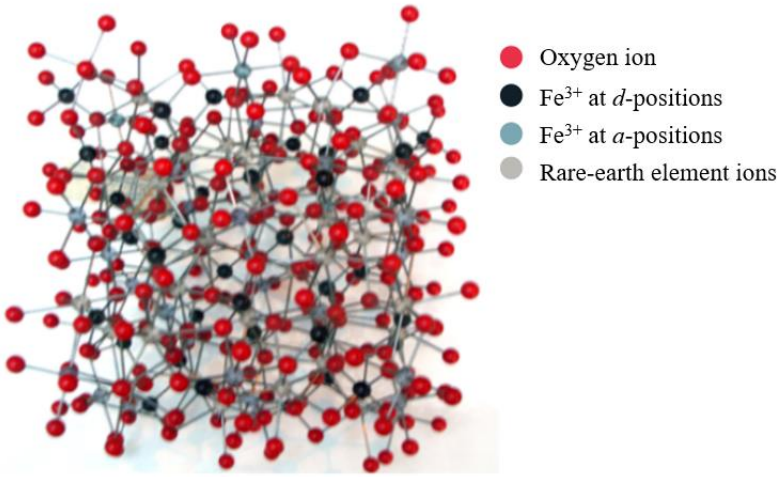


Fig.1-2 Unit cell structure of magnetic garnet.

The magnetic garnet unit cell structure is shown in Fig.1-2. One unit cell consists of eight $R_3Fe_5O_{12}$ unit structures. Lattice structures are composed of oxygen ions

forming three different interstices: tetrahedron (*d*), octahedron (*a*), and dodecahedron (*c*). Due to the large radii, the $R^{3+}$ ions occupy the *c*-position, while the $Fe^{3+}$ ions occupy the *a*- and *d*- positions. Since the $Fe^{3+}$ at *d*- and *a*-positions are superexchanged by oxygen ions, their magnetic moments are arranged in opposite directions and the final net magnetic moment is the same as one of the $Fe^{3+}$ ion at *d*-position, so magnetic garnets should belong to ferrimagnetic materials [32]. The optical absorption of the RIG material in the 1310 nm and 1550 nm communication bands is very small because the absorption wavelength of the $Fe^{3+}$ electron dipole transition in the material is around a wavelength of 900 nm. However, the MO effect of most used RIG material, *e.g.*, YIG is very weak, so it is necessary to dope cerium elements to enhance the MO effect [33]. Cerium-substituted yttrium iron garnet (Ce:YIG) is doped with $Ce^{3+}$ elements to occupy dodecahedral interstices in the lattice and form $Ce_xY_{3-x}Fe_5O_{12}$ phase. As the $Ce^{3+}$ ratio increases, the MO effect of the material will increase accordingly. However, since the radius of $Ce^{3+}$ ions is larger than that of $Y^{3+}$ ions, excessive cerium-doping leads to the direct combination of cerium with oxygen to form a more stable but non-magneto-optical $CeO_2$ phase [34]. Therefore, proper cerium doping ratio is the key to obtain high-performance Ce:YIG films, and the Ce:YIG has a higher MO effect when the cerium ratio x is about 1~1.5 (as shown in Figs.1-3 (a) and (b)) [35].

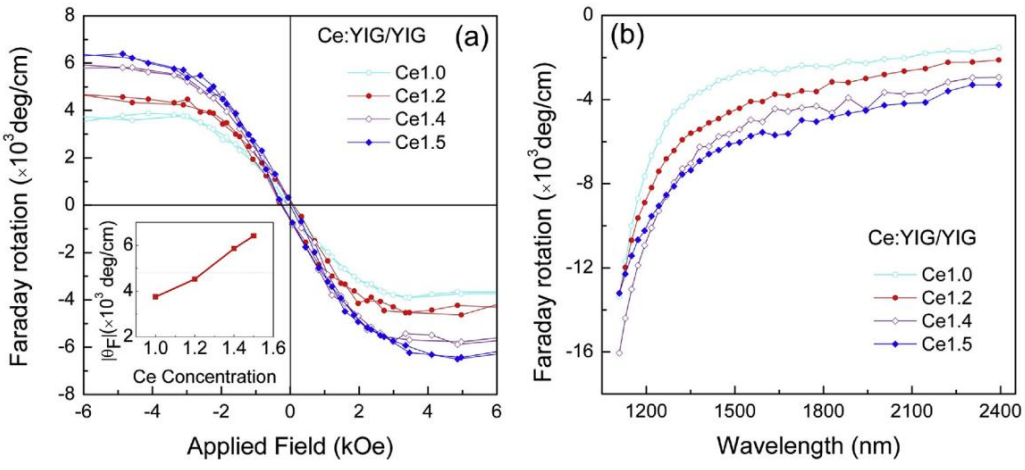


Fig.1-3 (a) Faraday rotation of Ce:YIG thin films with different cerium concentrations deposited at a wavelength of 1550 nm. (b) Faraday rotation spectra [35].

Magnetic garnets are used in the design of nonreciprocal optical devices because their unique permittivity tensor breaks the time-reversal symmetry, allowing light to have different responses of intensities, phases, or polarizations when propagating in forward and backward directions. When it is magnetized by applying an external magnetic field along the z-axis, its permittivity tensor can be written as:

$$\tilde{\varepsilon} = \begin{bmatrix} \varepsilon_{xx} & i\gamma & 0 \\ -i\gamma & \varepsilon_{yy} & 0 \\ 0 & 0 & \varepsilon_{zz} \end{bmatrix} \tag{1-1}$$

where $\varepsilon$ and $\gamma$ is diagonal and non-diagonal elements of the complex permittivity tensor, respectively. Its asymmetric permittivity tensor breaks the Lorentz reciprocity of the optical system, and its strong MO effect and low optical absorption loss also led it widely used in the design of nonreciprocal optical devices [36,37].

Ce:YIG material is commonly epitaxially grown on GGG substrate because GGG and Ce:YIG have the same lattice type and similar lattice constant, so it can achieve high crystallinity, and the properties of Ce:YIG will be almost comparable to single crystal material [38].

Besides LPE, the preparation techniques of Ce:YIG thin films include pulsed laser deposition (PLD), and sputtering. For applications where the thickness of Ce:YIG is thinner ( < 1 μm), we usually choose to sputter, which is the most suitable technology for industrial mass production [39-42]. But if we need to integrate magnetic garnets on a silicon-based platform, the integration technology will be more complicated.

## 1.4 Integration technology

Due to the lattice constant and thermal expansion coefficient mismatch between Ce:YIG and the silicon substrate, directly depositing Ce:YIG on the silicon substrate will cause the material to be very difficult to crystallize, which will weaken the MO effect and increase the optical loss. To overcome this problem, two technical approaches have been used for silicon-based integration of MO materials, *i.e.*, wafer bonding and monolithic integration [43,44].

### 1.4.1 Wafer bonding

The basic idea of the wafer bonding technology approach is to directly bond the

high-performance Ce:YIG grown on the garnet substrate on the silicon waveguides or devices. The bonded $Ce_1Y_2Fe_5O_{12}$ usually has a high FR of -4500 °/cm at a wavelength of 1550 nm. But due to the relatively fixed distribution of MO materials and structure of MO waveguides, MO waveguides prepared based on wafer bonding can only support NRPS of TM mode; and MO materials need to cover a large on-chip area, which increases the footprint and absorption loss [45].

According to different bonding methods, wafer bonding can be cataloged into direct bonding and benzocyclobutene (BCB) bonding [46,47]. Direct bonding is to treat the bonding surface with nitrogen or oxygen plasma to make it rough, and then heat and pressurize the bonding surface in a vacuum environment as shown in Fig.1-4 (a) [48]. Although the roughness of the waveguide surface is usually < 1 nm, it will still increase the propagation loss of the MO waveguide to > 60 dB/cm [49]; and the uneven edge of the Ce:YIG chip will also cause additional reflection loss. However, the silicon substrate only needs to be heated to ~200 °C during the bonding process, so the temperature compatibility is good.

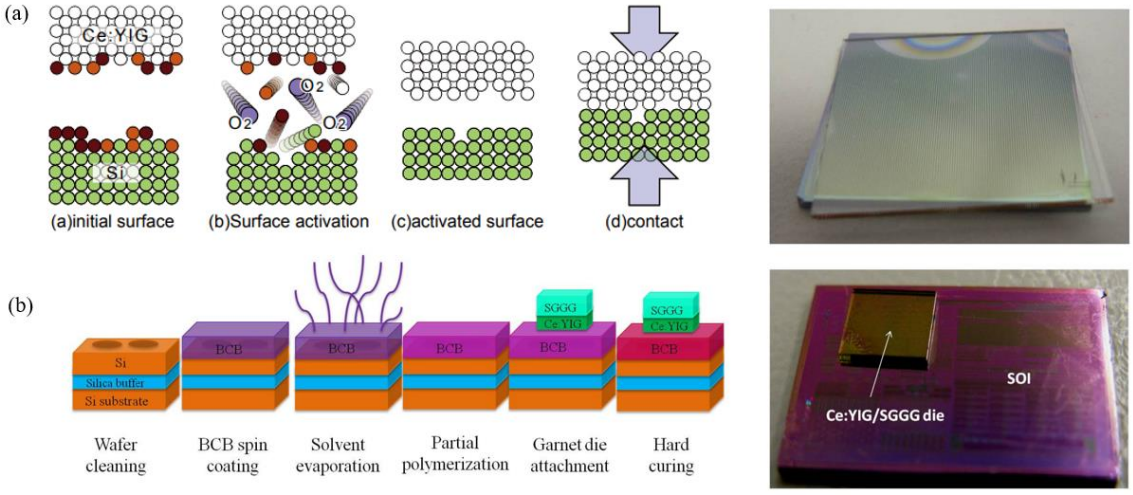


Fig.1-4 Schematic diagram of the processing flow and device photos of (a) direct bonding and (b) BCB bonding [48,50].

BCB bonding is to spin-coat a layer of BCB on the surface of the silicon substrate, and after placing the Ce:YIG chips the whole sample is heated to ~250 °C for curing as shown in Fig.1-4 (b) [50]. So BCB bonding also has the advantages of high material merit and good temperature compatibility. However, since Ce:YIG is not in direct

contact with the topwall of the waveguide, only a few energy of modes can be coupled to the MO material, resulting in a low NRPS.

### 1.4.2 Monolithic integration

Although MO materials growing directly on silicon substrates usually have poor crystallinity due to differences in lattice constants and thermal expansion coefficients, promoting the crystallization of RIG materials by introducing a seed layer can also obtain a material FoM exceeding 45 °/dB [51], which basically meets the requirements for the preparation of nonreciprocal devices.

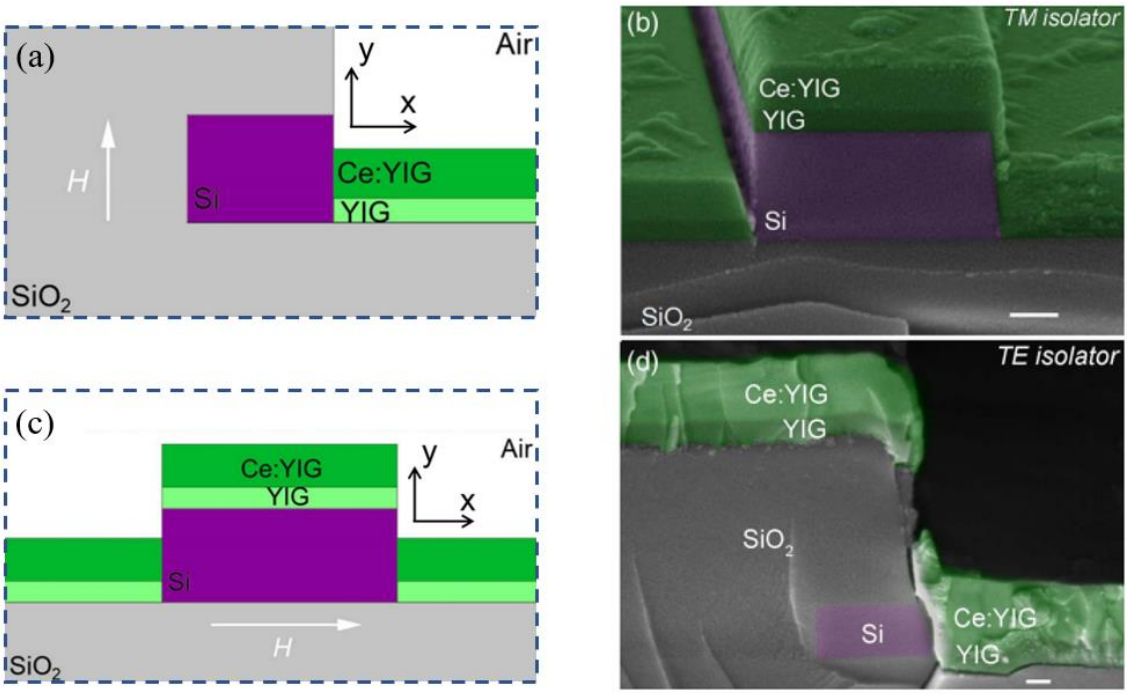


Fig.1-5 (a) TE-mode and (c) TM-mode MO waveguide. Cross-sectional SEM images of the MO waveguides for (b) TE-mode and (d) TM-mode [53].

YIG is usually used as a seed layer for Ce:YIG deposition. A layer of YIG with a thickness of ~50 nm is first deposited on silicon waveguides or devices by sputtering or PLD, and then a Ce:YIG MO material layer is deposited on the polycrystalline seed layer. To form a polycrystalline phase, the substrate needs to be annealed at a maximum temperature of ~850 °C [52]. The final deposited $Ce_1Y_2Fe_5O_{12}$ usually has an FR of only -3000 °/cm. And since the FR of YIG of ~150 °/cm has an opposite sign

to that of Ce:YIG, the NRPS of the propagation mode in the MO waveguide is slightly lower than that of the wafer-bonded fabricated waveguide. By adjusting the doping ratio of the cerium, a higher MO effect can be achieved, but the propagation loss of the modes will also increase accordingly [53].

Although the high annealing temperature of monolithic integration makes it difficult to integrate at the back end of the fabrication process, the devices prepared by this technical approach have their unique advantages. On the one hand, monolithic integration is more suitable for large-scale chip production; on the other hand, the free distribution of material deposition also makes the structure of MO waveguides more flexible. As shown in Figs. 1-5 (a) and (b), we can realize TE mode NRPS by controlling the distribution of MO materials only at one sidewall of the waveguide; and TM mode NRPS by depositing the MO material on the topwall of the waveguide as shown in Figs. 1-5 (c) and (d), which bring more possibilities for the design of nonreciprocal devices.

## 1.5 Silicon-based integrated magneto-optical devices based on nonreciprocal phase shift effect

After the integrated MO waveguide is magnetized by applying a magnetic field orthogonal to the propagation direction, the propagation constants of the fundamental modes will degenerate when propagating in forward and backward directions, *i.e.*, NRPS. Since the MO effect is relatively weak, usually the devices need a longer MO waveguide to cumulate phase shift to meet the application requirements of nonreciprocal transmission. The integrated MO nonreciprocal devices designed and prepared based on this idea can be roughly divided into three categories: Mach-Zehnder interferometer (MZI) type, microring resonator (MRR) type, and multimode interferometer (MMI) type. The most important device indicators for MO isolators are insertion loss (IL) and isolation ratio (IR), which is also known as crosstalk in circulators. So, in this section, we will focus on the performance, advantages, and disadvantages of various types of devices.

### 1.5.1 Mach-Zehnder interferometer type

As one of the most common integrated optical components, MZI is an excellent structure for MO nonreciprocal devices design. The classic structure of the silicon-

based TM-mode MZI MO device is shown in Fig.1-6 (a) [54]. The device consists of two 3 dB couplers at both ends of the device and nonreciprocal waveguides and reciprocal waveguides on two arms. 3 dB couplers can be realized by 1×2 or 2×2 MMI, directional coupler (DC), or mode evolution structure. After the opposite magnetic field is applied to the two arms, the TM fundamental mode propagation constants in the nonreciprocal waveguides of the two arms will become different. By designing the appropriate length of the MO waveguide, the overall NRPS is designed to be $0.5\pi$; while the reciprocal phase shift (RPS) between the two arms is $2n\pi + 0.5\pi$. When propagating in the forward direction, the overall phase difference between the two-arms light is $\varphi_{\mathrm{RPS}} + \varphi_{NRPS} = 2n\pi + 0.5\pi - 0.5\pi = 2n\pi$, so the light at the output 3 dB coupler will interfere constructively; while in the backward propagation, the overall phase difference becomes $\varphi_{\mathrm{RPS}} + \varphi_{NRPS} = 2n\pi + 0.5\pi + 0.5\pi = (2n+1)\pi$ due to the NRPS effect, the light eventually interferes and couple to other output port as a circulator or cladding mode for evanescence as an isolator to achieve nonreciprocal transmission operation.

The performance of MZI-type devices is strongly related to the reciprocal waveguide length. On the one hand, the asymmetric loss caused by the reciprocal waveguide will cause the energy of the two arms to incomplete extinction, which restricts the IR of the device. On the other hand, the smaller the length of the reciprocal waveguide, the wider the free spectral range (FSR) will be, and the operation bandwidth of the device will also be improved.

The fabrication of silicon-based MZI MO isolators based on wafer bonding (as shown in Fig.1-6 (b)) was reported in 2008 [43]. Because of the absorption of the MO material which covered a large on-chip area and the mode mismatch at the edge of the Ce:YIG chip, the IL of this kind of device was still not ideal (> 9 dB) [54]. And due to the limitations of the MO waveguide structure mentioned above, the device could only operate under TM-polarized light input. The TE mode isolation could be realized by series polarization rotators (PRs) as shown in Fig.1-6 (c), but the additional PRs would introduce IL to restrict the overall performance of the device, the reported IL of TE mode device was ~ 20 dB [55].

In recent years, with the development of silicon-based magnetic garnet growth technology, the high-performance silicon-based MZI-type MO isolator fabricated by the monolithic integration technology approach was also experimentally confirmed in

2019 [53]. The device structure is shown in Fig.1-6 (d). Since monolithic integration could more flexibly design the distribution of MO materials, the device employed an S-shaped waveguide design and an asymmetric window structure distribution enabling the device to work under a unidirectional magnetic field; and for TE mode devices, the sidewall deposition was adopted to directly realize TE mode NRPS, but due to the poor crystallinity of sidewall materials, as shown in Fig.1-6 (f) the device performance (IL~9 dB) still had a certain gap with TM mode (IL~5 dB) devices as shown in Fig.1-6 (e).

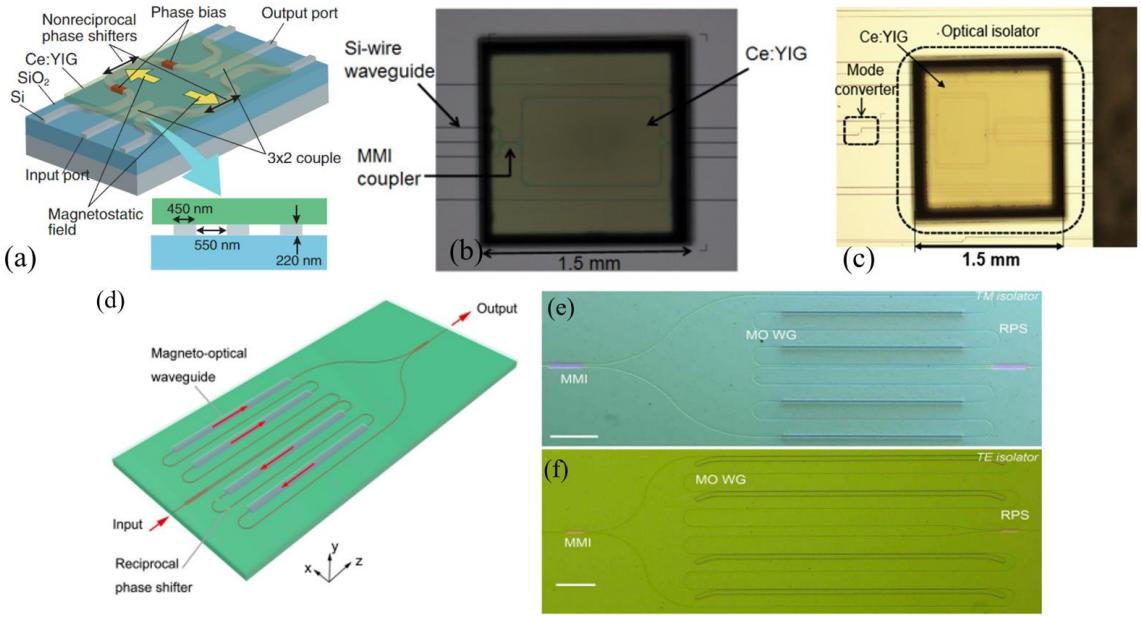


Fig.1-6 (a) Schematic diagram of MZI MO isolator structure. Micrographs of (b) TM mode (c) TE mode MZI MO isolator fabricated by wafer bonding. (d) Schematic diagram of the MZI MO isolator fabricated by monolithic integration, and Micrographs of (e) TM mode and (f) TE mode devices [37,53-55].

In addition to the improvement of device performance, magnetic field integration has also been experimentally proven in recent years. Since some MO nonreciprocal devices cannot work under unidirectional magnetic fields, the integration of magnetic fields is also an indispensable requirement for device miniaturization. The traditional solution could realize the integration of the magnetic field by depositing Au wires or

coils as shown in Fig.1-8 (a) [56,57], but this design required additional energy consumption and heat generation. Another better magnetic field integration solution was integrated self-holding permanent magnets as shown in Fig.1-8 (b) [58], passive magnetic field integration had been reported by processing bar magnets with strong shape anisotropy.

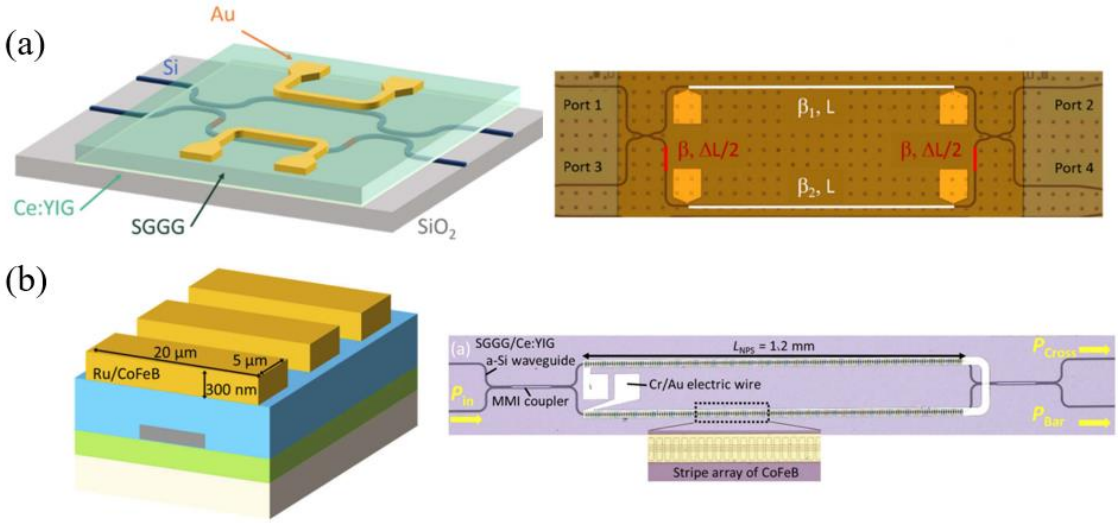


Fig.1-7 Magnetic field integration scheme: (a) Electronic control. (b) self-holding permanent magnet [56,58].

### 1.5.2 Microring resonator type

MRRs are another important component for wavelength filtering in PICs. The structure of the silicon-based MRR-based MO nonreciprocal devices is shown in Fig.1-8 (a). The device consists of an input/output straight waveguide and a microring. Under critical coupling conditions, the optical energy at the resonant wavelength will be coupled into the microring and cannot be output from the straight waveguide; due to the existence of NRPS in the microring formed by the MO waveguide, the light rotating clockwise (CW) and counterclockwise (CCW) in the microring will have different resonant wavelengths, so at the resonant wavelength of the backward transmission, the device can operate as an isolator.

The point of MRR device design is how to accumulate NRPS and how to achieve critical coupling conditions. Because of the limitation of wafer bonding accuracy, MO materials usually cover the entire microring. With the symmetrical structure of the microring, the device cannot accumulate NRPS of TM fundamental mode under a

unidirectional magnetic field, so a radial magnetic field needs to be applied; and for monolithic integration, the MO material can only be deposited on only one side of the microring, so there is no above-mentioned problem. The realization of the critical coupling can ensure that the device has a high IR and a large operating bandwidth, so the estimation of the transmission loss of the microring is an important step in the simulation design.

Because of the difficulty of magnetic field integration under the wafer bonding technology approach, the first silicon-based MRR MO isolator was prepared by a monolithic integration in 2011 [44], the unsatisfactory crystallization properties of the materials at that time, especially the MO materials on the sidewalls, resulting in the IL of the device was as high as 18.8 dB. At present, after material optimization, the IL of the MRR MO isolator was lower than 3 dB and the IR was greater than 40 dB, initially meeting the application requirements [59].

With the development of magnetic field integration technology, silicon-based MRR MO isolators fabricated by wafer bonding had been also reported as shown in Figs. 1-8 (b) and (c) [60]. The device had a high IR of ~32 dB, but because the input/output straight waveguide was covered by MO materials, resulting in a large amount of absorption loss, the overall IL of the TM device was ~10 dB; and the IL of the TE mode device is slightly lower because most of the straight waveguide propagates in the TE mode, but it was still 6.5 dB [61].

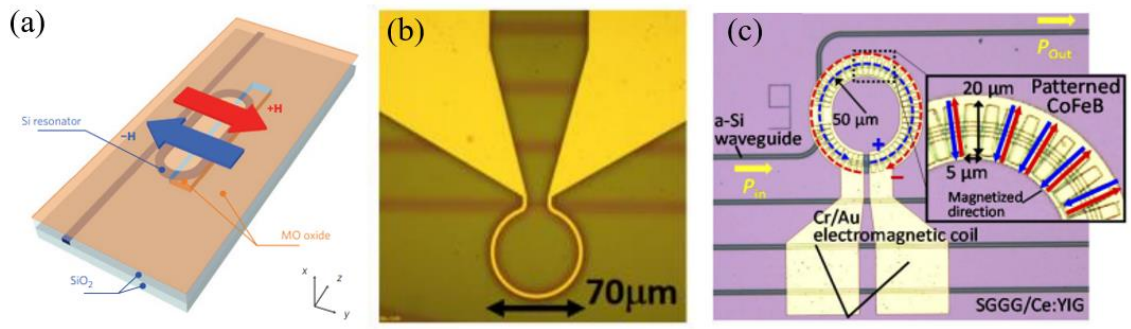


Fig.1-8 (a) Monolithically integrated MRR MO isolator. The MRR MO isolator prepared by wafer bonding technology, the magnetic field was integrated by (b) Au wire and (c) permanent magnet [44,58,60].

Additionally, since a long length of microring is needed to accumulate NRPS, the

FSR of the spectrum is usually small, resulting in MRR nonreciprocal devices that can only be used in narrow-band working situations.

### 1.5.3 Multimode interferometer type

For MMI-type MO nonreciprocal devices, its working principle is like that of MZI-type devices, but the incident light is not equally divided into two arms, it excites the two different modes: different polarizations or different orders of the same polarization, in the multimode MO waveguide with equal energy. Utilizing NRPS of one or two modes to achieve a phase difference between modes of $2n\pi$ in forward transmission and $(2n\pm1)\pi$ in backward transmission to achieve nonreciprocal operation.

Since the interference process involves two different modes, the difference in intermode IL and dispersion between the two modes will affect the performance of the device. The difference in IL will cause an incomplete extinction, resulting in a low IR; and the difference in dispersion will affect the FSR of the device and thus restrict the working bandwidth.

The TE-mode silicon-based MMI MO circulator based on the sandwich structure as shown in Fig.1-9 (a) had unique advantages: the device had a one-dimensional structure and the NRPS of two-mode signs are opposite (push-pull structure) [62,63]. However, the crystallization of the MO in the slot guide was poor, the device performance has not been proved experimentally.

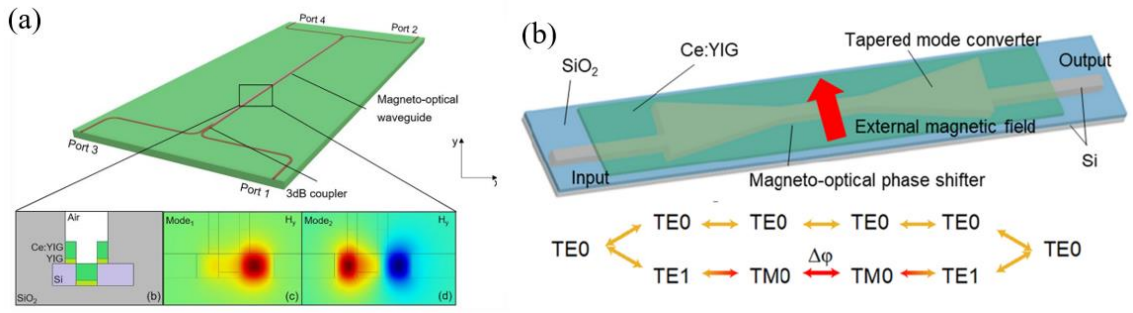


Fig.1-9 (a) Sandwich structure TE MMI MO circulator. (b) MMI MO isolator based on half-mode conversion [63,64].

Another type of silicon-based nonreciprocal MMI device based on the half-mode conversion is an excellent solution to the difficulty in realizing nonreciprocal devices

in TE mode under the wafer bonding fabrication process. The device structure is shown in Fig.1-9 (b) [64]. The device had a quasi-one-dimensional structure that greatly reduces the on-chip footprint; the mode excitation structure at both ends of the device equally divided the incident $TE_0$ mode into $TE_0$ and $TE_1$ modes in the multimode waveguide. After the $TE_1$ mode was efficiently converted to $TM_0$ mode by the mode converter, the TE mode nonreciprocal transmission could be achieved by employing the NRPS of the TM mode. But the IR of the device is only 16 dB due to IL imbalance between modes.

## 1.6 Silicon-based integrated polarization-independence nonreciprocal devices

Although the various nonreciprocal devices introduced in the previous section have excellent performance, they can only work under a single polarization (TE or TM). In optical paths, especially in optical fibers for inter-chip communication, the polarization states of reflected light and noise signals are often random, so polarization-independent integrated nonreciprocal devices are also in demand [65].

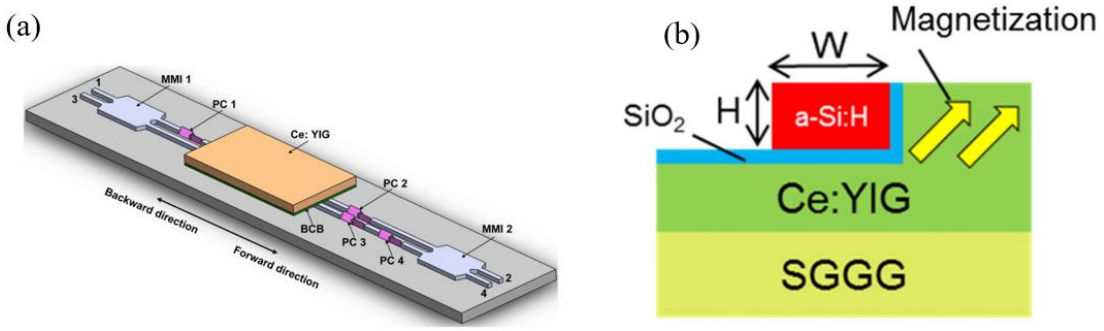


Fig.1-10 Integrated polarization-independent MO nonreciprocal device designed based on (a) 90° PRs and (b) sidewall deposition [67,69].

There have been two reported designs of polarization-independence integrated MO nonreciprocal devices based on the NRPS effect: one is shown in Fig.1-10 (a) [66], and the device was realized by polarization-independent 3 dB couplers and 90° PRs. After the incident light is divided into two arms, the light of one arm underwent 90° polarization rotation, and the light of the two arms was respectively in $TE_0$ and $TM_0$ modes. After propagating through the nonreciprocal phase shifter to accumulate

the required NRPS from TM mode, lights would return to the original polarization by PRs and interferes for output. The devices based on this design have been realized on the III-V semiconductor platform in 2021 [67], but since the realization of PCs required a waveguide with a triangular cross-section to support the TE-TM-hybrid mode, therefore, the anisotropic etching, which was incompatible with the CMOS process, was inevitably involved in the device preparation process, so there was a process compatibility problem in the integration on the silicon-based platform. And the IL of the device was extremely high due to the mode mismatch at the end faces of PRs.

Another design was to deposit MO materials on the sidewall and topwall of the waveguide at the same time as shown in Fig.1-10 (b) [68,69]. After applying an oblique magnetic field, the MO waveguide could support NRPS of both TE and TM modes. However, due to the poor crystallinity of the sidewall materials mentioned above, and the difficulty of designing the NRPS of the TE and TM modes to the same value, resulting in the mismatch of the length of the nonreciprocal phase shifter under different polarized light inputs, the devices based on this design have not yet been experimentally demonstrated.

## 1.7 Research motivation and dissertation organization

By summarizing the existing State-of-Art devices as shown in Table 1-1, we can find several unsolved problems of the existing silicon-based integrated MO nonreciprocal devices:

(1) The performance of TE mode devices still has a performance gap with that of TM devices. Especially in terms of IL due to the additional PRs.

(2) The IL of the wafer bonding technology is always higher than that of monolithic integration. This is partly due to the MO material covering the extra waveguide; and the coupling loss caused by the mode mismatching at the edge of the bonded chips.

(3) Some devices, especially MRR-type devices prepared by wafer bonding, still cannot work under a unidirectional magnetic field, so additional steps are required to integrate the magnetic field.

(4) Silicon-based integrated polarization-independent MO devices have not been experimentally demonstrated.

Based on the above challenges, we will give the research motivation.

Table.1-1 Summary of silicon-based integrated MO device performance

| Type | Year | IL (dB) | IR (dB) | Polarization | Integration |
|---|---|---|---|---|---|
| MZI | 2012[50] | 9.7 | 25 | TM | BCB Bonding |
| | 2014[54] | 13 | 30 | TM | Direct Bonding |
| | 2016[55] | 33.4 | 26.7 | TE | Direct Bonding |
| | 2017[56] | 9 | 29 | TM | Direct Bonding |
| | 2019[57] | 18 | 30 | TE | Direct Bonding |
| | 2019[53] | 5 | 30 | TM | Monolithic |
| | 2019[53] | 9 | 30 | TE | Monolithic |
| MRR | 2011[44] | 18.8 | 19.5 | TM | Monolithic |
| | 2016[60] | 10 | 32 | TM | Direct Bonding |
| | 2018[61] | 6.5 | 25 | TE | Direct Bonding |
| | 2018[59] | 3 | 40 | TM | Monolithic(GeSbSe) |
| | 2019[53] | 11.5 | 20 | TM | Monolithic |
| MMI | 2018[64] | 3.4 (Ideal) | 16 | TE | Direct Bonding |

### 1.7.1 Research motivation

Considering the temperature compatibility we will integrate magnetic garnet on silicon platforms by wafer bonding and realize TE mode isolation by employing NRPS of TM mode. So, achieving efficient mode conversion between TE modes and TM modes will be the key to reducing the IL of TE mode nonreciprocal devices. In this work, we will make extensive use of mode couplers and mode converters based on ***mode evolution***.

As for the MRR device to work under a unidirectional magnetic field, we will design an asymmetric microring structure to realize the overall NRPS accumulation.

Finally, after we realize the IL and structural optimization of TE mode devices, we will further realize the design and experiment of the polarization-independent nonreciprocal device. So, the main goals are therefore as follows:

Step 1: Under the premise of a unidirectional magnetic field, improve the performance of existing broadband and narrowband TE mode devices, especially IL, by novel mode evolution structure designs.

Step 2: Based on the above results, design and fabricate silicon-based integrated polarization-independent MO nonreciprocal devices.

### 1.7.2 Organization of dissertation

This thesis will be divided into six chapters as shown in Fig.1-11. In the first chapter, we have discussed the characteristics of magnetic garnets and silicon-based integration technologies; the current status and problems of silicon-based integrated nonreciprocal MO devices; finally gave the research motivation for reducing IL, simplifying magnetic field integration and realizing polarization-independent devices.

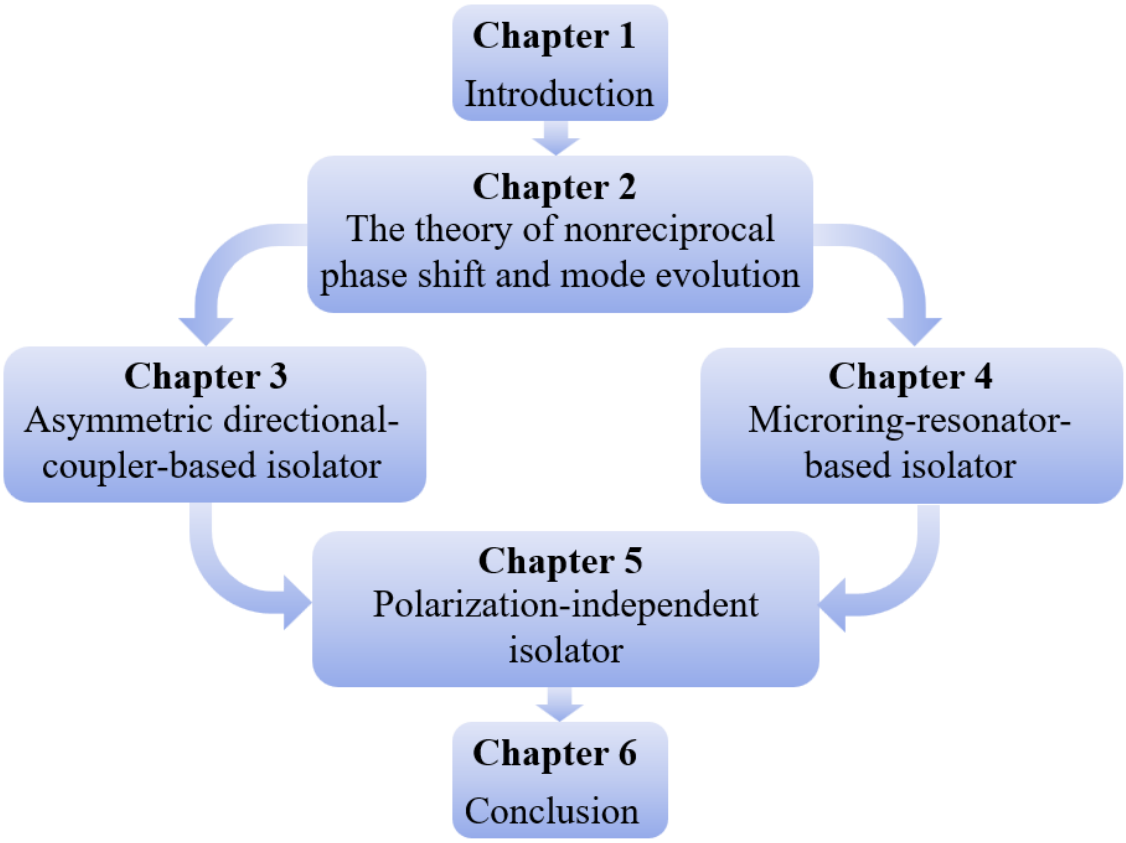


Fig.1-11 Organization of this dissertation.

In Chapter 2, we will explain in detail the device design principles, mainly

including the principle of mode evolution and nonreciprocal phase shift.

Chapters 3 and 4 are our optimized design of TE mode MMI and MRR devices. By designing high-efficiency mode converters based on mode evolution, we realize extremely low-loss TE mode MO isolators and circulators; and the devices can work under a unidirectional magnetic field. In the experiment, the device exhibits excellent performance.

In Chapter 5, we successfully designed a novel waveguide-integrated polarization-independent MO isolator based on the design inspiration of the devices in Chapters 3 and 4. The device adopts a CMOS-compatible fabrication process and has excellent performance. The proposed device is a milestone as the first silicon-based integrated MO nonreciprocal device.

In the last chapter, we will briefly summarize all the work and look forward to future research directions.

## References


1. Williams R.S., "What's next?[The end of Moore's law]." *Computing in Science & Engineering* 19.2 (2017): 7-13. DOI: 10.1109/MCSE.2017.31
2. Margalit N., Xiang C., Bowers S.M., Bjorlin A., Blum R. and Bowers J.E., "Perspective on the future of silicon photonics and electronics." *Applied Physics Letters* 118.22 (2021): 220501. DOI: 10.1063/5.0050117
3. Jones N., "How to stop data centres from gobbling up the world's electricity." *Nature* 561.7722 (2018): 163-166. DOI: 10.1038/d41586-018-06610-y
4. Miller S.E., "Integrated optics: An introduction." *The Bell System Technical Journal* 48.7 (1969): 2059-2069. DOI: 10.1002/j.1538-7305.1969.tb01165.x
5. Kimerling L.C., "Silicon microphotonics." *Applied Surface Science* 159 (2000): 8-13. DOI: 10.1016/S0169-4332(00)00126-4
6. Nagarajan R., Joyner C.H., Schneider R.P., Bostak J.S., Butrie T., Dentai A.G., Dominic V.G., Evans P.W., Kato M., Kauffman M. and Lambert D.J., "Large-scale photonic integrated circuits." *IEEE Journal of Selected Topics in Quantum Electronics* 11.1 (2005): 50-65. DOI: 10.1109/JSTQE.2004.841721
7. Yang W., Chen J., Zhang Y., Zhang Y., He J. and Fang, X., "Silicon-compatible photodetectors: trends to monolithically integrate photosensors with chip technology." *Advanced Functional Materials* 29.18 (2019): 1808182. DOI: 10.1002/adfm.201808182
8. Reed G.T., Mashanovich G., Gardes F.Y. and Thomson D., "Silicon optical modulators." *Nature Photonics* 4.8 (2010): 518-526. DOI: 10.1038/nphoton.2010.179
9. Dong P., "Silicon photonic integrated circuits for wavelength-division multiplexing applications." *IEEE Journal of Selected Topics in Quantum Electronics* 22.6 (2016): 370-378. DOI: 10.1109/JSTQE.2016.2575358
10. Dai D., Wang J. and He S., "Silicon multimode photonic integrated devices for on-chip mode-division-multiplexed optical interconnects (invited review)." *Progress In Electromagnetics Research* 143 (2013): 773-819. DOI: 10.2528/PIER13111003
11. Hu J., Zhang Y., Du Q., Wang C., Fakhrul T., Zhang Y., Liu S., Deng L., Goncalves C., Blanco C. Richardson K., Huang D., Pintus P., Bowers J.E., Ross C.A. and Bi L., "Filling in the missing link: monolithic optical isolators on silicon with high performance, broadband operation, and polarization diversity." *Photonic and Phononic Properties of Engineered Nanostructures X*. Vol. 11289. SPIE, 2020. DOI: 10.1117/12.2553949
12. Jalas D., Petrov A., Eich M., Freude W., Fan S., Yu Z., Baets R., Popović M., Melloni A., Joannopoulos J.D. and Vanwolleghem M., "What is-and what is not-an optical isolator." *Nature Photonics* 7.8 (2013): 579-582. DOI: 10.1038/nphoton.2013.185
13. Shoji Y. and Mizumoto T., "Waveguide magneto-optical devices for photonics integrated circuits." *Optical Materials Express* 8.8 (2018): 2387-2394. DOI: 10.1364/OME.8.002387

14. Bi L., Hu J., Jiang P., Kim H.S., Kim D.H., Onbasli M.C., Dionne G.F. and Ross C.A., "Magneto-optical thin films for on-chip monolithic integration of non-reciprocal photonic devices." *Materials* 6.11 (2013): 5094-5117. DOI: 10.3390/ma6115094
15. Bi L., "Materials for nonreciprocal photonics." *MRS Bulletin* 43.6 (2018): 408-412. DOI: 10.1557/mrs.2018.120
16. Fischer S., "The Faraday optical isolator." *Journal of Optical Communications* 8.1 (1987): 18-21. DOI: 10.1515/JOC.1987.8.1.18
17. Henry R., Besser P., Heinz D. and Mee J., "Ferromagnetic resonance properties of LPE YIG films." *IEEE Transactions on Magnetics* 9.3 (1973): 535-537. DOI: 10.1109/TMAG.1973.1067610
18. Rao Y., Zhang D., Zhang H., Jin L., Yang Q., Zhong Z., Li M., Hong C. and Ma B., "Thickness dependence of magnetic properties in submicron yttrium iron garnet films." *Journal of Physics D: Applied Physics* 51.43 (2018): 435001. DOI: 10.1088/1361-6463/aade43
19. Linares R.C., McGraw R.B. and Schroeder J.B., "Growth and properties of yttrium iron garnet single-crystal films."*Journal of Applied Physics* 36.9 (1965): 2884-2886. DOI: 10.1063/1.1714599
20. Rao Y., Zhang H., Yang Q., Zhang D., Jin L., Ma B. and Wu Y., "Liquid phase epitaxy magnetic garnet films and their applications." *Chinese Physics B* 27.8 (2018): 086701. DOI: 10.1088/1674-1056/27/8/086701
21. Zhang C., Dulal P., Stadler B.J. and Hutchings D.C., "Monolithically-integrated TE-mode 1D silicon-on-insulator isolators using seedlayer-free garnet." *Scientific Reports* 7.1 (2017): 5820. DOI: s41598-017-06043-z
22. Srinivasan K., Zhang C., Dulal P., Radu C., Gage T.E., Hutchings D.C. and Stadler B.J., "High-gyrotropy seedlayer-free Ce: TbIG for monolithic laser-matched SOI optical isolators." *ACS Photonics* 6.10 (2019): 2455-2461. DOI: 10.1021/acsphotonics.9b00707
23. Fan L., Wang J., Varghese L.T., Shen H., Niu B., Xuan Y., Weiner A.M. and Qi M., "An all-silicon passive optical diode." *Science* 335.6067 (2012): 447-450. DOI: 10.1126/science.1214383
24. Peng B., Özdemir Ş.K., Lei F., Monifi F., Gianfreda M., Long G., Fan S., Nori F., Bender C.M. and Yang L., "Parity–time-symmetric whispering-gallery microcavities." *Nature Physics* 10.5 (2014): 394-398. DOI: 10.1038/nphys2927
25. Doerr C.R., Chen L. and Vermeulen D., "Silicon photonics broadband modulation-based isolator." *Optics Express* 22.4 (2014): 4493-4498. DOI: 10.1364/OE.22.004493
26. Sounas D.L. and Alù A., "Non-reciprocal photonics based on time modulation." *Nature Photonics* 11.12 (2017): 774-783. DOI: 10.1038/s41566-017-0051-x

27. Sohn D.B., Kim S. and Bahl G., "Time-reversal symmetry breaking with acoustic pumping of nanophotonic circuits." *Nature Photonics* 12.2 (2018): 91-97. DOI: 10.1038/s41566-017-0075-2
28. Shi Y., Yu Z. and Fan S., "Limitations of nonlinear optical isolators due to dynamic reciprocity." *Nature Photonics* 9.6 (2015): 388-392. DOI: 10.1038/nphoton.2015.79
29. Shoji Y., Miura K., and Mizumoto T., "Optical nonreciprocal devices based on magneto-optical phase shift in silicon photonics." *Journal of Optics* 18.1 (2015): 013001. DOI: 10.1088/2040-8978/18/1/013001
30. Mizumoto T., Baets R. and Bowers J.E., "Optical nonreciprocal devices for silicon photonics using wafer-bonded magneto-optical garnet materials." *MRS Bulletin* 43.6 (2018): 419-424. DOI: 10.1557/mrs.2018.125
31. Fakhrul T., Tazlaru S., Beran L., Zhang Y., Veis M. and Ross C.A., "Magneto-optical Bi: YIG films with high figure of merit for nonreciprocal photonics." *Advanced Optical Materials* 7.13 (2019): 1900056. DOI: 10.1002/adom.201900056
32. Gilleo M.A. and Geller S., "Magnetic and Crystallographic Properties of Substituted Yttrium-Iron Garnet, $3Y_2O_3{\cdot}xM_2O_3{\cdot}(5-x)Fe_2O_3$." *Physical Review* 110.1 (1958): 73. DOI: 10.1103/PhysRev.110.73
33. Wang C.T., Liang X.F., Zhang Y., Liang X., Zhu Y.P., Qin J., Gao Y., Peng B., Sun N.X. and Bi L., "Controlling the magnetic anisotropy in epitaxial $Y_3Fe_5O_{12}$ films by manganese doping." *Physical Review B* 96.22 (2017): 224403. DOI: 10.1103/PhysRevB.96.224403
34. Liang X., Xie J., Deng L. and Bi L., "First principles calculation on the magnetic, optical properties and oxygen vacancy effect of $Ce_xY_{3-x}Fe_5O_{12}$." *Applied Physics Letters* 106.5 (2015): 052401. DOI: 10.1063/1.4907413
35. Zhang Y., Wang C., Liang X., Peng B., Lu H., Zhou P., Zhang L., Xie J., Deng L., Zahradnik M., Beran L., Kucere M., Veis M., Ross C.A. and Bi L., "Enhanced magneto-optical effect in $Y_{1.5}Ce_{1.5}Fe_5O_{12}$ thin films deposited on silicon by pulsed laser deposition." *Journal of Alloys and Compounds* 703 (2017): 591-599. DOI: 10.1016/j.jallcom.2017.01.315
36. Ren S., Yan W., Feng L., Chen Y., Wu Y., Qi X., Liu X., Cheng Y., Xu B., Deng L., Guo G., Bi L. and Ren X., "Single-Photon nonreciprocity with an integrated magneto-optical isolator." *Laser & Photonics Reviews* 16.5 (2022): 2100595. DOI: 10.1002/lpor.202100595
37. Shoji Y., Ito M., Shirato Y. and Mizumoto T., "MZI optical isolator with Si-wire waveguides by surface-activated direct bonding." *Optics Express* 20.16 (2012): 18440-18448. DOI: 10.1364/OE.20.018440
38. Schmidt G., Hauser C., Trempler P., Paleschke M. and Papaioannou E.T., "Ultra thin films of yttrium iron garnet with very low damping: A review." *Physica Status Solidi (b)* 257.7 (2020): 1900644. DOI: 10.1002/pssb.201900644
39. Yang F. and Hammel P.C., "FMR-driven spin pumping in $Y_3Fe_5O_{12}$-based structures." *Journal of Physics D: Applied Physics* 51.25 (2018): 253001. DOI: 10.1088/1361-6463/aac249

40. Bai H., Zhan X., Li G., Su J., Zhu Z., Zhang Y., Zhu T. and Cai J., "Characterization of YIG thin films and vacuum annealing effect by polarized neutron reflectometry and magnetotransport measurements." *Applied Physics Letters* 115.18 (2019): 182401. DOI: 10.1063/1.5124832
41. Liu T., Chang H., Vlaminck V., Sun Y., Kabatek M., Hoffmann A., Deng L. and Wu M., "Ferromagnetic resonance of sputtered yttrium iron garnet nanometer films." *Journal of Applied Physics* 115.17 (2014): 17A501. DOI: 10.1063/1.4852135
42. Ding J., Liu T., Chang H. and Wu M., "Sputtering growth of low-damping yttrium-iron-garnet thin films." *IEEE Magnetics Letters* 11 (2020): 1-5. DOI: 10.1109/LMAG.2020.2989687
43. Shoji Y., Mizumoto T., Yokoi H., Hsieh I.W. and Osgood Jr R.M., "Magneto-optical isolator with silicon waveguides fabricated by direct bonding." *Applied physics Letters* 92.7 (2008): 071117. DOI: 10.1063/1.2884855
44. Bi L., Hu J., Jiang P., Kim D.H., Dionne G.F., Kimerling L.C. and Ross C.A., "On-chip optical isolation in monolithically integrated non-reciprocal optical resonators." *Nature Photonics* 5.12 (2011): 758-762. DOI: 10.1038/nphoton.2011.270
45. Shoji Y., Shirato Y. and Mizumoto T., "Silicon Mach–Zehnder interferometer optical isolator having 8 nm bandwidth for over 20 dB isolation." *Japanese Journal of Applied Physics* 53.2 (2014): 022202. DOI: 10.7567/JJAP.53.022202
46. Shoji Y. and Mizumoto T., "Silicon waveguide optical isolator with directly bonded magneto-optical garnet." *Applied Sciences* 9.3 (2019): 609. DOI: 10.3390/app9030609
47. Ghosh S., Keyvaninia S., Van Roy W., Mizumoto T., Roelkens G. and Baets R., "Adhesively bonded Ce:YIG/SOI integrated optical circulator." *Optics Letters* 38.6 (2013): 965-967. DOI: 10.1364/OL.38.000965
48. Mizumoto T., Shoji Y. and Takei R., "Direct wafer bonding and its application to waveguide optical isolators." *Materials* 5.5 (2012): 985-1004. DOI: 10.3390/ma5050985
49. Takei R., Yoshida K. and Mizumoto T., "Effects of wafer precleaning and plasma irradiation to wafer surfaces on plasma-assisted surface-activated direct bonding." *Japanese Journal of Applied Physics* 49.8R (2010): 086204. DOI: 10.1143/JJAP.49.086204
50. Ghosh S., Keyvavinia S., Van Roy W., Mizumoto T., Roelkens, G. and Baets R., "Ce: YIG/Silicon-on-Insulator waveguide optical isolator realized by adhesive bonding." *Optics Express* 20.2 (2012): 1839-1848. DOI: 10.1364/OE.20.001839
51. Fakhrul T., Tazlaru S., Khurana B., Beran L., Bauer J., Vančík M., Marchese A., Tsotsos E., Kučera M., Zhang Y., Veis M. and Ross C.A., "High figure of merit magneto-optical Ce-and Bi-substituted terbium iron garnet films integrated on Si." *Advanced Optical Materials* 9.16 (2021): 2100512. DOI: 10.1002/adom.202100512

52. Onbasli M.C., Goto T., Sun X., Huynh N. and Ross C.A., "Integration of bulk-quality thin film magneto-optical cerium-doped yttrium iron garnet on silicon nitride photonic substrates." *Optics Express* 22.21 (2014): 25183-25192. DOI: 10.1364/OE.22.025183
53. Zhang Y., Du Q., Wang C., Fakhrul T., Liu S., Deng L., Huang D., Pintus P., Bowers J.E., Ross C.A. Hu J. and Bi L., "Monolithic integration of broadband optical isolators for polarization-diverse silicon photonics." *Optica* 6.4 (2019): 473-478. DOI: 10.1364/OPTICA.6.000473
54. Shoji Y. and Mizumoto T., "Magneto-optical non-reciprocal devices in silicon photonics." *Science and Technology of Advanced Materials* (2014). DOI: 10.1088/1468-6996/15/1/014602
55. Shoji Y., Fujie A. and Mizumoto T., "Silicon waveguide optical isolator operating for TE mode input light." *IEEE Journal of Selected Topics in Quantum Electronics* 22.6 (2016): 264-270. DOI: 10.1109/JSTQE.2016.2574678
56. Huang D., Pintus P., Shoji Y., Morton P., Mizumoto T. and Bowers J.E., "Integrated broadband Ce:YIG/Si Mach–Zehnder optical isolators with over 100 nm tuning range." *Optics Letters* 42.23 (2017): 4901-4904. DOI: 10.1364/OL.42.004901
57. Pintus P., Huang D., Morton P.A., Shoji Y., Mizumoto T. and Bowers J.E., "Broadband TE optical isolators and circulators in silicon photonics through Ce: YIG bonding." *Journal of Lightwave Technology* 37.5 (2019): 1463-1473. DOI: 10.1109/JLT.2019.2896650
58. Murai T., Shoji Y., Nishiyama N. and Mizumoto T., "Nonvolatile magneto-optical switches integrated with a magnet stripe array." *Optics Express* 28.21 (2020): 31675-31685. DOI: 10.1364/OE.403129
59. Du Q., Wang C., Zhang Y., Zhang Y., Fakhrul T., Zhang W., Gonçalves C., Blanco C., Richardson K., Deng L. and Ross C.A., "Monolithic on-chip magneto-optical isolator with 3 dB insertion loss and 40 dB isolation ratio." *ACS Photonics* 5.12 (2018): 5010-5016. DOI: 10.1021/acsphotonics.8b01257
60. Huang D., Pintus P., Zhang C., Shoji Y., Mizumoto T. and Bowers J.E., "Electrically driven and thermally tunable integrated optical isolators for silicon photonics." *IEEE Journal of Selected Topics in Quantum Electronics* 22.6 (2016): 271-278. DOI: 10.1109/JSTQE.2016.2588778
61. Huang D., Pintus P. and Bowers J.E., "Towards heterogeneous integration of optical isolators and circulators with lasers on silicon." *Optical Materials Express* 8.9 (2018): 2471-2483. DOI: 10.1364/OME.8.002471
62. Shui K., Nie L., Zhang Y., Peng B., Xie J., Deng L. and Bi L., "Design of a compact waveguide optical isolator based on multimode interferometers using magneto-optical oxide thin films grown on silicon-on-insulator substrates." *Optics Express* 24.12 (2016): 12856-12867. DOI: 10.1364/OE.24.012856
63. Yang Y., Liu S., Yan W., Zhang Y., Qin J., Deng L. and Bi L., "Design for a TE mode magneto-optical circulator based on asymmetric silicon slot waveguides." *2021 5th*

*IEEE Electron Devices Technology & Manufacturing Conference (EDTM)*. IEEE, 2021. DOI: 10.1109/EDTM50988.2021.9420887

64. Yamaguchi R., Shoji Y. and Mizumoto T., "Low-loss waveguide optical isolator with tapered mode converter and magneto-optical phase shifter for TE mode input." *Optics Express* 26.16 (2018): 21271-21278. DOI: 10.1364/OE.26.021271
65. Zhao W., Liu R., Peng Y., Yi X., Chen H. and Dai D., "High-performance silicon polarization switch based on a Mach–Zehnder interferometer integrated with polarization-dependent mode converters." *Nanophotonics* 11.10 (2022): 2293-2301. DOI: 10.1515/nanoph-2022-0022
66. Shoji Y., Hsieh I.W., Osgood R.M. and Mizumoto T., "Polarization-independent magneto-optical waveguide isolator using TM-mode nonreciprocal phase shift." *Journal of Lightwave Technology* 25.10 (2007): 3108-3113. DOI: 10.1109/JLT.2007.904940
67. Ma R., Reniers S., Shoji Y., Mizumoto T., Williams K., Jiao Y. and van der Tol J., "Integrated polarization-independent optical isolators and circulators on an InP membrane on silicon platform." *Optica* 8.12 (2021): 1654-1661. DOI: 10.1364/OPTICA.443097
68. Fujita J., Levy M., Osgood R.M., Wilkens L. and Dotsch H., "Polarization-independent waveguide optical isolator based on nonreciprocal phase shift." *IEEE Photonics Technology Letters* 12.11 (2000): 1510-1512. DOI: 10.1109/68.887722
69. Ishida E., Miura K., Shoji Y., Yokoi H., Mizumoto T., Nishiyama N. and Arai S., "Amorphous-Si waveguide on a garnet magneto-optical isolator with a TE mode nonreciprocal phase shift." *Optics Express* 25.1 (2017): 452-462. DOI: 10.1364/OE.25.000452

# Chapter II

# The theory of nonreciprocal phase shift and mode evolution

## 2.1 Introduction

In this dissertation, the NRPS effect and mode evolution are crucial principles in the device design.

Although the NRPS effect can be explained as the magneto-optical Kerr effect (MOKE) in ray optics, with the development of wave optics and simulation software, the NRPS calculation method based on perturbation theory is more universal now.

Mode evolution is an excellent design scheme for mode converters and mode couplers. Its characteristics of wide bandwidth, low insertion loss, and high mode conversion efficiency, *et al.* make it suitable for IL optimization.

In this chapter, we will discuss the determination of the off-diagonal elements of the permittivity tensor and the NRPS calculation theory assisted by simulation software; and discuss the principles of mode evolution from the coupled-mode theory.

## 2.2 Magneto-optical effect and nonreciprocal phase shift

When light interacts with a magnetized MO material, one or more MO effect phenomena will occur, and the NRPS effect is the most used in the design of integrated nonreciprocal devices. In this section, we will deduce the working mechanism of the NRPS effect.

### 2.2.1 Off-diagonal elements of the permittivity tensor

To calculate the NRPS, we first need to determine the off-diagonal element of the permittivity tensor of the magnetic medium. At present, the laboratory usually

measures its value by testing the FR loop under different magnetic fields.

If a biased magnetic field was applied along the z-axis, then the material permittivity tensor can be expressed as [1]

$$\tilde{\varepsilon} = \begin{bmatrix} \varepsilon & i\gamma & 0 \\ -i\gamma & \varepsilon & 0 \\ 0 & 0 & \varepsilon \end{bmatrix}. \tag{2-1}$$

We assume that linearly polarized light also propagates in the MO material along the z-axis. The electric field components are

$$\vec{E} = \vec{r}E_0 e^{-ikz} = \begin{bmatrix} E_x \\ E_y \\ E_z \end{bmatrix}, \tag{2-2}$$

and the relationship of each field component can be written as

$$\begin{aligned} &\vec{k} \times \vec{H} = -\omega\varepsilon_0 \tilde{\varepsilon}\vec{E} \\ &\vec{k} \times \vec{E} = \omega\mu_0 \vec{H} \\ &\vec{k} \cdot \vec{H} = 0 \\ &\vec{k} \cdot \tilde{\varepsilon} \cdot \vec{E} = 0 \end{aligned}, \tag{2-3}$$

solve the dispersion relation

$$k^2\vec{E} - \vec{k}(\vec{k}\cdot\vec{E}) - k_0^2\tilde{\varepsilon}\cdot\vec{E} = \begin{bmatrix} k^2 - k_0^2\varepsilon & -ik_0^2\gamma & 0 \\ ik_0^2\gamma & k^2 - k_0^2\varepsilon & 0 \\ 0 & 0 & -k_0^2\varepsilon \end{bmatrix} \begin{bmatrix} E_x \\ E_y \\ E_z \end{bmatrix} = 0 \tag{2-4}$$

to

$$(k^2 - k_0^2\varepsilon)^2 - (k_0^2\gamma)^2 = 0, \tag{2-5}$$

$k$ can be calculated as

$$k_{\pm} = k_0\sqrt{\varepsilon \pm \gamma}\,. \tag{2-6}$$

Substituting the $k$ into Eq.2-4 can solve the electric field expression in the MO material

$$\begin{cases} (k^2 - k_0^2\varepsilon)E_x + ik_0^2\varepsilon E_y = 0 \\ -k_0^2\varepsilon E_z = 0 \end{cases} \tag{2-7}$$

to

$$\begin{cases} \dfrac{E_y}{E_x} = \dfrac{k_\pm^2 - k_0^2\varepsilon}{-ik_0^2\varepsilon} = \pm i \\ E_z = 0 \end{cases}. \tag{2-8}$$

Therefore, the eigenmodes propagating in the MO material are left-handed light and right-handed light, and the propagation constants are different. The electric field component are

$$\begin{aligned} \vec{E}_R &= (\vec{e}_x - i\vec{e}_y)E_0 e^{-ik_- z}, k_- = k_0\sqrt{(\varepsilon - \gamma)} \\ \vec{E}_L &= (\vec{e}_x + i\vec{e}_y)E_0 e^{-ik_+ z}, k_+ = k_0\sqrt{(\varepsilon + \gamma)} \end{aligned}. \tag{2-9}$$

In MO materials, the total electric field is the superposition of that of left-handed and right-handed light

$$\vec{E} = \vec{E}_R + \vec{E}_L = \vec{e}_x E_0(e^{-ik_+ z} + e^{-ik_- z}) + i\vec{e}_y E_0(e^{-ik_+ z} - e^{-ik_- z}), \tag{2-10}$$

then the polarization angle of the linear-polarized light varies with the propagation distance as

$$\tan^{-1}(\frac{E_y}{E_x}) = \frac{k_+ - k_-}{2} z = \theta_F z, \tag{2-11}$$

where $\theta_F$ is the FR coefficient, which means the Faraday rotation angle in a unit length. By testing the FR coefficient of the MO material, we can calculate the off-diagonal elements of the permittivity tensor matrix by

$$\gamma = \frac{2n\theta_F}{k_0}. \tag{2-12}$$

### 2.2.2 Magneto-optical nonreciprocal phase shift effect

After getting the permittivity tensor, the NRPS of the modes in the MO waveguide can be calculated. Taking the TM mode as an example, if the TM fundamental mode in the waveguide propagates along the z-axis, an external magnetic field needs to be applied along the x-axis to support an NRPS. At this condition, the permittivity tensor of the MO material is

$$\tilde{\varepsilon} = \begin{bmatrix} \varepsilon & 0 & 0 \\ 0 & \varepsilon & i\gamma \\ 0 & -i\gamma & \varepsilon \end{bmatrix}. \tag{2-13}$$

Bringing this into Maxwell's equations

$$\begin{aligned}
&\frac{\partial E_z}{\partial y}-\frac{\partial E_y}{\partial z}=-i\omega\mu_0 H_x \\
&\frac{\partial E_x}{\partial z}-\frac{\partial E_z}{\partial x}=-i\omega\mu_0 H_y \\
&\frac{\partial E_y}{\partial x}-\frac{\partial E_x}{\partial y}=-i\omega\mu_0 H_z \\
&\frac{\partial H_z}{\partial y}-\frac{\partial H_y}{\partial z}=i\omega\varepsilon_0\varepsilon E_x \\
&\frac{\partial H_x}{\partial z}-\frac{\partial H_z}{\partial x}=i\omega\varepsilon_0\varepsilon(E_y+i\gamma E_z) \\
&\frac{\partial H_y}{\partial x}-\frac{\partial H_x}{\partial y}=i\omega\varepsilon_0\varepsilon(E_z-i\gamma E_y)
\end{aligned} \quad . \tag{2-14}$$

The field components $\vec{E}$ and $\vec{H}$ can be solved by simulation software (such as COMSOL Multiphysics or Lumerical Mode Solution). The permittivity change from the MO effect can be regarded as a perturbation, and the NRPS value calculated by the perturbation theory [2,3]

$$NRPS_{TM}=\beta_{forward}-\beta_{backward}=\frac{2\omega\varepsilon_0}{P}\iint E^*\Delta\varepsilon E dxdy, \tag{2-15}$$

where $P$ is the power flow along the z-axis of the simulation cross-face as

$$P=\iint(E\times H^*+E^*\times H)_z dxdy, \tag{2-16}$$

and the perturbation $\Delta\varepsilon$ caused by the MO effect is

$$\Delta\varepsilon=\begin{bmatrix}0 & 0 & 0\\ 0 & 0 & i\gamma\\ 0 & -i\gamma & 0\end{bmatrix}. \tag{2-17}$$

Simultaneously, the TM mode electric field components can be simplified as

$$\vec{E}_{TM}=\begin{bmatrix}0\\ E_y\\ E_z\end{bmatrix}. \tag{2-18}$$

Simplify the simultaneous equations of Eqs.2-14, 2-15, 2-17, and 2-18 to get the NRPS of TM mode by

$$NRPS_{TM} = \frac{2\omega\varepsilon_0}{P}\iint \begin{bmatrix} 0 & E_y^* & E_z^* \end{bmatrix} \begin{bmatrix} 0 & 0 & 0 \\ 0 & 0 & i\gamma \\ 0 & -i\gamma & 0 \end{bmatrix} \begin{bmatrix} 0 \\ E_y \\ E_z \end{bmatrix} dxdy$$

$$= \frac{2\omega\varepsilon_0}{P}\iint 2\,\mathrm{Re}\left(i\gamma E_y^* E_z\right) dxdy \quad , \qquad (2\text{-}19)$$

$$= \frac{4\beta^{TM}}{\omega\varepsilon_0 P}\iint \frac{\gamma}{\varepsilon^2} H_x \partial_y H_x dxdy$$

where $\beta^{TM}$ is the propagation constant in an unmagnetized MO waveguide. Similarly for the TE mode, after we apply an external magnetic field along the y-axis, the perturbation of the permittivity is

$$\Delta\varepsilon = \begin{bmatrix} 0 & 0 & i\gamma \\ 0 & 0 & 0 \\ -i\gamma & 0 & 0 \end{bmatrix}, \qquad (2\text{-}20)$$

calculate the NRPS value of TE mode by

$$NRPS_{TE} = \frac{4\omega\varepsilon_0}{\beta^{TE} P}\iint \gamma E_x \partial_x E_x dxdy\,. \qquad (2\text{-}21)$$

Then we discuss the result. Firstly, because the integral term contains off-diagonal elements of the permittivity tensor $\gamma$, only the MO material region contributes to the integral. Assuming a MO waveguide structure prepared by wafer bonding as shown in Fig.2-1 (a), the waveguide height is 220 nm and the width is 500 nm. The TE and TM fundamental modes field distribution in the waveguide is solved by the finite element method (FEM) as shown in Figs.2-1 (b) and (c).

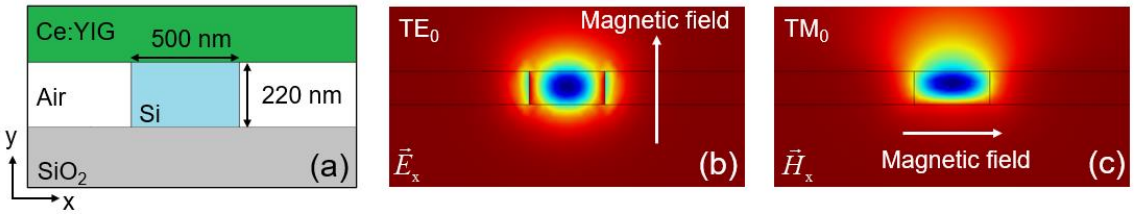


Fig.2-1 (a) Schematic diagram of the MO waveguide fabricated by wafer bonding. (b) $TE_0$ and (c) $TM_0$ mode field distributions

For the $TE_0$ mode, the integral term contains the gradient of $E_x$ along the x-axis. Due to the symmetry of the waveguide structure, the right half $\partial_x E_x$ is negative and

the left half $\partial_x E_x$ is positive, so the overall value cancels each other to 0. This explains why the TE mode MO waveguide needs to deposit MO materials on only one sidewall because in this way the $\partial_x E_x$ in the integral area will not cancel out. However, such a waveguide structure is difficult to achieve for the technical approach of wafer bonding.

For the $TM_0$ mode, the integral term contains the gradient of $H_x$ along the y-axis. Since only the integral area above the waveguide contributes to the NRPS, and the gradients are all negative, the overall NRPS can be achieved.

### 2.2.3 The figure of merit of a magneto-optical waveguide

Based on the discussion of NRPS calculation in the previous section, the NRPS of under different widths of MO waveguides can be calculated by simulation. Assume that the $\theta_F$ of the Ce:YIG used for bonding is -4500 °/cm, the calculated NRPS of $TM_0$ mode is shown in Fig.2-2 (a). As the mode filed distribution as shown in Fig.2-1 (c), the MO material region above the waveguide contributes more to the NRPS, so the NRPS value is low when the waveguide width is narrow; and if the waveguide is too wide to approach the multimode waveguide width, the $TM_0$ mode will hybridize with the $TE_1$ mode, and the TM mode ratio of the mode will decrease, so the NRPS will also decrease accordingly. So $TM_0$ mode has a maximum NRPS of 6.26 rad/mm when the waveguide width is ~ 690 nm.

For the FoM of a MO waveguide, we need to calculate its propagation loss first. Since the loss of the waveguide is mainly from the optical absorption loss of the materials, the confinement factor of in each layer of material is the key to calculating the propagation loss theoretically.

By assuming that material $m$ have a refractive index as $n_m + ik_m$, where the $k$ should be very small as the perturbation does not affect the mode distribution. While other materials have only the real part. Then the $n_{eff}$ of the mode can be simulated as:

$$n_{eff} = a_m + ib_m . \tag{2-22}$$

The confinement factor of the mode in the material $m$ is [4]

$$\Gamma_m = \frac{b_m}{k_m} . \tag{2-23}$$

The propagation loss of the mode is

$$\alpha = \sum_m \Gamma_m \alpha_m , \tag{2-24}$$

where $\alpha_m$ is the absorption loss of the material $m$. By simulation, the confinement factors of the $TM_0$ mode in different materials of the MO waveguide are shown in Fig.2-2 (b). As the waveguide width increases, the confinement factor in the Si layer gradually increases, while the confinement factor in the MO material layer gradually decreases. Since the absorption loss of MO materials is several orders of magnitude higher than that of other materials, the propagation loss of $TM_0$ mode decreases as the waveguide width becomes wider.

And the FoM of the $TM_0$ mode MO waveguide can be roughly calculated by

$$FoM = \frac{NRPS}{\Gamma_{Ce:YIG}} . \tag{2-25}$$

As shown in Fig.2-2 (c), within the width of a single-mode waveguide, the FoM increases with increasing width of the waveguide.

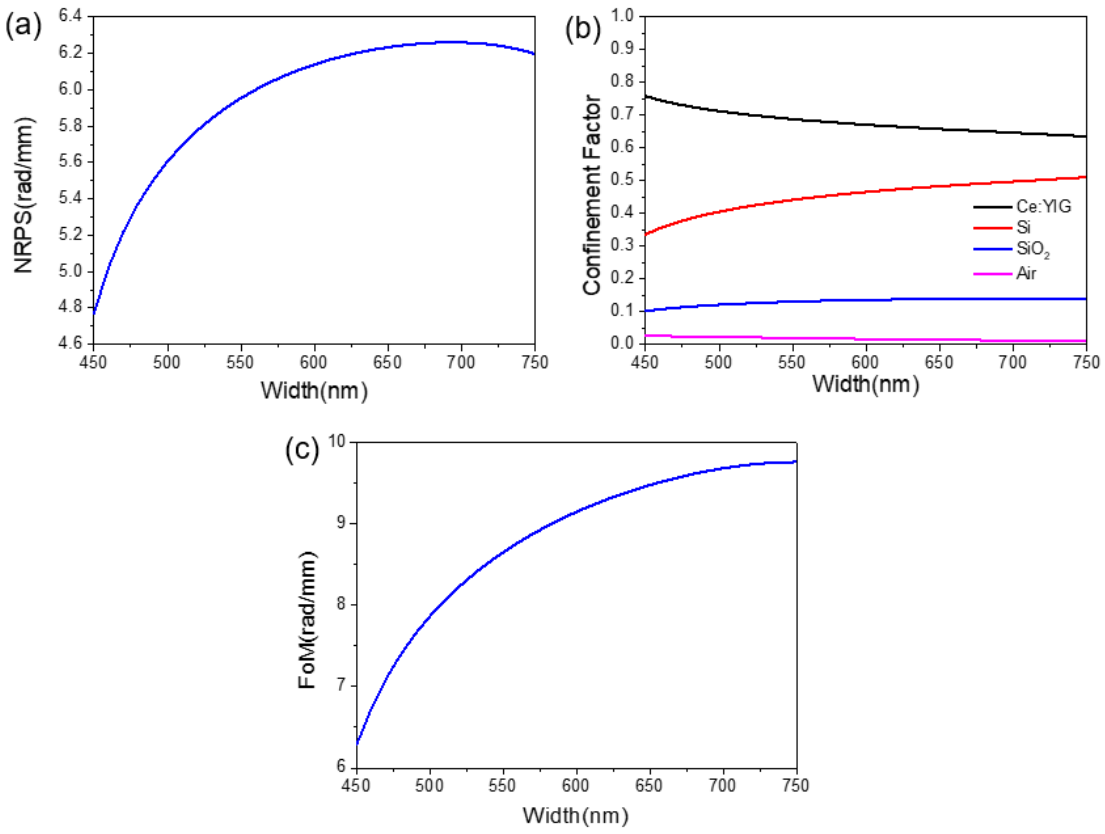


Fig.2-2 (a) NRPS, (b) confinement factor, and (c) FoM of MO waveguides with different widths.

## 2.3 Coupled-mode theory and mode evolution

The waveguide mode conversion from one or more modes to another one or more modes needs to be analyzed by the coupled-mode theory. The basic idea is to consider the change of the waveguide structure or material distribution of microelements in the coupling area as a disturbance and use the mode in the undisturbed waveguide to represent the mode in the disturbed waveguide to solve the coupling efficiency.

### 2.3.1 Coupled-mode theory

We assume that the effective permittivity of the undisturbed waveguide is $\varepsilon$, and the mode field components in the waveguide are $\vec{E}$ and $\vec{H}$; and the effective permittivity of the perturbed waveguide is $\varepsilon'$, and the corresponding mode field components are $\vec{E}'$ and $\vec{H}'$. Its field components satisfy the relationship

$$\begin{aligned} \nabla \times \vec{E} &= -i\omega\mu\vec{H} \\ \nabla \times \vec{H} &= i\omega\varepsilon\vec{E} \\ \nabla \times \vec{E}' &= -i\omega\mu\vec{H}' \\ \nabla \times \vec{H}' &= i\omega\varepsilon'\vec{E}' \end{aligned}, \tag{2-26}$$

then we can get

$$\nabla \cdot (\vec{E}^* \times \vec{H}' + \vec{E}' \times \vec{H}^*) = -i\omega(\varepsilon' - \varepsilon)\vec{E}^* \cdot \vec{E}', \tag{2-27}$$

intercept a microelement along the propagation direction (z-axis) in the waveguide and perform volume integration of Eq.2-27 by Gaussian's law as

$$\oiint_S (\vec{E}^* \times \vec{H}' + \vec{E}' \times \vec{H}^*) \cdot dS = -i\omega \iiint_V (\varepsilon' - \varepsilon)\vec{E}^* \cdot \vec{E}' dV, \tag{2-28}$$

where $dV = \Delta z \times dS$. When $\Delta z \to 0$, the surface integral can ignore the sidewall part and only involve the waveguide cross-sections on both sides of the microelement

$$\begin{aligned} &\iint_S ((\vec{E}^* \times \vec{H}' + \vec{E}' \times \vec{H}^*)_{z+\Delta z} - (\vec{E}^* \times \vec{H}' + \vec{E}' \times \vec{H}^*)_z) dS \\ &= -i\omega\Delta z \iint_S (\varepsilon' - \varepsilon)\vec{E}^* \cdot \vec{E}' dS \end{aligned} \tag{2-29}$$

to

$$\begin{aligned}\iint_S \frac{\partial}{\partial z}(\vec{E}^* \times \vec{H}' + \vec{E}' \times \vec{H}^*)dS &= \iint_S \frac{\partial}{\partial z}(\vec{E}_t^* \times \vec{H}_t' + \vec{E}_t' \times \vec{H}_t^*) \cdot \vec{e}_z ds \\ &= -i\omega \iint_S (\varepsilon' - \varepsilon)\vec{E}^* \cdot \vec{E}' dS\end{aligned}, \tag{2-30}$$

where $t$ represents the tangential direction of the waveguide cross-section [5]. Eq.2-30 is basic mode coupling formula, which gives the equivalent relationship between the modes on both sides of any waveguide microelement.

### 2.3.2 Intermode orthogonality and coupling coefficient

We will further analyze the Eq.2-30 under different waveguide structures. First, if the waveguide medium is homogeneous in the integration region ( $\varepsilon = \varepsilon'$ ). We set

$$\begin{aligned}\begin{bmatrix}\vec{E} \\ \vec{H}\end{bmatrix} &= \begin{bmatrix}\vec{E}_n \\ \vec{H}_n\end{bmatrix} \\ \begin{bmatrix}\vec{E}' \\ \vec{H}'\end{bmatrix} &= \begin{bmatrix}\vec{E}_m \\ \vec{H}_m\end{bmatrix}\end{aligned}, \tag{2-31}$$

where $n$ and $m$ represent the order of different modes. From Eq.2-30

$$(\beta_n - \beta_m)\iint_S (\vec{E}_{nt}^* \times \vec{H}_{mt} + \vec{E}_{mt} \times \vec{H}_{nt}^*) \cdot \vec{e}_z ds = 0 . \tag{2-32}$$

When $n = m$, then $\beta_n = \beta_m$, the equation is obviously established. When $n \neq m$, the integral term should be 0, that is, the $n$-order and $m$-order modes are orthogonal.

Substituting $-m$ for $m$ in Eq.2-32 and adding it to itself to get the basic mode orthogonal relationship

$$\begin{aligned}\iint_S (\vec{E}_{mt} \times \vec{H}_{nt}^*) \cdot \vec{e}_z ds &= 0 (n \neq m) \\ \iint_S (\vec{E}_{mt} \times \vec{H}_{nt}^*) \cdot \vec{e}_z ds &= 2P (n = m)\end{aligned} \tag{2-33}$$

normalized to

$$\begin{aligned}\iint_S (\vec{e}_{mt} \times \vec{h}_{nt}^*) \cdot \vec{e}_z ds &= 0 (n \neq m) \\ \iint_S (\vec{e}_{mt} \times \vec{h}_{nt}^*) \cdot \vec{e}_z ds &= 1 (n = m)\end{aligned}, \tag{2-34}$$

where $\vec{e}(x, y)$ and $\vec{h}(x, y)$ are normalized field components. Therefore, in a homogeneous waveguide, modes of different orders are orthogonal, and energy

crosstalk does not occur between modes. If the effective permittivity of the waveguide changes in the integration region, *i.e.*, $\varepsilon \neq \varepsilon'$, then the field components can be expressed as a linear superposition of the modes in the undisturbed waveguide as

$$\begin{bmatrix} \vec{E} \\ \vec{H} \end{bmatrix} = \begin{bmatrix} \vec{e}_n(x,y) \\ \vec{h}_n(x,y) \end{bmatrix} e^{-i\beta_n z}$$
$$\begin{bmatrix} \vec{E}' \\ \vec{H}' \end{bmatrix} = \sum_m a_m(z) \begin{bmatrix} \vec{e}_m(x,y) \\ \vec{h}_m(x,y) \end{bmatrix} e^{-i\beta_m z} \quad , \tag{2-35}$$

where $a_m(z)$ is the linear superposition factor. Taking into Eq.2-30

$$\sum_m (i\Delta\beta a_m + \frac{da_m}{dz}) e^{i\Delta\beta z} \iint_S \frac{\partial}{\partial z} (\vec{e}_{nt}^{\,*} \times \vec{h}_{mt} + \vec{e}_{mt} \times \vec{h}_{nt}^{\,*}) \cdot \vec{e}_z ds$$
$$= -i\omega \sum_m a_m e^{i\Delta\beta z} \iint_S (\varepsilon' - \varepsilon) \vec{e}_n^{\,*} \cdot \vec{e}_m ds \quad , \tag{2-36}$$

where $\Delta\beta = \beta_n - \beta_m$. Use the orthogonality relationship Eq.2-36 to simplify the left side, only when $n = m$ and $\Delta\beta = 0$ the integral is not 0, to get

$$\frac{da_n}{dz} = -i \sum_m a_m(z) e^{i\Delta\beta z} C_{m,n} \, , \tag{2-37}$$

where the coupling coefficient $C_{m,n}$ is:

$$C_{m,n} = \frac{\omega}{2} \iint_S (\varepsilon' - \varepsilon) \vec{e}_n^{\,*} \cdot \vec{e}_m ds \, . \tag{2-38}$$

### 2.3.3 Mode evolution

Consider two mode: mode$_A$ and mode$_B$ in an unperturbed waveguide as

$$a_A(z) \begin{bmatrix} \vec{e}_A(x,y) \\ \vec{h}_A(x,y) \end{bmatrix} e^{-i\beta_A z}$$
$$a_B(z) \begin{bmatrix} \vec{e}_B(x,y) \\ \vec{h}_B(x,y) \end{bmatrix} e^{-i\beta_B z} \quad , \tag{2-39}$$

then the field of the cross-section is

$$a_A(z) \begin{bmatrix} \vec{e}_A(x,y) \\ \vec{h}_A(x,y) \end{bmatrix} e^{-i\beta_A z} + a_B(z) \begin{bmatrix} \vec{e}_B(x,y) \\ \vec{h}_B(x,y) \end{bmatrix} e^{-i\beta_B z} \, . \tag{2-40}$$

Similar to Eq.2-35, the coupled-mode equations can be written as

$$\begin{aligned} \frac{da_A}{dz} &= -iC_{BA}a_B(z)e^{-i\Delta\beta z} \\ \frac{da_B}{dz} &= -iC_{AB}a_A(z)e^{-i\Delta\beta z} \end{aligned}, \tag{2-41}$$

where

$$\begin{aligned} C_{BA} &= \frac{\omega}{2}\iint_S(\varepsilon_B - \varepsilon_{cladding})\vec{e}_B^{\,*}\cdot\vec{e}_A ds \\ C_{AB} &= \frac{\omega}{2}\iint_S(\varepsilon_A - \varepsilon_{cladding})\vec{e}_A^{\,*}\cdot\vec{e}_B ds \\ \Delta\beta &= \beta_A - \beta_B \end{aligned} \tag{2-42}$$

if the two modes have the same effective permittivity, the phase-matching coupling condition is satisfied, that is

$$\begin{aligned} \beta_A &= \beta_B \equiv \beta_0 \\ C_{AB} &= C_{BA} \equiv C \end{aligned}. \tag{2-43}$$

If we input mode$_B$ power as $P_0$, Eq.2-41 can be solved as

$$\begin{aligned} P_A(z) &= \left|a_A(z)\right|^2 = P_0\sin^2(Cz) \\ P_B(z) &= \left|a_B(z)\right|^2 = P_0\cos^2(Cz) \end{aligned}. \tag{2-44}$$

That is, the energy oscillates between mode$_A$ and mode$_B$, and the conversion between modes can be realized by designing an appropriate coupling length.

To explain mode coupling from the perspective of mode analysis, it is because the eigenmodes supported in the coupling structure at this time will become equal-energy mode$_A$+mode$_B$ (even mode) and mode$_A$-mode$_B$ (odd mode). Since the effective refractive index ($n_{eff}$) of the two hybridized eigenmodes is slightly different, the two-mode components of the interference output under different propagation lengths will also change accordingly. The half-beat length is given by

$$\mathrm{L}_\pi = \frac{\pi}{\beta_{even} - \beta_{odd}}. \tag{2-45}$$

For the mode evolution, if the effective permittivity changes slowly enough, *i.e.*, $\varepsilon' \approx \varepsilon$ and $\Delta\beta \approx 0$, Eq.2-37 will be

$$\frac{da_n}{dz} = 0. \tag{2-46}$$

It can be simply understood that the input $n$-order mode component will not

change with the propagation distance. And the $n$-order mode at the input port will be converted to the $n$-order mode at the output port with a mode conversion efficiency of ~100%.

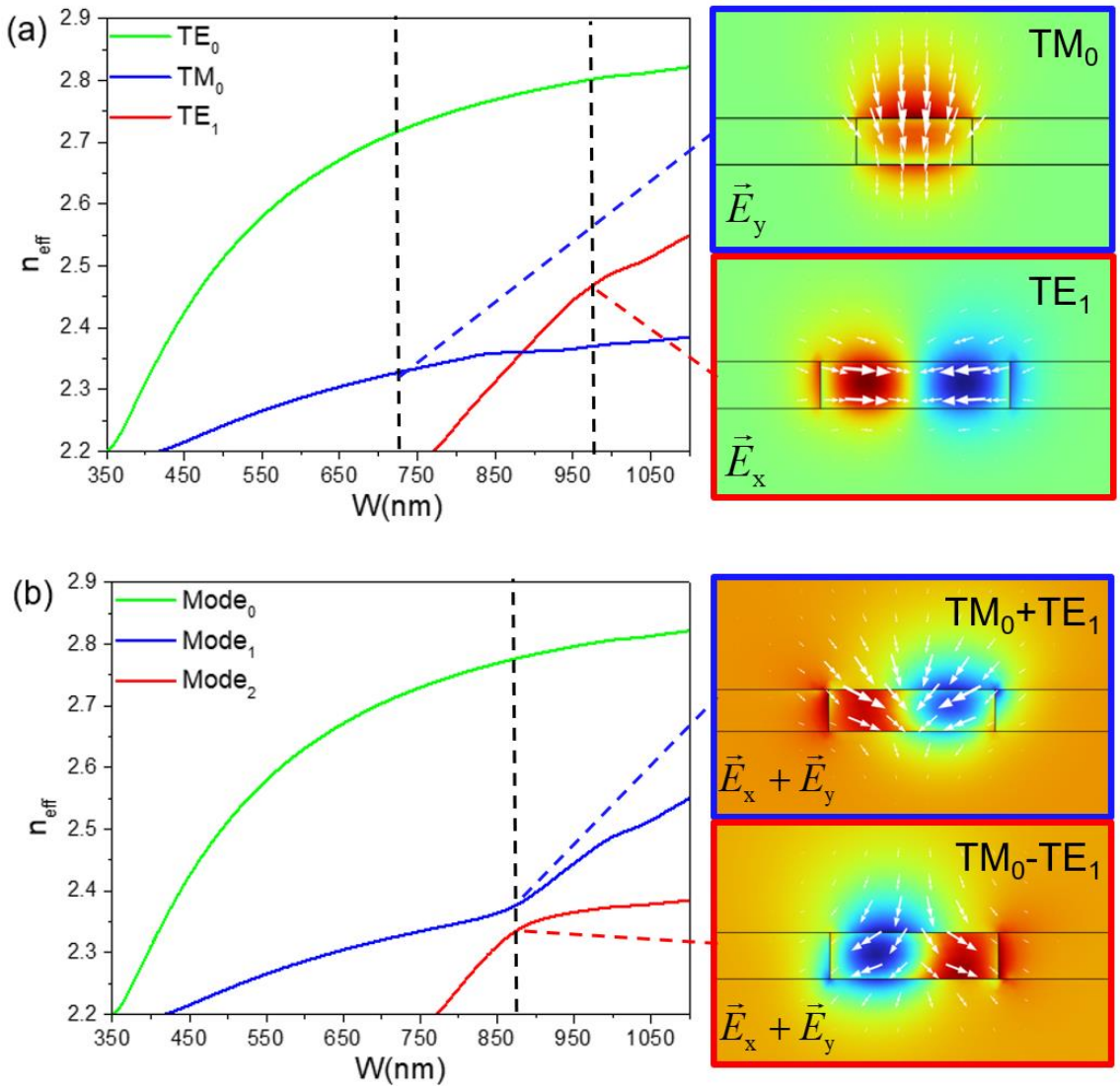


Fig.2-3 $n_{eff}$ change with different with of MO waveguide calculated by (a) semi-vector and (b) full-vector simulations. The insets show the mode field distribution at a specific width, and the white arrows indicate the electric field direction.

Based on the MO waveguide structure fabricated by wafer bonding as shown in Fig.2-1 (a), we discuss the differences between mode coupling mode evolution. As shown in Fig.2-3 (a), as the width of the MO waveguide changes, the $n_{eff}$ curves of

the $TE_1$ mode $TM_0$ modes will cross when the waveguide width is ~ 875 nm with a wavelength of 1550 nm. Under this width, the $TE_1$ and $TM_0$ modes in the waveguide will hybrid. The two hybridized eigenmodes have electric fields of x- and y-components as a mixture of $TE_1$ and $TM_0$ modes but are orthogonal to each other. This hybridization occurs only when the waveguide has asymmetry in the vertical direction (As shown in the insets of Fig.2-3 (b)). If the waveguide width changes rapidly near the hybridization point and the adiabatic mode conversion condition is not satisfied, the process involves mode excitation, and its overlap between modes can be calculated by [6]

$$\eta = \frac{(\iint (\vec{E}^* \times \vec{H}' + \vec{E}' \times \vec{H}^*) \cdot \vec{e}_z ds)^2}{\iint (\vec{E}^* \times \vec{H} + \vec{E} \times \vec{H}^*) \cdot \vec{e}_z ds \times \iint (\vec{E}'^* \times \vec{H}' + \vec{E}' \times \vec{H}'^*) \cdot \vec{e}_z ds}, \tag{2-47}$$

then the $TE_1$ ($TM_0$) mode will remain as the $TE_1$ ($TM_0$) mode due to the large overlap.

But if the waveguide width change around the hybridization point satisfies the adiabatic gradient condition, the mode conversion process will take place along Fig.2-3 (b). Since there is no energy coupling between different-order modes, $mode_1$ and $mode_2$ can be used for efficient mode conversion between $TE_1$ and $TM_0$ modes. Such a mode converter design will be discussed in detail in the following chapters.

### 2.3.4 Mode coupling vs. Mode evolution

Finally, we will compare the tolerances of $TE_1$&$TM_0$ mode converters based on mode coupling and mode evolution to demonstrate the high robustness of mode-evolution-based devices [7-10].

The converter structure and transmission field distribution are shown in Fig.2-4. Although ideally, both devices can achieve mode conversion efficiencies of ~ 99%, mode-coupled devices are more sensitive to fabrication errors and wavelength changes [11-13].

For mode coupling, the input $TM_0$ mode will excite equal energy and in-phase $TM_0$+$TE_1$ and $TM_0$-$TE_1$ hybridization modes in the 875-nm-wide waveguide. After propagation of the half-beat length, the phase difference between the two hybrid modes will be $\pi$, and the connection with the output waveguide here will excite the $TE_1$ mode and output (as shown in Figs.2-4 (a) and (b)). On the one hand, it can be

known from Eq.2-44 that the mode conversion efficiency satisfies a sinusoidal function with the propagation distance, so the length error will affect the mode conversion efficiency; on the other hand, Eq.2-43 shows that when the waveguide width or operating wavelength changes, because the dispersion of the $TE_1$ and $TM_0$ modes is different, the phase-matching coupling condition cannot be satisfied, and its mode conversion efficiency will be also negatively affected.

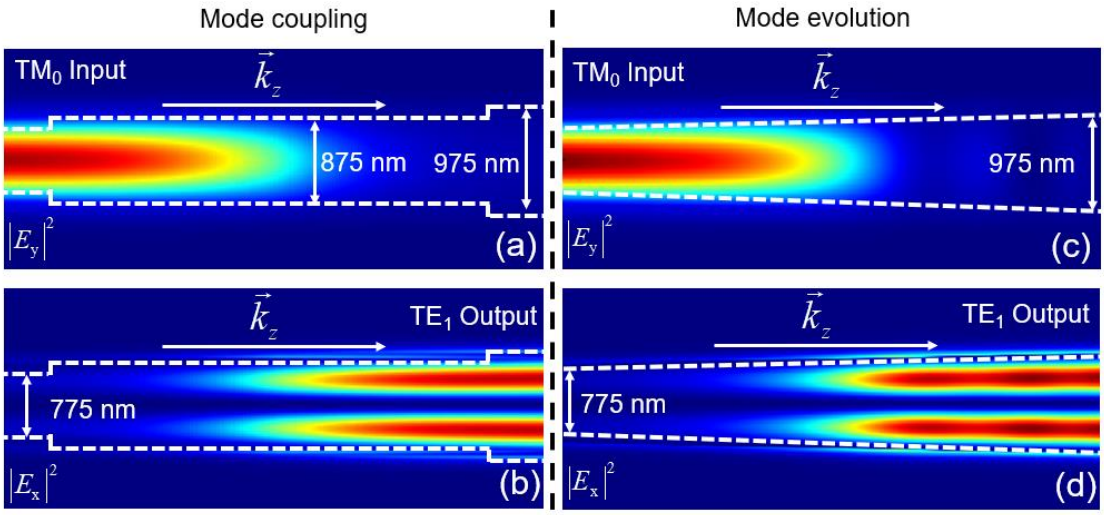


Fig.2-4 (a) $E_y$ and (b) $E_x$ field distributions of the mode converter based on the mode coupling. (c) $E_y$ and (d) $E_x$ field distributions of the mode converter based on the mode evolution.

Table.2-1 Tolerance analysis of mode conversion efficiency

| Error | | Mode coupling (%) | Mode evolution(%) |
|---|---|---|---|
| Coupler Length | + 5 μm | 90.2 | 99.9 |
| | - 5 μm | 91.2 | 99.9 |
| Coupler Width | + 10 nm | 94.7 | 99.8 |
| | - 10 nm | 89.7 | 99.8 |
| Wavelength | + 10 nm | 98.0 | 99.9 |
| | - 10 nm | 89.3 | 99.8 |

For mode evolution, the input mode$_1$ is initially $TM_0$ mode, which is converted to $TE_1$ mode by an adiabatically tapered waveguide (as shown in Figs.2-4 (c) and (d)). On the one hand, the length of the coupler only needs to meet the adiabatic evolution

condition, so the length increase will not affect the device performance at all; on the other hand, if the tapered waveguide covers the mode hybridization point, high-efficiency mode conversion can be achieved, so the waveguide width error and wavelength changes will only affect the position of the hybridization point and not mode conversion efficiency [14,15]. The converter can operate in an extremely broadband [16-19].

The numerical tolerance analysis from fabrication error and wavelength changes is shown in Table 2-1.

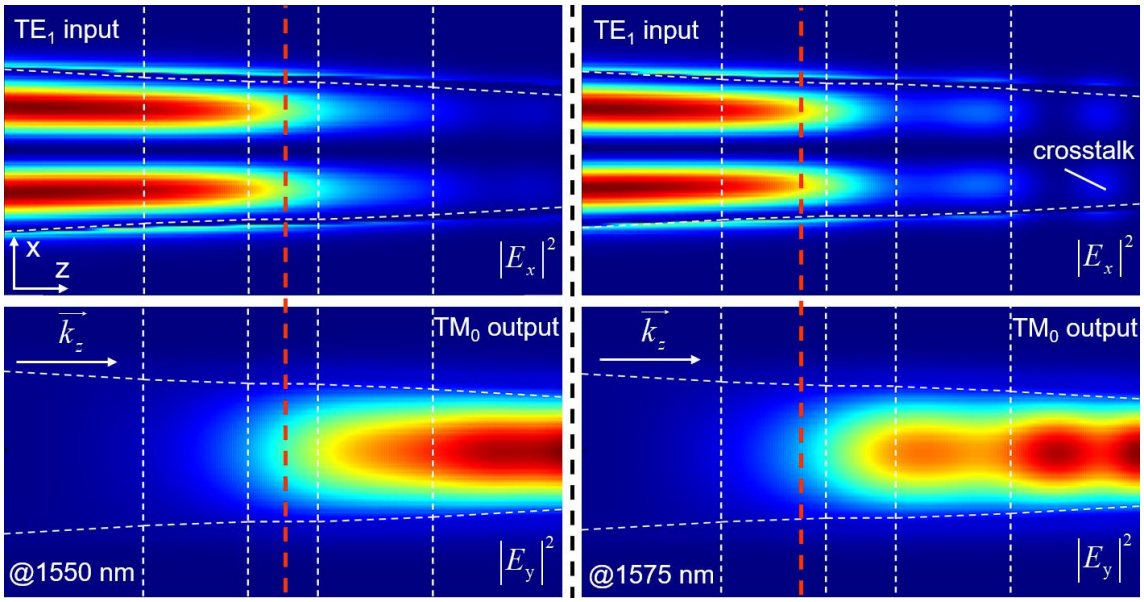


Fig.2-5 Transmission field distribution of $TE_1$&$TM_0$ mode converters with nonlinear tapered waveguide at wavelengths of 1550 nm and 1575 nm.

The mode converters and mode couplers based on mode evolution could also be designed with a nonlinear tapered waveguide structure to reduce the device length, but the fabrication tolerance and operation bandwidth would be reduced. As shown in Fig.2-5, we divided the $TE_1$&$TM_0$ converter into five parts for design. Since the mode hybridization point was in the center part as the red line shows, the width of the waveguide near the two sides changed faster, while the width of the central part changed smoothly, and the overall length of the device could be reduced by ~47%. At the design wavelength of 1550 nm, lossless mode conversion could also be achieved; however, when there were fabrication errors or a deviation in the operation

wavelength, the hybridization point would be at the off-center part leading to a break in the adiabatic condition, thereby introducing additional IL and crosstalk. As shown in Fig.2-5, at a wavelength of 1575 nm, the component introduces an IL and crosstalk of ~ 0.2 dB. Therefore, to ensure the high fabrication tolerance and wide operation bandwidth of the device, we chose the design of a linear tapered waveguide.

## 2.4 Summary

In this chapter, we deduced and discussed the basic principles involved in device design in the following chapters.

For the MO effect, we discussed the determination of the off-diagonal elements of the permittivity tensor based on FR effect, deduced the calculation method of NRPS under different polarizations, and discussed the necessary conditions for the MO waveguide structure to support NRPS of TE or TM modes. Finally, the relationship between the FoM of the MO waveguide and its structural parameters was discussed based on the confinement factor.

For mode evolution, we deduced the phase-matching coupling conditions in or between waveguides and the working principle of mode-coupling devices from the coupled-mode theory; and discussed the principle of mode evolution based on the mode coupling equation. Finally, the fabrication tolerances of mode-coupling- and mode-evolution-based devices were compared.

## References


1. Yamamoto S. and Makimoto T., "Circuit theory for a class of anisotropic and gyrotropic thin-film optical waveguides and design of nonreciprocal devices for integrated optics." *Journal of Applied Physics* 45.2 (1974): 882-888. DOI: 10.1063/1.1663332
2. Shamonin M. and Hertel P., "Analysis of nonreciprocal mode propagation in magneto-optic rib-waveguide structures with the spectral-index method." *Applied Optics* 33.27 (1994): 6415-6421. DOI: 10.1364/AO.33.006415
3. Bahlmann N., Chandrasekhara V., Erdmann A., Gerhardt R., Hertel P., Lehmann R., Salz D. and Wallenhorst M., "Improved design of magnetooptic rib waveguides for optical isolators." *Journal of Lightwave Technology* 16.5 (1998): 818. DOI: 10.1109/50.669010
4. Robinson J.T., Preston K., Painter O. and Lipson M., "First-principle derivation of gain in high-index-contrast waveguides." *Optics Express* 16.21 (2008): 16659-16669. DOI: 10.1364/OE.16.016659
5. Haus H., Huang W., Kawakami S. and Whitaker N., "Coupled-mode theory of optical waveguides." *Journal of Lightwave Technology* 5.1 (1987): 16-23. DOI: 10.1109/JLT.1987.1075416
6. Lohmeyer M. and Stoffer R., "Integrated optical cross strip polarizer concept." *Optical and Quantum Electronics* 33 (2001): 413-431. DOI: 10.1023/A:1010894801196
7. Yuan W., Kojima K., Wang B., Koike-Akino T., Parsons K., Nishikawa S. and Yagyu E., "Mode-evolution-based polarization rotator-splitter design via simple fabrication process." *Optics Express* 20.9 (2012): 10163-10169. DOI: 10.1364/OE.20.010163
8. Tseng S.Y., "Counterdiabatic mode-evolution based coupled-waveguide devices." *Optics Express* 21.18 (2013): 21224-21235. DOI: 10.1364/OE.21.021224
9. Watts M.R. and Haus H.A., "Integrated mode-evolution-based polarization rotators." *Optics Letters* 30.2 (2005): 138-140. DOI: 10.1364/OL.30.000138
10. Watts M.R., Haus H.A. and Ippen E.P., "Integrated mode-evolution-based polarization splitter." *Optics Letters* 30.9 (2005): 967-969. DOI: 10.1364/OL.30.000967
11. Byrd M.J., Timurdogan E., Su Z., Poulton C.V., Fahrenkopf N.M., Leake G., Coolbaugh D.D. and Watts M.R. "Mode-evolution-based coupler for high saturation power Ge-on-Si photodetectors." *Optics Letters* 42.4 (2017): 851-854. DOI: 10.1364/OL.42.000851
12. Hung Y.J., Li Z.Y., Chung H.C., Liang F.C., Jung M.Y., Yen T.H. and Tseng S.Y., "Mode-evolution-based silicon-on-insulator 3 dB coupler using fast quasiadiabatic dynamics." *Optics Letters* 44.4 (2019): 815-818. DOI: 10.1364/OL.44.000815
13. Elfiqi A.E., Tanomura R., Yu D., Yanwachirakul W., Shao H., Suzuki Y., Tanemura T. and Nakano Y., "Robust InP/InGaAsP polarization rotator based on mode

evolution." *IEEE Photonics Technology Letters* 34.2 (2022): 109-112. DOI: 10.1109/LPT.2022.3141518

14. Zhang J., Yu M., Lo G.Q. and Kwong D.L., "Silicon-waveguide-based mode evolution polarization rotator." *IEEE Journal of Selected Topics in Quantum Electronics* 16.1 (2009): 53-60. DOI: 10.1109/JSTQE.2009.2031424
15. Kim S. and Qi M., "Mode-evolution-based polarization rotation and coupling between silicon and hybrid plasmonic waveguides." *Scientific Reports* 5.1 (2015): 18378. DOI: 10.1038/srep18378
16. Mia M.B., Ahmed S.Z., Jaidye N., Ahmed I. and Kim S., "Mode-evolution-based ultra-broadband polarization beam splitter using adiabatically tapered extreme skin-depth waveguide." *Optics Letters* 46.18 (2021): 4490-4493. DOI: 10.1364/OL.434110
17. Wang J., Xuan Y., Qi M., Huang H., Li Y., Li M., Chen X., Sheng Z., Wu A., Li W. and Wang X., "Broadband and fabrication-tolerant on-chip scalable mode-division multiplexing based on mode-evolution counter-tapered couplers." *Optics Letters* 40.9 (2015): 1956-1959. DOI: 10.1364/OL.40.001956
18. Wang J., Niu B., Sheng Z., Wu A., Li W., Wang X., Zou S., Qi M. and Gan F., "Novel ultra-broadband polarization splitter-rotator based on mode-evolution tapers and a mode-sorting asymmetric Y-junction." *Optics Express* 22.11 (2014): 13565-13571. DOI: 10.1364/OE.22.013565
19. Sia J.X.B., Wang W., Guo X., Zhou J., Zhang Z., Rouifed M.S., Li X., Qiao Z., Liu C., Littlejohns C., Reed G.T. and Wang H., "Mid-infrared, ultra-broadband, low-loss, compact arbitrary power splitter based on adiabatic mode evolution." *IEEE Photonics Journal* 11.2 (2019): 1-11. DOI: 10.1109/JPHOT.2019.2907788

# Chapter III

# Asymmetric directional-coupler-based isolator and circulator

## 3.1 Introduction

Based on the challenges of silicon-based integrated broadband MO nonreciprocal devices prepared by wafer bonding discussed in Chapter 1, we will optimize the structure and performance of MMI-based TE-mode devices in this chapter.

The basic idea was to design a TE-mode nonreciprocal device based on an asymmetric directional coupler, and the mode conversion process involved in the device is shown in Fig.3-1. By designing an adiabatic half mode converter, the input $TE_0$ mode would be converted into equal-energy $TE_0$ and $TM_0$ modes and propagated to the MO waveguide to accumulate NRPS. After it, by a reverse mode conversion process, the two modes would be interfered and output. The output efficiency was determined by the phase difference between the two modes in the multimode MO waveguide [1]. Since the MO waveguide only supported NRPS of $TM_0$ mode and no push-pull structure design, the device could work under a unidirectional magnetic field, which simplified the difficulty of magnetic field integration.


Fig.3-1 Mode conversion process in the device.

To reduce the IL, we employed some tricky design included: combining the mode converter with the nonreciprocal phase shifter, and using the NRPS of the TE-TM-

hybrid mode in the polarization rotation process, which avoided additional PRs, reducing the IL and on-chip footprint; the waveguide had no abrupt structure, avoiding the IL caused by mode mismatching; light would propagate into the Ce:YIG bonded region when it was still in TE-polarized to reduce the junction loss at the edge of the Ce:YIG chip [2].

Herein, we will discuss in detail the working principle and parameter design of the device. Finally, the performance of the device will be demonstrated and discussed in combination with theoretical analysis.

## 3.2 Device structure and operation principle

The proposed device structure is shown in Fig.3-2. A four-port device composed of two parallel MO waveguides with a gap of 150 nm and complementary widths. The device was designed based on a silicon-on-insulator (SOI) wafer with a standard 220-nm-thick silicon ( $n_{Si} = 3.48$ ) layer; bonded Ce:YIG ( $n_{Ce:YIG} = 2.2$ [3,4]) as the upper cladding covering the entire device area to provide the out-of-plane directional asymmetry required for mode hybridization and to support the NRPS of the $TM_0$ mode [5,6]. The device presented a quasi-one-dimensional structure without abrupt junction structures, so it was hoped to have advantages over traditional devices in terms of on-chip footprint and IL.

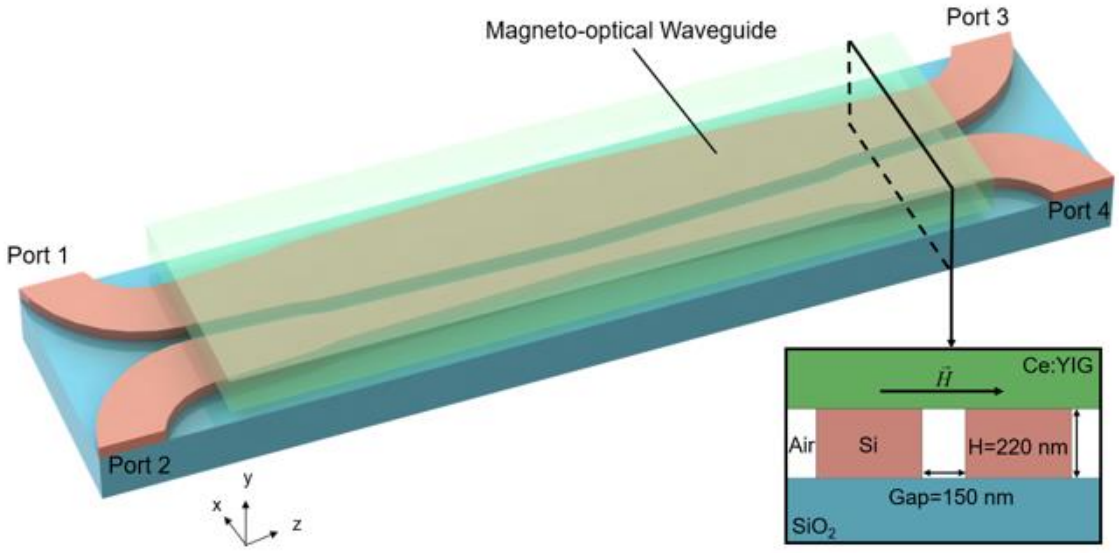


Fig.3-2 Device structure and cross-sectional structure.

Its working principle was: divided the input $TE_0$ mode light into TE zero- and first-order modes ($mode_0$ and $mode_1$, respectively) equally in the MO waveguides, and converted the $mode_1$ into TM mode for the NRPS accumulation of $\pi$ required by the isolator operation.

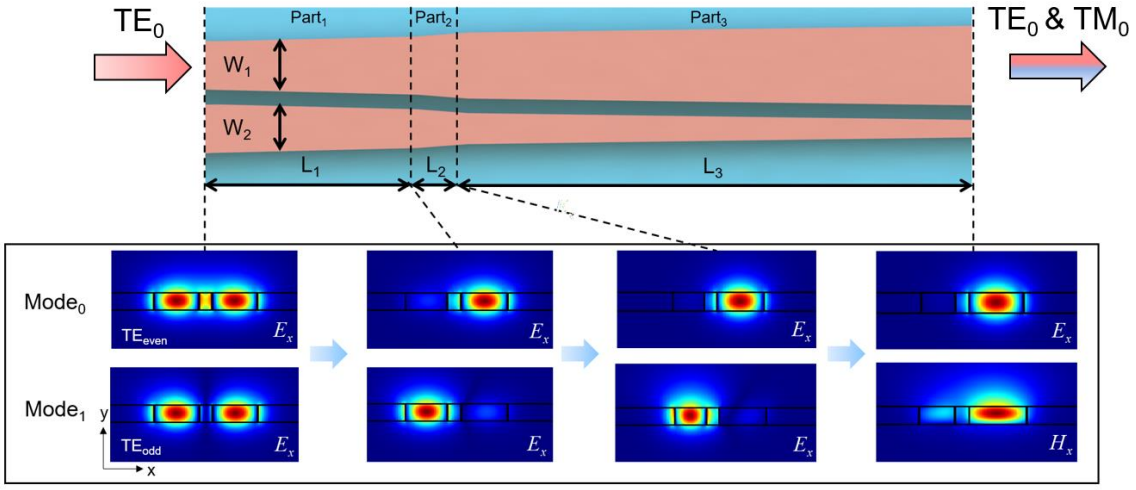


Fig.3-3 The mode conversion process and the mode field distribution at specific positions.

The specific mode conversion process is shown in Fig.3-3, the structure on the input side could be divided into three parts according to the different mode conversion functions: at the input port such as Port 1, the widths of the two waveguides, *i.e.*, $W_1$ and $W_2$ respectively, were equal, so the incident $TE_0$ mode would excite $TE_{even}$ mode ($mode_0$) and $TE_{odd}$ mode ($mode_1$) with equal energy; in $Part_1$, as $W_1$ increases ($W_2$ decreases), $mode_0$ and $mode_1$ were converted into $TE_0$ mode in the wide and narrow waveguide, respectively; $Part_2$ was only used as a connection and did not involve any mode conversion; in $Part_3$, as the waveguide width changes, $mode_1$ would gradually convert from the $TE_0$ mode in the narrow waveguide to the $TM_0$ mode in the wide waveguide, and the TE-TM-hybrid mode in this process was available for NRPS accumulation. Finally, after the reverse mode conversion process, the two modes would interfere and output to Port 3; and in the backward transmission, due to the NRPS, the light input from Port 3 would output from Port 2 instead of Port 1, so this device could operate as a TE-mode isolator also a four-port TE-mode circulator. The

field distributions of mode$_0$ and mode$_1$ at the junction between each part were shown in Fig.3-3.

## 3.3 Simulation and parameter design

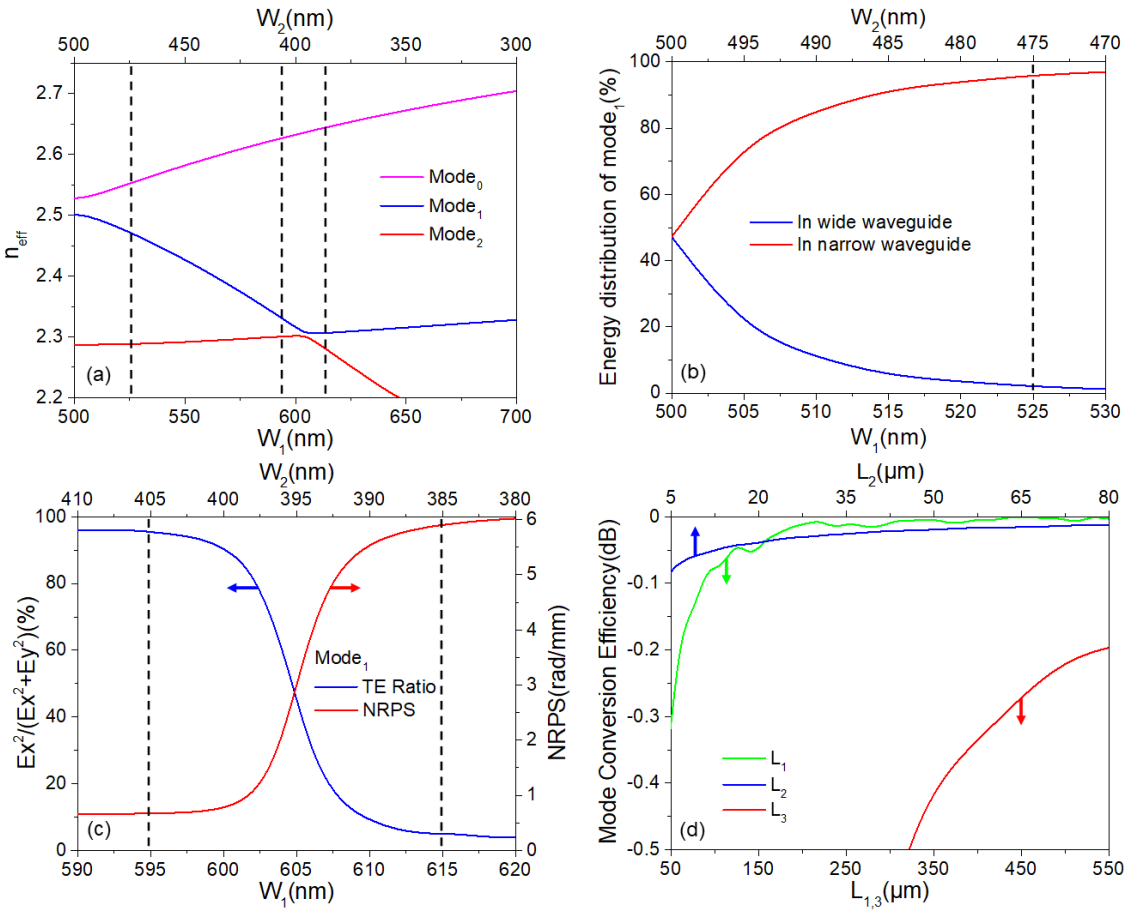


Fig.3-4 Device structure parameter design. (a) $n_{eff}$ varies with waveguide width. (b) Mode energy distribution of mode$_1$ in Part$_1$ as a function of waveguide width. (c) The TE ratio and NRPS of mode$_1$ in Part$_3$ vary with the waveguide structure. (d) Mode conversion efficiency as a function of the lengths of each part.

We first set the width of the input and output single-mode waveguide as 500 nm, so $W_1 = W_2 = 500$ nm at the input/output ends. Keeping the sum of the widths of the two MO waveguides constant of 1 μm, the $n_{eff}$ of the eigenmodes in the composite waveguide varied with the waveguide width at a wavelength of 1550 nm as shown in Fig.3-4 (a). When $W_1/W_2$ was 500 nm/500 nm and 600 nm/400 nm, the $n_{eff}$ between

the modes were close to each other, corresponding to $TE_0$-$TE_0$ and $TE_0$-$TM_0$ hybridization respectively. Based on the mode hybridization width, the adiabatic tapered waveguide could be divided into three parts for design.

For the width design. Firstly, for $Part_1$, we designed the width change range corresponding to the mode conversion process of $mode_1$ from $TE_{odd}$ mode to $TE_0$ mode in the narrow waveguide. The starting width $W_1/W_2$ was 500 nm/500 nm, and then by simulating the energy distribution of $mode_1$ in the two waveguides as the $W_1/W_2$ changes as shown in Fig.3-4 (b), when 95% of the energy was confined to the narrow waveguide, we assumed that the mode conversion was completed, and the corresponding ending width was 525 nm/475 nm; and for $Part_3$, we designed the width change range corresponding to that the $mode_1$ converted from $TE_0$ in the narrow waveguide to $TM_0$ in the wide waveguide. By simulating the TE ratio of $mode_1$ around the $TE_0$-$TM_0$ hybrid point under various $W_1/W_2$ as the blue curve shown in Fig.3-4 (c), the TE ratio was designed from 95% to 5% as the starting and ending point of the mode conversion corresponding to a width of 595 nm/405 nm and 615 nm/385 nm, respectively [7].

Table.3-1 Structural Parameters

| $Part_i$ | $W_1$ (nm) | $W_2$ (nm) | $L_i$ (μm) |
|---|---|---|---|
| $Part_1$ | 500 → 525 | 500 → 475 | 200 |
| $Part_2$ | 525 → 595 | 475 → 405 | 50 |
| $Part_3$ | 595 → 615 | 405 → 385 | 499 |

For the length design, the correspondence between the length of each part ($L_{1,2,3}$) and the mode conversion efficiency is shown in Fig.3-4 (d). For $Part_1$ and $Part_2$, the length only needed to meet the adiabatic evolution condition, by designing the mode conversion efficiency to be 99% (~0.04 dB), the lengths were $L_1$ = 200 μm and $L_2$ = 50 μm, respectively; for $Part_3$, in addition to the mode conversion efficiency, the $L_3$ also needed to ensure that the total NRPS of $mode_1$ was $\pi/2$, so by assuming the FR of Ce:YIG of -4500 °/cm and simulating the NRPS of $mode_1$ in $Part_3$ varied with $W_1/W_2$ as the red curve shown in Fig.3-4 (c), $L_3$ should be designed to be 499 μm which was obtained by integral calculation. As the red curve in Fig.3-4 (d), the mode conversion efficiency in $Part_3$ was ~95% (~0.22 dB). Therefore, the total IL caused by

the mode conversion process was ~0.6 dB.

The structural parameters were shown in Table.3-1.

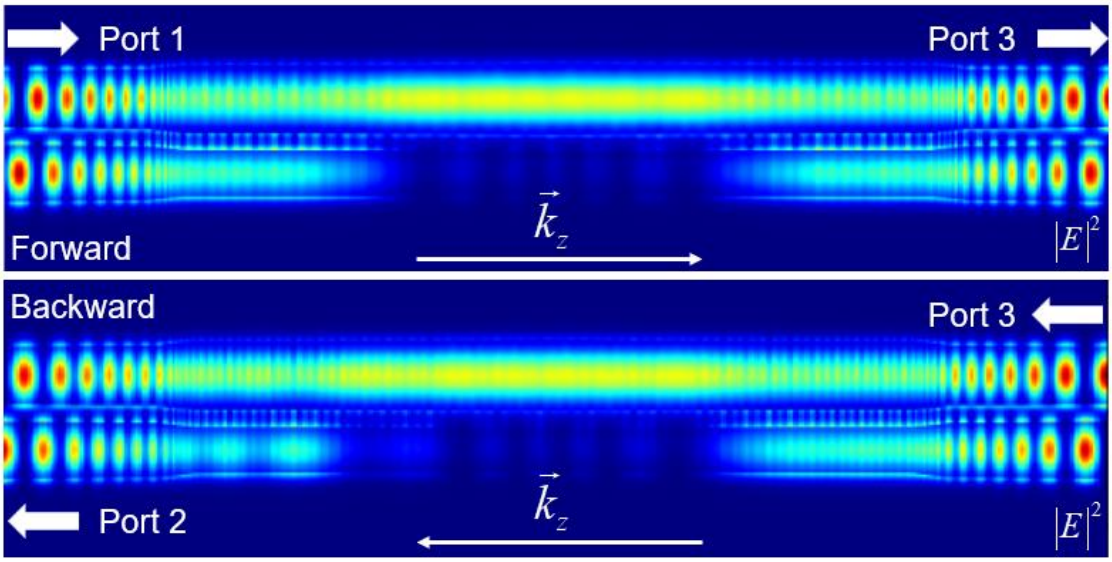


Fig.3-5 Forward and backward transmission field distribution simulated by FDTD.

Based on such structural parameters, the forward and backward transmission field distribution of the device was simulated by FDTD solution as shown in Fig.3-5. It could be seen that when the light was input as $TE_0$ mode from Port 1, the light would output to Port 3; and when the input was input from Port 3, the light would output to Port 2, which meet the device design expectations [8].

## 3.4 Experiment preparation

The device fabrication process flow is shown in Fig.3-6. The SOI substrate was pre-deposited a 200-nm-thick $SiO_2$ layer as a hard mask by P-CVD. Then the spin-coated ZEP520A photoresist was patterned by electron beam lithography (EBL) and development process. Two-step reactive ion etching (RIE) of $CF_4$ and $SF_6$ transferred the pattern to the $SiO_2$ mask layer and the Si core layer. Then, the upper cladding $SiO_2$ was removed by HF solution to complete the Si waveguide fabrication.

1.5 mm×1.5 mm Ce:YIG (500 nm)/SGGG chips were integrated as the upper cladding layer of the device by nitrogen plasma surface-activated wafer bonding.

Finally, the devices could be tested after dicing (See the appendix for details of the process).

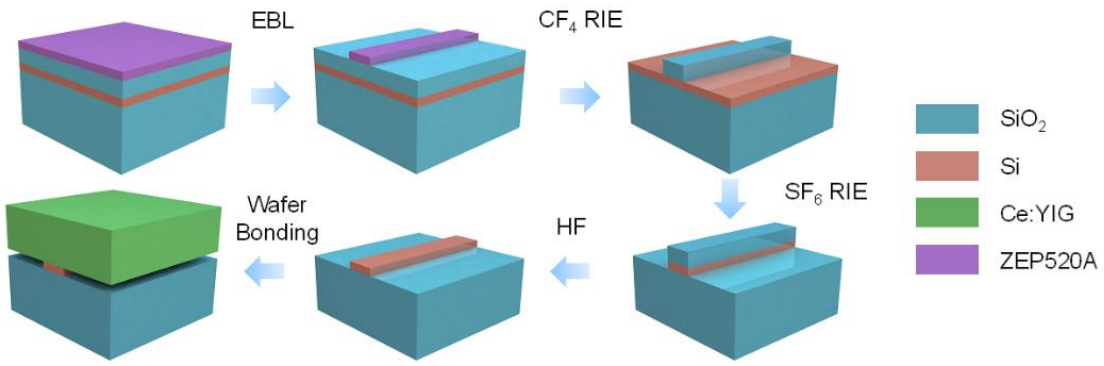


Fig.3-6 Process flow.

## 3.5 Device characterization

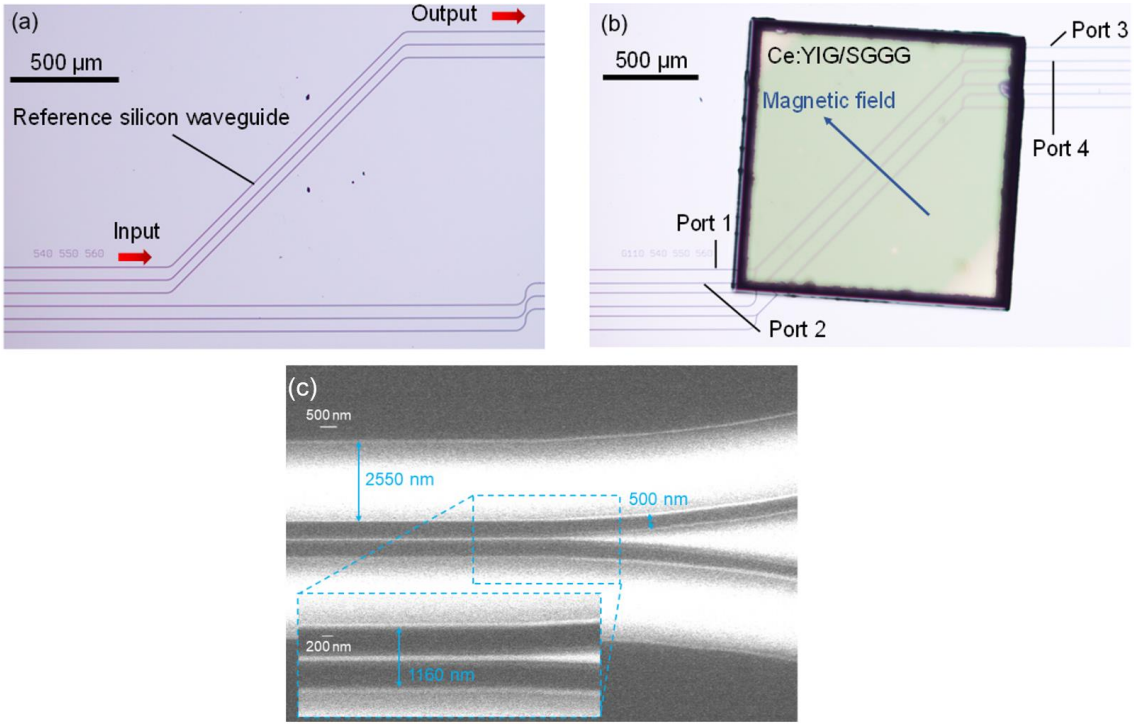


Fig.3-7 Device structure characterization. Micrographs of (a) reference waveguides and (b) devices. (c)SEM photo of the input/output port.

After the device was prepared, we characterized the structure and performance of

the device.

The micrographs of the reference waveguide and the device are shown in Figs.3-7 (a) and (b). The reference waveguide was a silicon waveguide with the same length as the device, without any other additional loss mechanism; in the device micrograph, the green area was the bonded Ce:YIG/SGGG chip; the devices were arranged diagonally to increase the bonding tolerance, and the blue arrows indicate that the direction of the applied magnetic field which was orthogonal to the propagation direction. Fig.3-7 (c) is the SEM photo of the waveguide at the input/output port, and the actual size of the device was in line with the design.

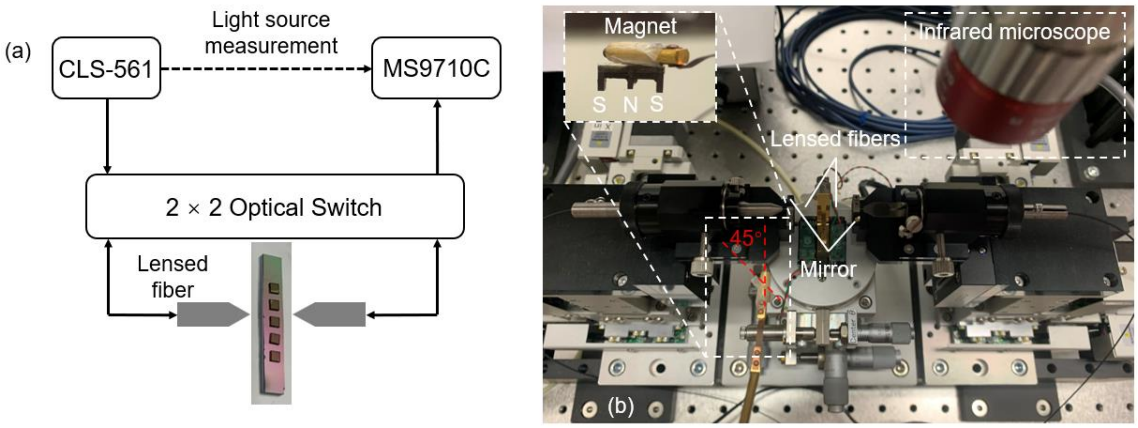


Fig.3-8 (a) Diagram and (b) photos of the test system.

The structure of the measurement system is shown in Fig.3-8 (a). A broadband amplified spontaneous emission (ASE) light source (CLS-561) was used to generate light in the wavelength range of 1530~1600 nm. A 2 × 2 optical switch was employed to control forward and backward propagation.

As shown in Fig.3-8 (b), the fiber-to-waveguide coupling was performed microscopically. The E-shaped magnet, which was set at 45° with the frame, provides an external magnetic field sufficient to magnetize the Ce:YIG chip to saturation at in-plane direction. The output light was transmitted to a spectrum analyzer (MS9710C) to measure the transmittance characteristics of the device.

The measured transmission spectrum of the reference waveguide and the forward and backward transmission spectra of the device between Port 2 and Port 4 are shown in Fig.3-9 (a). Under TE-polarized light input, the maximum IR of ~ 15 dB was measured at a wavelength of 1537.3 nm, the corresponding IL was 5 dB, and the 10-

dB isolation bandwidth was 2 nm. The theoretical fitting curves of IR and IL are shown in Fig. 3-9 (b), and the actual spectral line of the device was in line with the theoretical line shape.

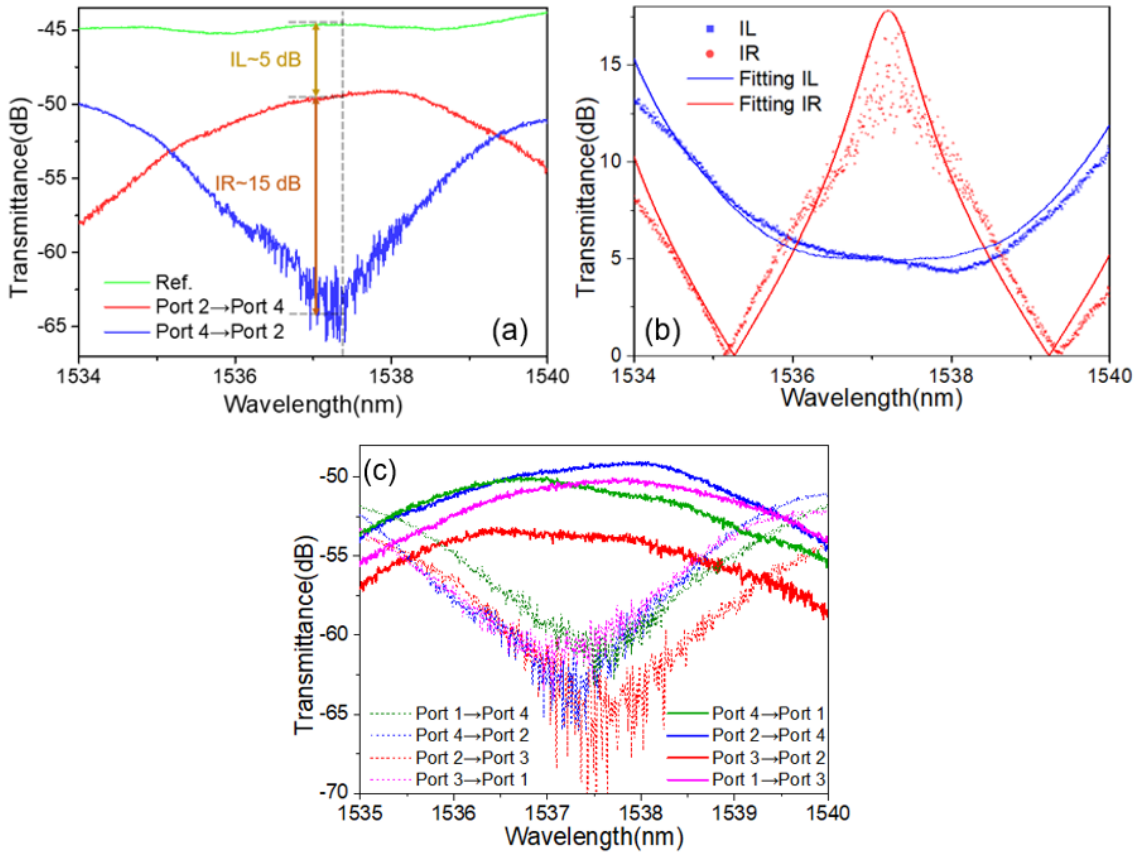


Fig.3-9 (a) The spectra of the reference waveguide and the device in forward and backward transmission. (b) The theoretical fitted device performance. (c) Four-port circulator spectra.

The device could also work as a four-port circulator, and its spectra are shown in Fig.3-9 (c). The crosstalk between the four ports was ~10 dB. The performance difference between the ports was due to the fiber-to-waveguide coupling efficiency error caused by dicing; and the uneven edge of the Ce:YIG chip.

## 3.6 Discussion

We broke down the IL as shown in Table.3-2 and Fig.3-10 (c). Including: (1) Mode conversion loss of ~0.6 dB mentioned in Section 3.3. (2) The junction loss from mode mismatching between the air-clad waveguide and the MO-material-clad waveguide at

the edge of the Ce:YIG chip, which was ~ 0.2 dB per side for the $TE_0$ mode. (3) Due to insufficient NRPS, the forward transmission efficiency at the operation wavelength did not reach the maximum, resulting in an additional loss of ~0.8 dB.

Table.3-2 Loss Breakdown

| Origin of loss | Value(dB) |
|---|---|
| (1) Mode conversion | 0.6 |
| (2) Ce:YIG edge coupling | 0.4 |
| (3) Insufficient NRPS | 0.8 |
| (4) Out-device MO loss | 0.55 |
| (5) In-device MO loss | 2.65 |
| Total | 5 |

The remaining IL of 3.2 dB was attributed to the MO material absorption. To solve this part of the loss, we simulated the confinement factor of $mode_0$ and $mode_1$ in Ce:YIG layer under different waveguide structures in the device as shown in Fig.3-10 (a), and the propagation loss could be calculated by Eq.2-24. Combining with the experimental results, the $\alpha_{Ce:YIG}$ was calculated as ~64 dB/cm. The MO loss of $mode_0$ and $mode_1$ was 1.6 dB and 3.83 dB, respectively.

So, (4) The MO loss caused by additional covered input and output straight waveguide was ~0.55 dB.

(5) The in-device MO loss was ~2.65 dB which could be calculated by

$$T = \omega_0^2\alpha_0 + \omega_1^2\alpha_1 + 2\omega_0\omega_1\sqrt{\alpha_0\alpha_1}\cos(\varphi), \tag{3-1}$$

where $\omega_0$ and $\omega_1$ were the normalized energies of $mode_0$ and $mode_1$ respectively, both ideally 0.5; $\alpha_0$ and $\alpha_1$ were the transmission efficiencies of $mode_0$ and $mode_1$ respectively; and $\varphi$ was the overall phase difference between them, which was 0 in the forward transmission. And due to the imbalanced loss of the two modes, the light could not achieve complete extinction in backward transmission. By assuming $\varphi = \pi$ in Eq.3-1, the theoretical maximum IR was 17.8 dB, which was in line with the experimental results.

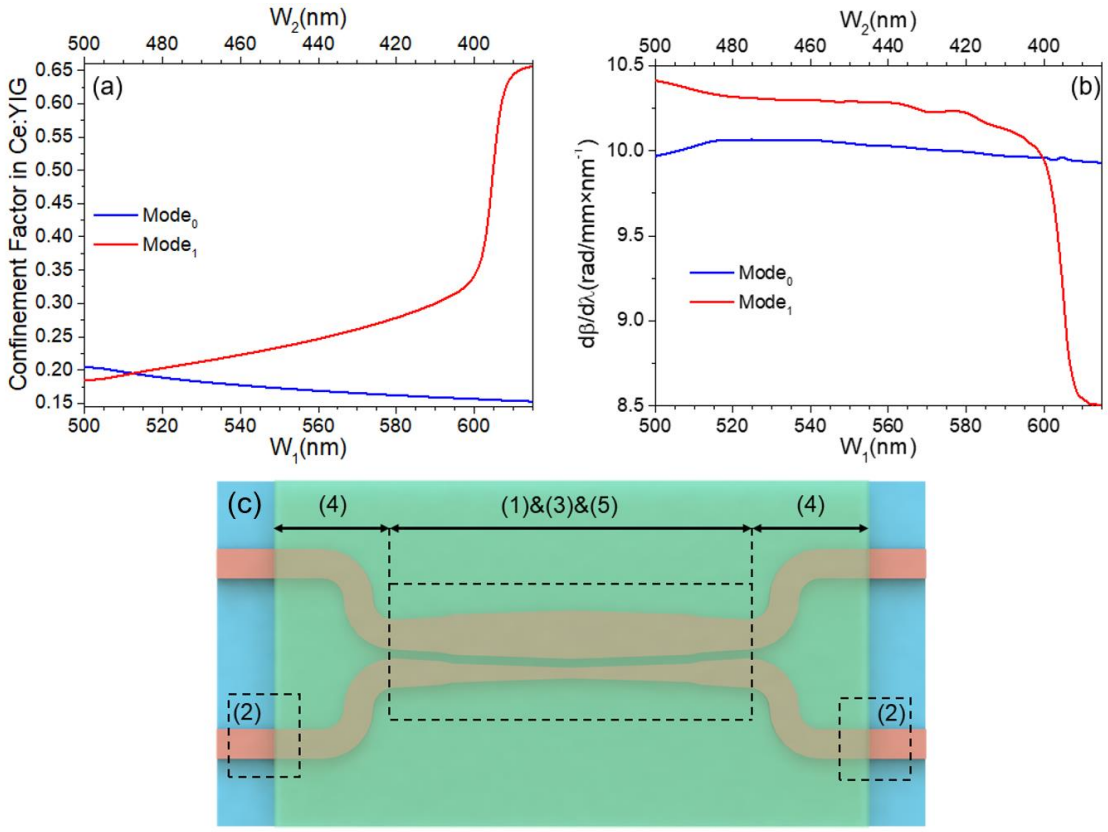


Fig.3-10 (a) Confinement factor in Ce:YIG layer and (b) dispersion of mode$_0$ and mode$_1$ under different waveguide width. (c) Insertion loss contributions to the isolator.

Finally, we theoretically calculated the bandwidth of the device. The bandwidth of the device was determined by the intermode dispersion between mode$_0$ and mode$_1$ as

$$\frac{d\phi}{d\lambda} = \int_L \frac{d(\beta_0 - \beta_1)}{d\lambda} dL, \tag{3-2}$$

where $\beta_0$ and $\beta_1$ were propagation constant of mode$_0$ and mode$_1$ respectively. By simulating the mode dispersion in the device as shown in Fig.3-10 (b), the intermode dispersion at the operation wavelength was ~0.565 rad/nm, and the corresponding 10-dB isolation bandwidth was 2.16 nm, which was almost similar to the experimental value of 2 nm.

## 3.7 Summary and prospect

In this chapter, we proposed a novel half-mode conversion TE-mode nonreciprocal device based on an asymmetric directional coupler. The device was fabricated by a CMOS-compatible process and could work under a unidirectional magnetic field, which simplified the difficulty of magnetic field integration. The device exhibited 15-dB IR and 5-dB IL when operating as a TE mode isolator.

The IL of the device was much lower than that of the reported half-mode conversion device [9], however, an unsatisfactory IR was due to the imbalanced intermode loss. At the same time, the device had a quasi-one-dimensional structure, which had its unique advantages in on-chip integration. By further optimization of bonding accuracy and NRPS design, losses (3) and (4) will be eliminated. Then the theoretical optimum IL and IR are 3.56 dB and 17.8 dB respectively [10].

This device structure was also expected to achieve polarization-independent nonreciprocal transmission operation. Ideally, when $TM_0$ was input, the $TM_{even}$ mode ($mode_2$) and $TM_{odd}$ mode ($mode_3$) at the input port would be excited, and finally converted to $TE_0$ and $TM_0$ modes in the narrow MO waveguide, and the NRPS would be accumulated to realize the TM-mode isolation operation (as shown in Fig.3-11). However, due to the waveguide size limitation, the MO waveguide only supports three eigenmodes ($mode_{0,1,2}$ as shown in Fig.3-4(a)), so the device could not work under TM-polarized light input based on the current structural parameters.

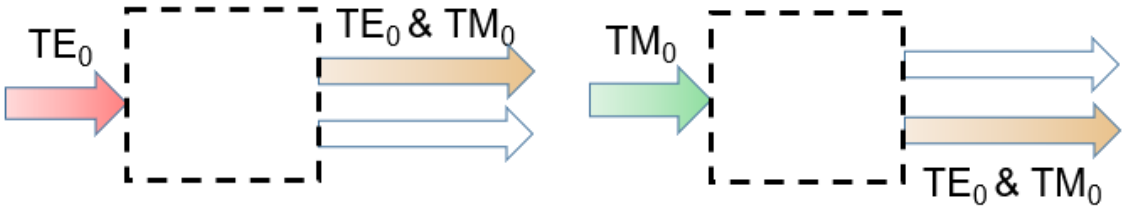


Fig.3-11 Mode conversion process of a polarization-independent nonreciprocal device.

One of the solutions was to increase the width of the two waveguides, but this would confine more energy of the modes into the core layer and made mode hybridization much more difficult, which eventually led to the length of the adiabatic mode converter becoming the order of tens of millimeters. The MO loss and the

imbalanced intermode loss would greatly restrict device performance.

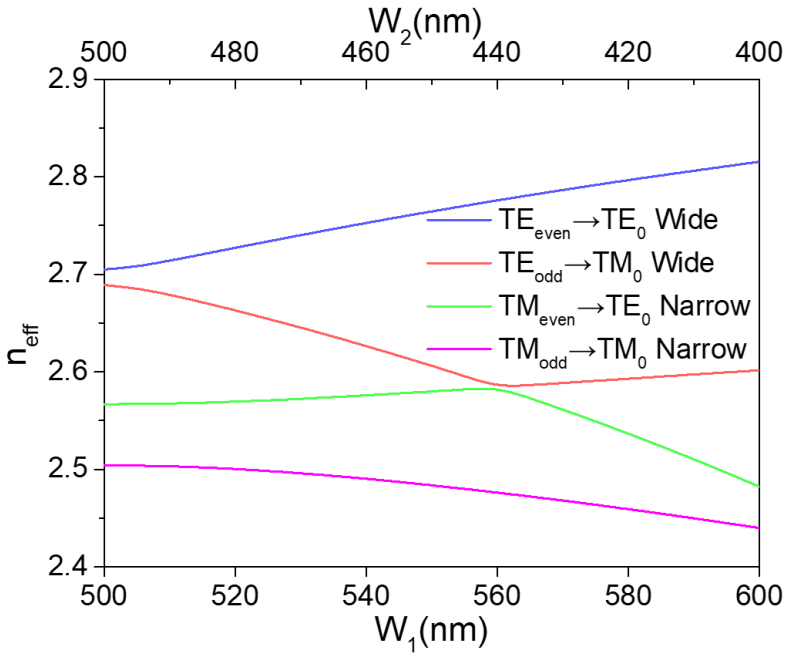


Fig.3-12 $n_{eff}$ of eigenmodes in a 300-nm-thick SOI waveguide varies with the waveguide width.

Another idea was to increase the height of the waveguide. When the waveguide height was ~300 nm, the narrow MO waveguide could also support the $TM_0$ mode. The specific parameters of the device were designed as shown in Table.3-3. The $n_{eff}$ of eigenmodes in MO waveguide varied with $W_1/W_2$ was simulated as Fig.3-12, show that the device could achieve the expected mode conversion. But in addition to the above-mentioned problem that the length of the adiabatic gradient coupler was too long, such a design also had other problems:

Table.3-3 Structural parameters of a polarization-independent nonreciprocal device

| Gap | $W_1$ | $W_2$ | $H_{Si}$ |
|---|---|---|---|
| 150 nm | 500 nm → 600 nm | 500 nm → 400 nm | 300 nm |

(1) The lengths of the nonreciprocal phase shifters for TE- and TM-mode inputs were the same but different in width, so the overall NRPS was difficult to keep consistent under TE- and TM-polarized light input.

(2) Most silicon-based integrated optical devices were designed on SOI wafers with a 220-nm-thick silicon layer, so there were compatibility issues in device cascading and unified process fabrication [11-15].

Therefore, the motivation to realize the integrated polarization-independent nonreciprocal device by the half-mode conversion is feasible, but further optimization of the design is still needed. The specific design scheme will be discussed in detail in Chapter 5.

## References


1. Chen R., Tao D., Zhou H., Hao Y., Yang J., Wang M. and Jiang X., "Asymmetric multimode interference isolator based on nonreciprocal phase shift." *Optics Communications* 282.5 (2009): 862-866. DOI: 10.1016/j.optcom.2008.11.064
2. Rickman A.G. and Reed G.T., "Silicon-on-insulator optical rib waveguides: loss, mode characteristics, bends and y-junctions." *IEE Proceedings-Optoelectronics* 141.6 (1994): 391-393. DOI: 10.1049/ip-opt:19941468
3. Gomi M., Furuyama H. and Abe M., "Strong magneto-optical enhancement in highly Ce-substituted iron garnet films prepared by sputtering." *Journal of Applied Physics* 70.11 (1991): 7065-7067. DOI: 10.1063/1.349786
4. Shintaku T. and Uno T., "Preparation of Ce-substituted yttrium iron garnet films for magneto-optic waveguide devices." *Japanese Journal of Applied Physics* 35.9R (1996): 4689. DOI: 10.1143/JJAP.35.4689
5. Holmes B.M., Naeem M.A., Hutchings D.C., Marsh J.H. and Kelly A.E., "A semiconductor laser with monolithically integrated dynamic polarization control." *Optics Express* 20.18 (2012): 20545-20550. DOI: 10.1364/OE.20.020545
6. Holmes B.M. and Hutchings D.C., "Realization of novel low-loss monolithically integrated passive waveguide mode converters." *IEEE Photonics Technology Letters* 18.1 (2005): 43-45. DOI: 10.1109/LPT.2005.859987
7. Yin Y., Li Z. and Dai D., "Ultra-broadband polarization splitter-rotator based on the mode evolution in a dual-core adiabatic taper." *Journal of Lightwave Technology* 35.11 (2017): 2227-2233. DOI: 10.1109/JLT.2017.2662200
8. Mitsuya K., Shoji Y. and Mizumoto T., "Demonstration of a silicon waveguide optical circulator." *IEEE Photonics Technology Letters* 25.8 (2013): 721-723. DOI: 10.1109/LPT.2013.2247995
9. Yamaguchi R., Shoji Y. and Mizumoto T., "Low-loss waveguide optical isolator with tapered mode converter and magneto-optical phase shifter for TE mode input." *Optics Express* 26.16 (2018): 21271-21278. DOI: 10.1364/OE.26.021271
10. Liu S., Shoji Y. and Mizumoto T., "Mode-evolution-based TE mode magneto-optical isolator using asymmetric adiabatic tapered waveguides." *Optics Express* 29.15 (2021): 22838-22846. DOI: 10.1364/OE.427914
11. Zhang C., Xiang Y., Liu S., Liu D., Yan H., Peng Y., Li H., Shi Y., Liu L., Kumar R., Panepucci R.R. and Dai D., "Silicon Photonic Wavelength-Selective Switch Based on an Array of Adiabatic Elliptical-Microrings." *Journal of Lightwave Technology* (2023). DOI: 10.1109/JLT.2023.3264613
12. Liu D., Zhang L., Tan Y. and Dai D., "High-order adiabatic elliptical-microring filter with an ultra-large free-spectral-range." *Journal of Lightwave Technology* 39.18 (2021): 5910-5916. DOI: 10.1109/JLT.2021.3091724
13. Cheng J., Zhang W., Gu W., Zhou H., Dong J. and Zhang X., "Photonic emulator for inverse design." *ACS Photonics* (2022). DOI: 10.1021/acsphotonics.2c00716

14. Dai D. and Bowers J.E., "Novel concept for ultracompact polarization splitter-rotator based on silicon nanowires." *Optics Express* 19.11 (2011): 10940-10949. DOI: 10.1364/OE.19.010940
15. Yang S., Zhang Y., Grund D.W., Ejzak G.A., Liu Y., Novack A., Prather D., Lim A.E.J., Lo G.Q., Baehr-Jones T. and Hochberg M., "A single adiabatic microring-based laser in 220 nm silicon-on-insulator." *Optics Express* 22.1 (2014): 1172-1180. DOI: 10.1364/OE.22.001172

# Chapter IV

# Microring-resonator-based isolator

## 4.1 Introduction

In this chapter, we will optimize the performance and magnetic field integration of narrowband MRR-based MO isolators. Before discussing device design, we will briefly explain the working principle and transmission formula of MRR.

Figure 4-1 shows a simple MRR structure and its performance parameters. The amplitude relationship of its coupling region is

$$\begin{aligned} b_1 &= ta_1 + k^* a_2 \\ b_2 &= t^* a_2 - ka_1 \end{aligned}, \tag{4-1}$$

where $a_1$, $a_2$, $b_1$, and $b_2$ is the normalized amplitude of each port. t, $t^*$ and k, $k^*$ are the self-coupling coefficients and cross-coupling coefficients between the straight waveguide and the microring, respectively, and satisfy

$$|k|^2 + |t|^2 = 1, \tag{4-2}$$

and

$$\begin{aligned} |k| &= |k^*| \\ |t| &= |t^*| \end{aligned}. \tag{4-3}$$

$a_2$, $b_2$ satisfy the relation

$$a_2 = \alpha e^{i\varphi} b_2, \tag{4-4}$$

where $\alpha$ is the attenuation coefficient of the microring, and $\varphi$ is the phase delay of one cycle. Solve the transmittance as

$$|b_1|^2 = \frac{\alpha^2 + |t|^2 - 2\alpha|t|\cos(\varphi)}{1 + \alpha^2|t|^2 - 2\alpha|t|\cos(\varphi)}. \tag{4-5}$$

When the wavelength satisfies the resonance condition $\varphi = 2n\pi$, Eq.4-5 can be written as

$$|b_1|^2 = \frac{(\alpha - |t|)^2}{(1-\alpha|t|)^2}. \tag{4-6}$$

If and only when the attenuation coefficient $\alpha$ of the microring is equal to the self-coupling coefficient $|t|$ of the coupler, the critical coupling condition is met, and the output light intensity will be 0. That is, the transmission light field $ta_1$ in the straight waveguide is destructive interference with the coupled field $ka_2$ from the microring [1-4]. The light confined into microring is attenuated by the internal loss when there is not any other coupled waveguide.

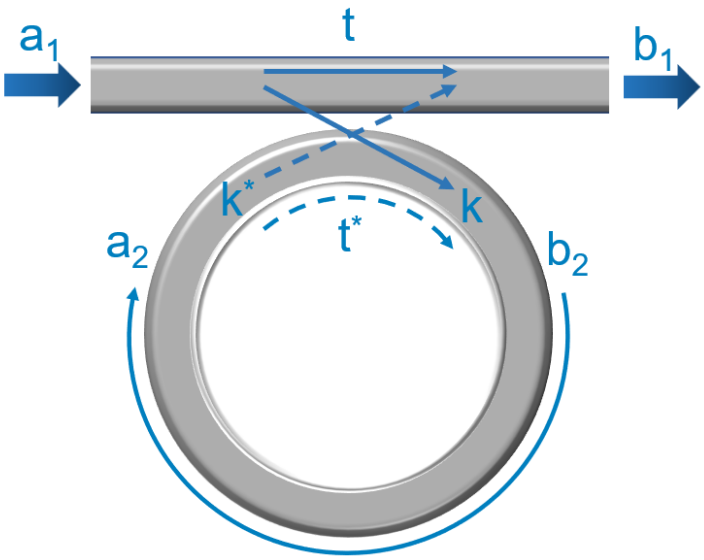


Fig. 4-1 The structure and t performance parameters of a microring resonator.

Considering such an TM-mode MRR-based isolator, after integrating the MO material upper cladding by wafer bonding and applying a radial direction magnetic field, due to the NRPS of the $TM_0$ mode in the microring, the phase delay $\varphi$ of the light propagating in the CW and CCW directions in the microring will be different, which leads to the nonreciprocal transmittance between forward and backward transmission. However, due to the symmetrical microring structure, if a unidirectional magnetic field is applied, the overall NRPS in the microring will be 0, so additional fabrication processes are indispensable for integrating Au wires or permanent magnet

materials to achieve a radial direction magnetic field (as shown in Fig.4-2 (a)) [5].

To realize the low-loss TE-mode MRR isolator working under a unidirectional magnetic field, we proposed some novel designs: first, to realize NRPS accumulation under a unidirectional magnetic field, we designed an asymmetric microring structure as shown in Fig.4-2 (b). One side of the microring transmitted $TE_1$ mode and the other side transmitted $TM_0$ mode. The mode conversion of the two modes could be achieved by an adiabatically tapered waveguide; then, to reduce the IL introduced by the additional series PRs [6-9], we combined the PRs with the coupler, when $TE_0$ mode was input from the straight waveguide, the coupler could convert and couple light into the microring as $TE_1$ mode while meeting the critical coupling conditions; finally, since only the $TE_0$ mode propagated in the input/output straight waveguide, the MO loss in the straight waveguide and the junction loss at the edge of Ce:YIG could be reduced.

Herein, we will show the working principle and structural parameter design of the novel MRR-based isolator in detail. The measured performance of the proposed device; and its compatibility under the external-fab process will be discussed.

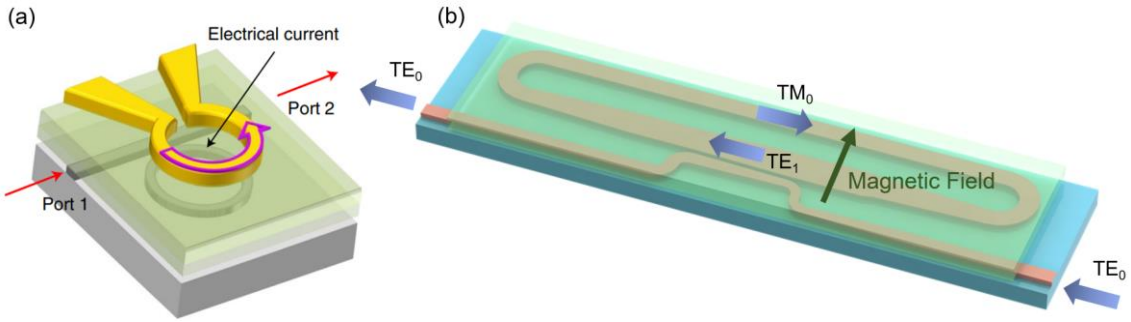


Fig. 4-2 (a) MRR nonreciprocal device fabricated by wafer bonding, the radial magnetic field was integrated by Au wires [5]. (b) The novel MRR nonreciprocal device fabricated by wafer bonding under a unidirectional magnetic field.

## 4.2 Device structure and operation principle

Fig. 4-3(a) is the structure of the proposed device. The device consisted of a straight input/output waveguide and an asymmetric microring with widths of $W_S$ and $W_R$, respectively, and the gap between them was designed to be 200 nm. The device

was fabricated on a standard SOI substrate with a Si core layer thickness of 220 nm and a 3-μm-think $SiO_2$ buried layer. Ce:YIG was bonded to the SOI substrate as a top cladding to achieve the NRPS of TM fundamental mode. The cross-section of the MO waveguide is shown in Fig. 4-3(b).

According to the designed mode conversion, the lower waveguide of the microring was divided into six parts, *i.e.*, $Part_{1\text{-}6}$. $TE_0$ mode input from the straight waveguide (as shown in Fig.4-3 (c)), and partial energy was converted into the $TE_1$ mode (as shown in Fig.4-3 (d)) by the $TE_0$ & $TE_1$ mode coupler at $Part_4$ and coupled into the microring. $Parts_{3,5}$ are buffer areas to ensure that the total length of the microring was fixed when the length of the coupler $L_4$ changes. The $TE_1$ & $TM_0$ mode converter at $Part_1$ converted the $TE_1$ mode to $TM_0$ mode (as shown in Fig.4-3 (e)) and propagated in the upper waveguide to accumulate a designed NRPS of $\pi$. By a reverse mode conversion process, partial energy was coupled back into the straight waveguide as $TE_0$ mode and interfered with self-coupled light and output.

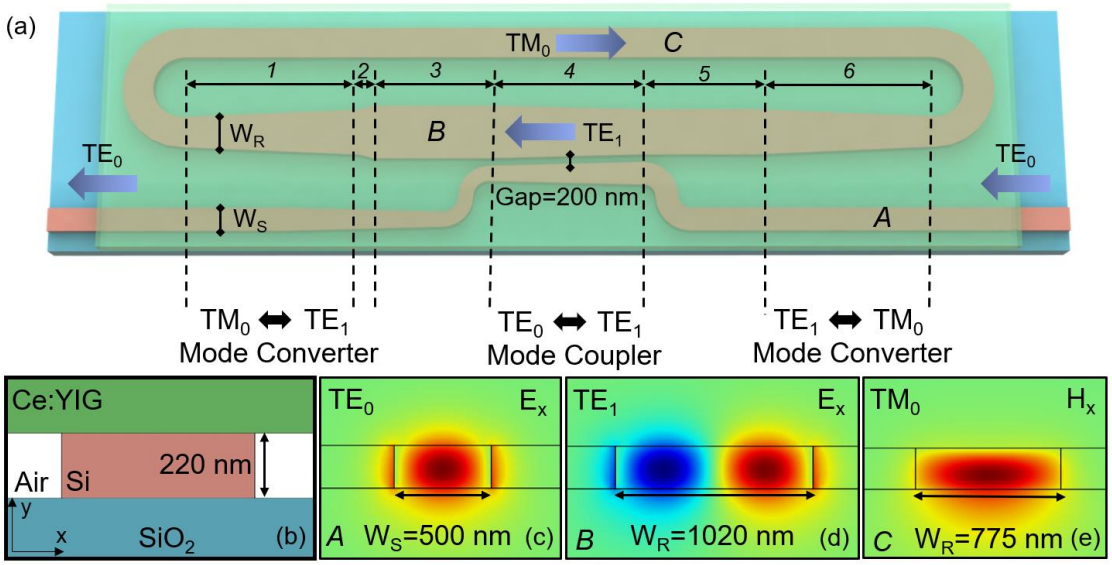


Fig. 4-3 (a) Top view of the device, the lower waveguide in the MRR was divided into six parts ($Part_{1\text{-}6}$) for designed mode conversion. (b) Cross-section of the magneto-optical waveguide. Mode field distribution at specific locations (c) A, (d) B, and (e) C, as shown in (a).

## 4.3 Simulation and parameter design

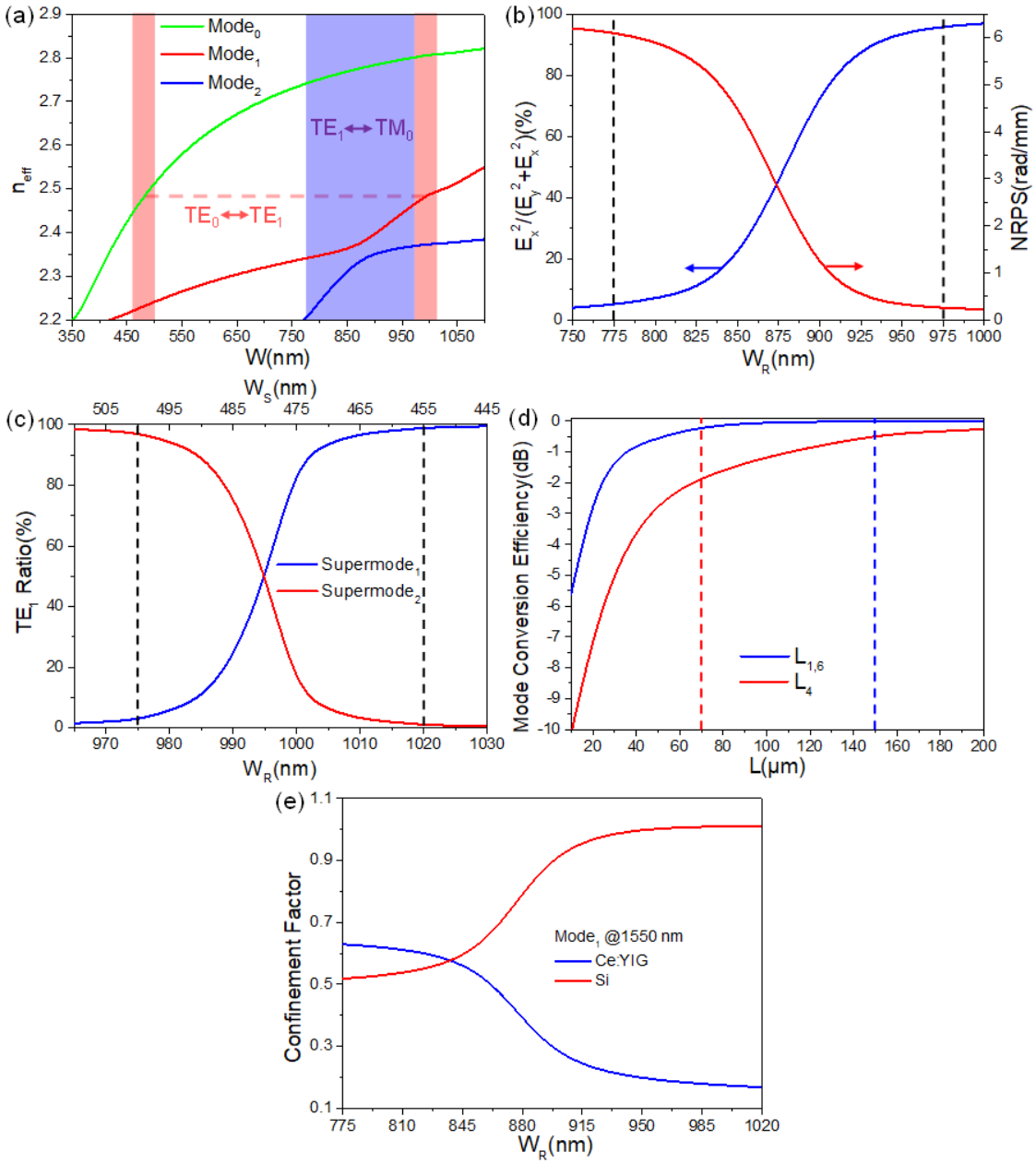


Fig. 4-4 (a) $n_{eff}$ of the eigenmodes varies with the waveguide width of a single MO waveguide. (b) The TE ratio ( $E_x^2 / (E_x^2 + E_y^2)$ )and NRPS of mode$_1$ as a function of the microring width $W_R$. (c) The TE$_1$ ratio of TE$_0$-TE$_1$ supermodes in the coupler varies with $W_R$. (d) Mode conversion efficiency as a function of $L_{1,6}$ and $L_4$. (e) The confinement factor of mode$_1$ in the Ce:YIG layer and Si layer varies with $W_R$.

The materials parameter used in the simulation were $n_{Si} = 3.48$, $n_{SiO_2} = 1.444$, and $n_{Ce:YIG} = 2.2$. The FR of Ce:YIG was assumed as 4500 °/cm.

The $TE_1$ & $TM_0$ mode converter and $TE_0$ & $TE_1$ mode coupler were designed by adiabatic mode evolution to achieve a low-loss and broadband operation. Simulating the $n_{eff}$ in a single MO waveguide varies with the waveguide width as shown in Fig.4-4 (a). The mode converter was designed by selecting a width range around the hybridization point of $TE_1$ and $TM_0$ modes, where the $n_{eff}$ of $mode_1$ and $mode_2$ were close (purple area); the mode coupler was realized by designing the $TE_0$ and $TE_1$ modes with the same $n_{eff}$ in two MO waveguides (pink area).

For the width design of the mode converter, the TE ratio of $mode_1$ near the hybridization point as the $W_R$ change was simulated as shown in the blue curve in Fig.4-4 (b). And we selected the TE ratio from 5% to 95% as the starting and ending widths of the mode converter corresponding to 775 nm and 975 nm, respectively.

For the width design of the mode coupler, we first fixed the waveguide width $W_S/W_R$ at one end as 500 nm/975 nm, which was consistent with the width of the straight waveguide and the mode converter respectively. Under this width, almost no mode coupling occurred between the straight waveguide and microring. Then keep the sum of $W_R$ and $W_S$ constant, and as $W_R$ increases ($W_S$ decreases), the $TE_1$ mode in the microring would couple with the $TE_0$ mode in the straight waveguide as $supermode_1$ ($TE_0$+$TE_1$) and $supermode_2$ ($TE_0$-$TE_1$). By simulating the $TE_1$ ratio of supermodes variation with different $W_R/W_S$ as shown in Fig.4-4 (c), the width $W_R/W_S$ at the other end could be designed as 1020 nm/455 nm, where the $TE_1$ ratio corresponding to the two supermodes were 99% and 1% respectively to ensure that there was almost no mode coupling under this width design.

For the length design, the mode converter only needed to satisfy the adiabatic evolution condition. By simulating the mode conversion efficiency with different lengths $L_{1,6}$ of the mode converter as shown in Fig4-4 (d), the $L_{1,6}$ was designed to be 150 μm to achieve a lossless mode conversion. And $Part_2$ involved no mode conversion, so $L_2$ was designed to be 30 μm to ensure a negligible loss.

The total length of the microring was determined by simulating the NRPS of the $TM_0$ mode in the 775 nm wide MO waveguide of 6.1 rad/mm as the red curve shown

in Fig.4-4 (b), so the length of the upper MO waveguide of microring was designed to be 510 μm. The bending waveguide radius was designed to be 50 μm so the bending loss could be ignored.

The mode coupler length $L_4$ should meet the critical coupling condition. Considering Eq.4-6, the coupling efficiency should be equal to the attenuation coefficient $\alpha$ of the microring to achieve a complete light extinction in the backward transmission. The $\alpha$ could be calculated by the confinement factor and material loss. We assumed material losses of Si and Ce:YIG as $\alpha_{Si}$ =3 dB/cm and $\alpha_{Ce:YIG}$ =60 dB/cm; and simulated the confinement factors of mode$_1$ in the two material layers under different $W_R$ as shown in Fig.4-4 (e). Combined with Eq.2-24, the attenuation coefficient of the microring can be calculated by

$$\alpha = \int (\Gamma_{Si}(L)\alpha_{Si} + \Gamma_{Ce:YIG}(L)\alpha_{Ce:YIG})dL, \tag{4-7}$$

where the path of integration was one circle of the microring. The calculated $\alpha$ was 0.61. Due to the high confinement of the TE mode in the Si layer and the buffer area design, the effect of the $L_4$ on $\alpha$ was negligible. The corresponding mode conversion efficiency of the coupler was estimated to be ~-2 dB. From the mode conversion efficiency as a function of coupler length $L_4$ as shown by the red line in Fig.4-4 (d), $L_4$ was designed to be 70 μm. Due to the limitation of the total length of the microring, the buffer area length $L_{3,5}$ was calculated to be 55 μm. The structural parameters are shown in Table.4-1.

Table.4-1 Structural parameters

| $Part_i$ | $W_R$ ($W_S$) (nm) | $L_i$ (μm) |
|---|---|---|
| $Part_{1,6}$ | 975 → 775 | 150 |
| $Part_2$ | 1020 → 975 | 30 |
| $Part_3$ / $Part_5$ | 1020 / 975 | 55 |
| $Part_4$ | 975 (500) → 1020 (455) | 70 |

Based on the above parameters. We simulated the transmission field distribution of the mode converter and mode coupler as shown in Fig. 4-5, and the components could work as expected.

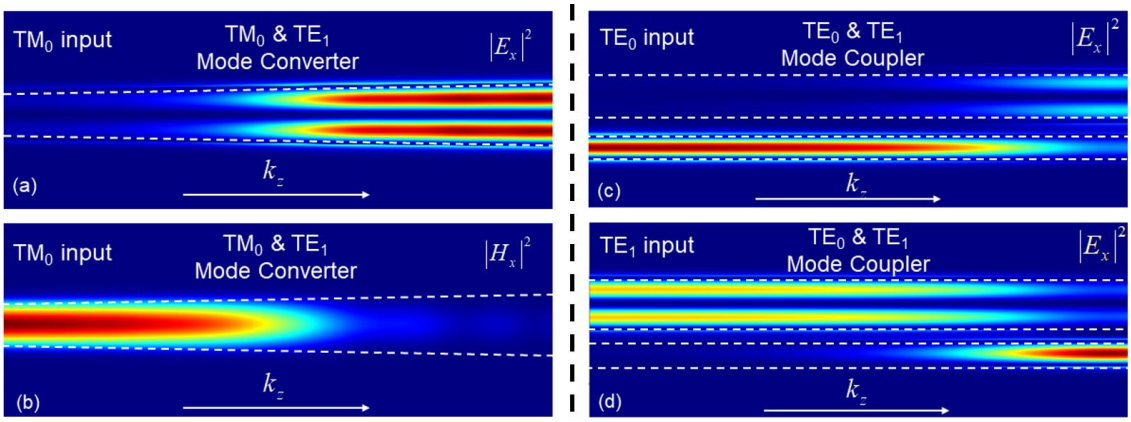


Fig. 4-5 The (a) $E_X$ and (b) $H_X$ field distribution of the mode converter with $TM_0$ mode input. The $E_X$ field distribution of the mode coupler with (c) $TE_0$ and (d) $TE_1$ modes input.

## 4.4 Experiment and device characterization

The device fabrication process is shown in Fig. 4-6, which is the same as that in Chapter 3 and will not be repeated here.

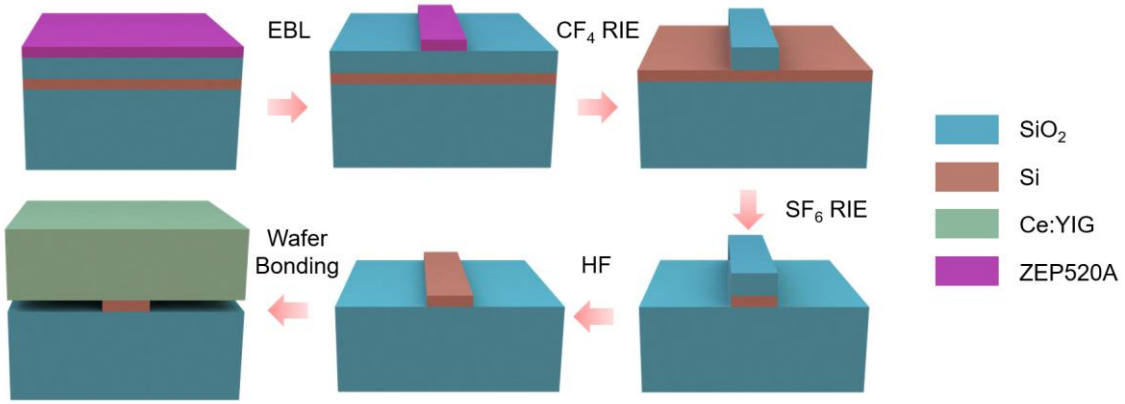


Fig. 4-6 Processing flow.

The micrograph of the device is shown in Fig.4-7 (a), where the green square was the bonded Ce:YIG/SGGG chip; the blue arrows indicated the direction of the applied magnetic field. Considering the fabrication error, the coupler length $L_4$ had different offsets to ensure that some devices could satisfy the critical coupling conditions. The performance of the device was roughly measured by the polarization-maintaining fiber system after the application of an external magnetic field, and it was found that

the IR of the device was higher when $L_4$ was 82~94 μm, and the corresponding device spectra were shown in Fig.4-7 (b).

The measured IR corresponding to different $L_4$ is shown in Fig.4-8 (a), so we inferred that the critical coupling condition could be satisfied when $L_4$ was ~90 μm. This deviation from the design value was due to fabrication errors, which will be discussed in detail in the next section. Therefore, we prepared several groups of devices with $L_4$=90 μm and tested them by the focusing lenses containing polarizers to improve the TE polarization purity of input light, and finally obtained the forward and backward transmission spectra of the device as shown by the red and blue curves in Fig.4-8 (b). The IR was 22 dB at a wavelength of 1572.62 nm. The green curve was the spectrum of a reference waveguide to determine the IL of the device, which was 4.3 dB at the operation wavelength.

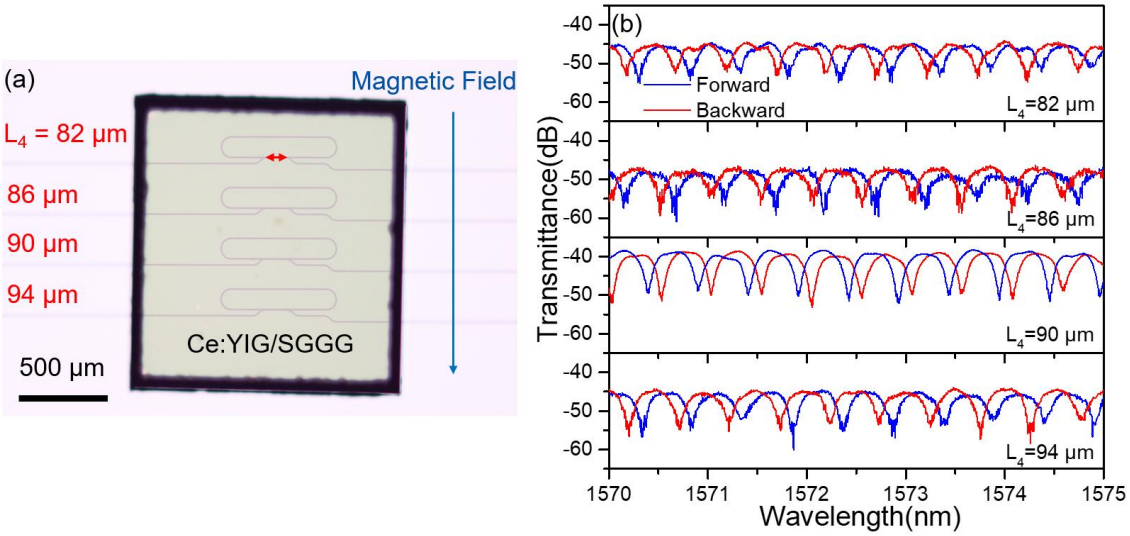


Fig. 4-7 (a) Micrograph of fabricated devices with different $L_4$. The blue arrow indicates the direction of the applied magnetic field. (b) Transmission spectra of the isolators in forward and backward transmission with different $L_4$.

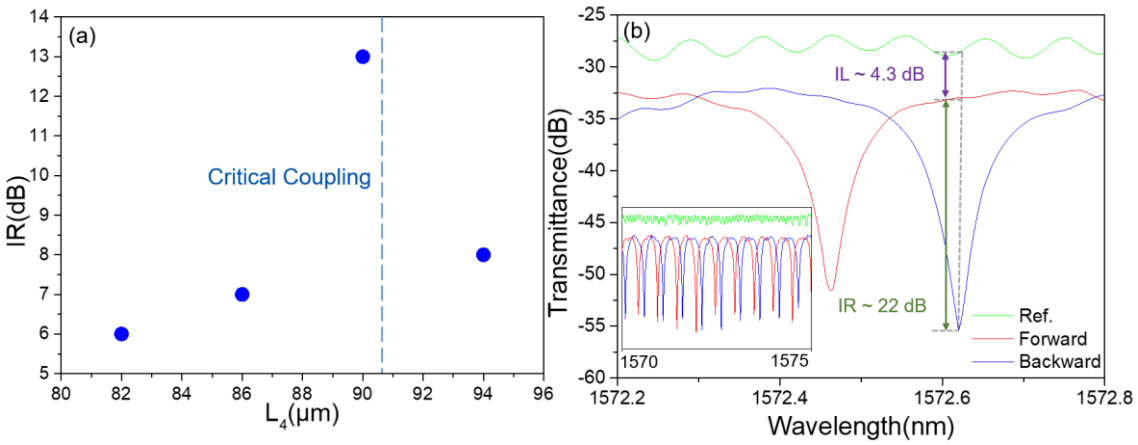


Fig. 4-8 (a) The corresponding relationship between IR and $L_4$, the dotted line indicates that the critical coupling length $L_4$ should be ~90 μm. (b) The transmission spectra of the isolators in forward and backward transmission, and the transmission spectrum of reference waveguide.

## 4.5 Discussion

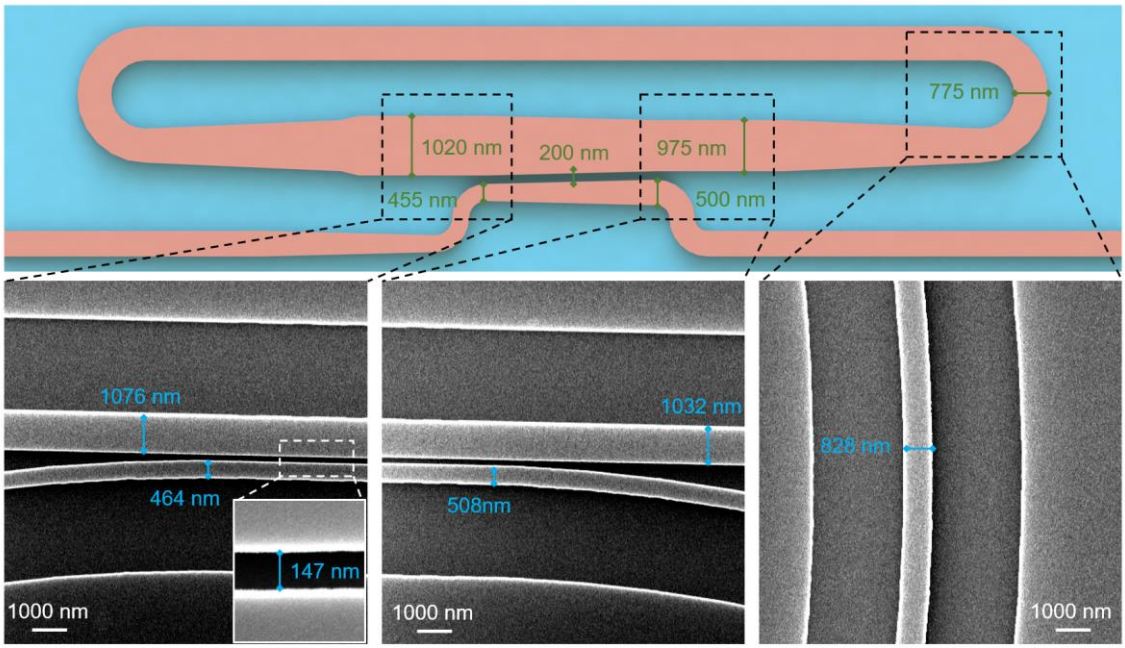


Fig. 4-9 The design width at specific locations compared with the actual width tested by SEM.

First, we analyzed the design and experimental deviation of $L_4$. By comparing the actual waveguide size at a specific position with the design value by SEM as shown

in Fig.4-9. We found that the actual size of the waveguide was slightly wider than the design value, so based on the actual waveguide size and operation wavelength, the self-coupling coefficient $|t|$ of the coupler was simulated as 0.63. Simultaneously, the corresponding confinement factors of mode$_1$ in the Si and Ce:YIG layers under different waveguide structures at the operation wavelength were simulated as shown in Fig.4-10. The attenuation coefficient $\alpha$ of the microring was also ~0.63 by Eq.4-7 calculation, which satisfies the critical coupling condition $\alpha = |t|$.

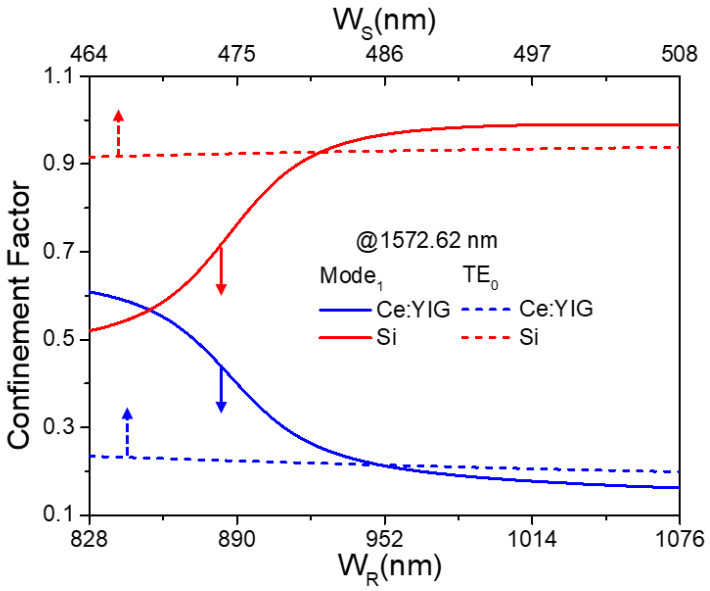


Fig. 4-10 The confinement factor of mode$_1$ in the Ce:YIG layer and Si layer varies with the $W_R$ based on the actual width and actual operating wavelength.

Then we broke down the IL: (1) The loss of the microring resonator at the nonresonant wavelength could be calculated as 0.9 dB by bringing $\alpha = |t| = 0.63$ and $\varphi = (2n+1)\pi$ into Eq.4-5. This value was much lower than the propagation loss in one cycle of the microring because only partial input energy was coupled into the microring, and the rest energy did not experience the propagation loss of the microring. (2) Due to insufficient NRPS, the forward transmittance at the operation wavelength did not reach the maximum value resulting in an IL of 0.7 dB. This was mainly because the TM component of the hybrid mode in the mode converter of Part$_{1,6}$ gets an NRPS (as the red curve shown in Fig.4-4 (b)) and the sign was opposite to the

NRPS of the $TM_0$ in the upper waveguide turned round along the microring. (3) The MO loss in the input/output straight waveguide with bonded Ce:YIG top cladding was ~2.3 dB. (4) The junction loss due to the mode field mismatching of the $TE_0$ mode between MO material cladding and air cladding waveguide at the edge of the Ce:YIG was 0.2 dB per edge, totaling 0.4 dB. The overall loss breakdown of the isolator was listed in Table.4-2.

If the wafer bonding accuracy can be further optimized, such as by μ-transfer printing, the IL will be significantly reduced by only covering the upper waveguide of the microring with MO material. Under such a structure, MO loss in input/output waveguides will be eliminated. Since there is no NRPS in the mode converter, IL due to insufficient NRPS is also eliminated; and IR will be also slightly improved. Junction loss will be calculated into propagation loss of the microring. In this case, the junction loss of $TM_0$ mode will be 1.5 dB per edge, resulting in a total propagation loss of 5 dB corresponding to an attenuation factor of 0.56 in the microring. So, the IL at the nonresonant wavelength can be calculated to be 1.4 dB by Eq.4-5. Therefore, the performance of the isolator still has a potential for improvement.

Table.4-2 Loss breakdown

| Origin of loss | Value (dB) |
|---|---|
| Loss of MRR | 0.9 |
| Insufficient NRPS | 0.7 |
| MO loss in input/output waveguide | 2.3 |
| Ce:YIG edge junction | 0.4 |
| Total | 4.3 |

## 4.6 External-fab compatibility

The proposed configuration had great application potential to replace the existing TE-mode isolator, so we tried to prepare it by external-fab process. Since the fabrication accuracy of the waveguide width in the external-fab process was higher than that in the laboratory, the coupler length $L_4$ was still designed as 70 μm in the external-fab layout.

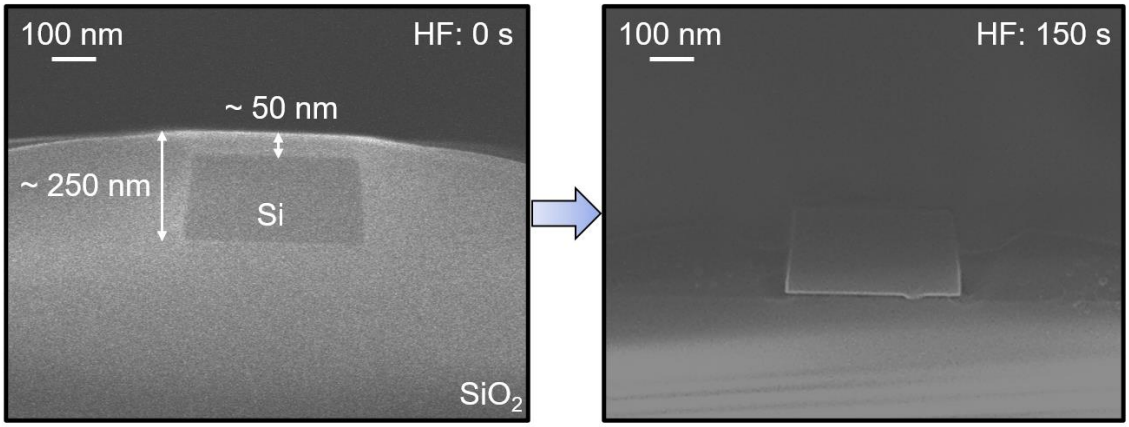


Fig. 4-11 SEM photos of the cross-section of the MO material integration window of the external-fab chip, (a) untreated and (b) HF solution wet etching for 150 s.

The problem was that silicon photonics fab bases circuits integration and silicon waveguides are covered by $SiO_2$ cladding layer for passivation and protection. It must be partially removed by alignment lithography for MO material integration at the back-end-of-line (BEOL) process. The external fab of AIST we used in this time provided deep etching for the window structure but a little amount of $SiO_2$ was remained.

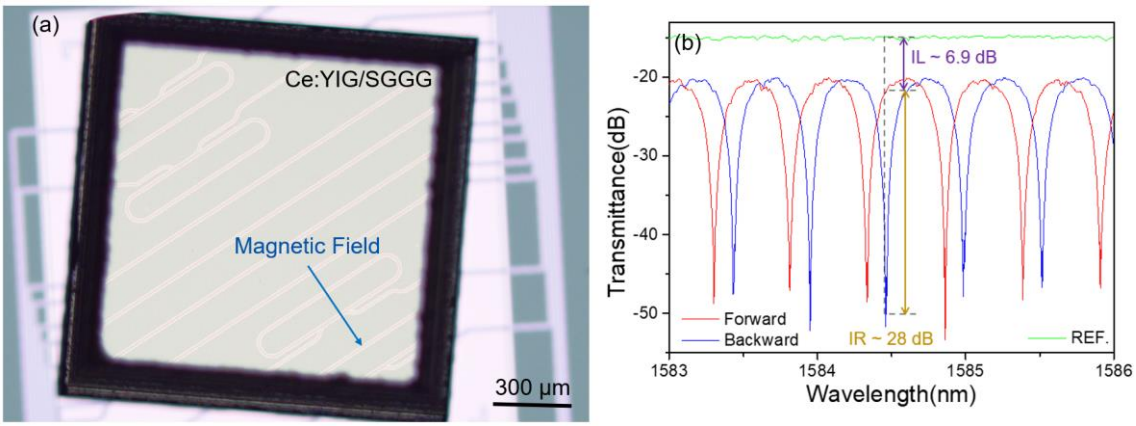


Fig.4-12 (a) Micrograph of fabricated devices on the external-fab chip. (b) Transmission spectra of reference waveguide and isolator in forward and backward transmission on the external-fab chip.

The waveguide in the window area of the external-fab chip is shown in Fig.4-11

(a). There was still a $SiO_2$ cladding layer of ~50 nm on the topwall of the waveguide. This was because the etching rate of $SiO_2$ was non-wafer-level uniform and difficult to strictly control. And the excessive etching would damage the waveguide structure. Therefore, we first performed HF(1:19) solution wet etching for 150 s to expose the topwall of the waveguide as shown in Fig.4-11 (b).

Afterward, Ce:YIG/SGGG chips were integrated by surface-active wafer bonding to complete the device preparation, and its micrograph is shown in Fig.4-12 (a). The forward and backward transmission spectra of the device and the transmission spectrum of the reference waveguide are shown in Fig.4-12 (b). The external-fab device had an IR of 28 dB and an IL of 6.9 dB. The loss was slightly higher than expected due to the scattering loss caused by the uneven sidewall $SiO_2$ structure of the waveguide as shown in Fig.4-11 (b). If a chemical mechanical polishing (CMP) step can be added before the window structure etching, it might be possible to eliminate this problem [10-12].

## 4.7 Summary

In this chapter, we proposed a novel asymmetric microring design to address the problems faced by the reported narrowband MRR-based nonreciprocal devices, *e.g.*, the poor performance of TE-mode devices and complex magnetic field integration. After the working principle of the device was shown, we discussed the design principle and structural parameters of each component in detail. Finally, the device demonstrated an ultra-high performance of 22-dB IR and 4.3-dB IL in laboratory preparation and was expected to reduce IL to 1.4 dB after the bonding accuracy was further improved [13]. In the follow-up external-fab experiment, the device also demonstrated the feasibility of its BEOL integration by the standard CMOS process and showed an IR of 28 dB and an IL of 6.9 dB.

## References


1. Bogaerts W., De Heyn P., Van Vaerenbergh T., De Vos K., Kumar Selvaraja S., Claes T., Dumon P., Bienstman P., Van Thourhout D. and Baets R., "Silicon microring resonators." *Laser & Photonics Reviews* 6.1 (2012): 47-73. DOI: 10.1002/lpor.201100017
2. Heebner J., Grover R. and Ibrahim T., "Optical microresonator theory." *Springer New York*, (2008). DOI: 10.1007/978-0-387-73068-4_3
3. Schwelb O., "Transmission, group delay, and dispersion in single-ring optical resonators and add/drop filters-a tutorial overview." *Journal of Lightwave Technology* 22.5 (2004): 1380-1394. DOI: 10.1109/JLT.2004.827666
4. Bogaerts W., Dumon P., Van Thourhout D., Taillaert D., Jaenen P., Wouters J., Beckx S., Wiaux V. and Baets R.G., "Compact wavelength-selective functions in silicon-on-insulator photonic wires." *IEEE Journal of Selected Topics in Quantum Electronics* 12.6 (2006): 1394-1401. DOI: 10.1109/JSTQE.2006.884088
5. Pintus P., Ranzani L., Pinna S., Huang D., Gustafsson M.V., Karinou F., Casula G.A., Shoji Y., Takamura Y., Mizumoto T. and Soltani M., "An integrated magneto-optic modulator for cryogenic applications." *Nature Electronics* 5.9 (2022): 604-610. DOI: 10.1038/s41928-022-00823-w
6. Zhang J., Yu M., Lo G.Q. and Kwong D.L., "Silicon-waveguide-based mode evolution polarization rotator." *IEEE Journal of Selected Topics in Quantum Electronics* 16.1 (2009): 53-60. DOI: 10.1109/JSTQE.2009.2031424
7. Fukuda H., Yamada K., Tsuchizawa T., Watanabe T., Shinojima H. and Itabashi S.I., "Polarization rotator based on silicon wire waveguides." *Optics Express* 16.4 (2008): 2628-2635. DOI: 10.1364/OE.16.002628
8. Gao L., Huo Y., Harris J.S. and Zhou Z., "Ultra-compact and low-loss polarization rotator based on asymmetric hybrid plasmonic waveguide." *IEEE Photonics Technology Letters* 25.21 (2013): 2081-2084. DOI: 10.1109/LPT.2013.2281425
9. Aamer M., Gutierrez A.M., Brimont A., Vermeulen D., Roelkens G., Fedeli J.M., Hakansson A. and Sanchis P.,"CMOS compatible silicon-on-insulator polarization rotator based on symmetry breaking of the waveguide cross section." *IEEE Photonics Technology Letters* 24.22 (2012): 2031-2034. DOI: 10.1109/LPT.2012.2218593
10. Yan W., Yang Y., Liu S., Zhang Y., Xia S., Kang T., Yang W., Qin J., Deng L. and Bi L., "Waveguide-integrated high-performance magneto-optical isolators and circulators on silicon nitride platforms." *Optica* 7.11 (2020): 1555-1562. DOI: 10.1364/OPTICA.408458
11. Nanz G. and Camilletti L.E., "Modeling of chemical-mechanical polishing: A review." *IEEE Transactions on Semiconductor Manufacturing* 8.4 (1995): 382-389. DOI: 10.1109/66.475179
12. Zhao D. and Lu X., "Chemical mechanical polishing: theory and experiment." *Friction* 1 (2013): 306-326. DOI: 10.1007/s40544-013-0035-x

13. Liu S., Shoji Y. and Mizumoto T., "TE-mode magneto-optical isolator based on an asymmetric microring resonator under a unidirectional magnetic field." *Optics Express* 30.6 (2022): 9934-9943. DOI: 10.1364/OE.454751

# Chapter V

# Polarization-independent isolator

## 5.1 Introduction

Inspired by Chapter 3, the idea of half-mode conversion was a feasible scheme to realize polarization-independent MO isolators. However, the design of polarization rotation couplers (PRCs) still had problems due to the coupling difficulties between $TE_0$ and $TM_0$ modes resulting in a too-long coupler length for mode evolution.

In Chapter 4 we introduced the $TE_1$ mode as an intermediary to realize the PRC function by the mode conversion of $TE_0 \rightarrow TE_1 \rightarrow TM_0$ and $TM_0 \rightarrow TE_1 \rightarrow TE_0$. And the fabricated PRCs had ultrahigh mode conversion efficiency and broad operation bandwidth.

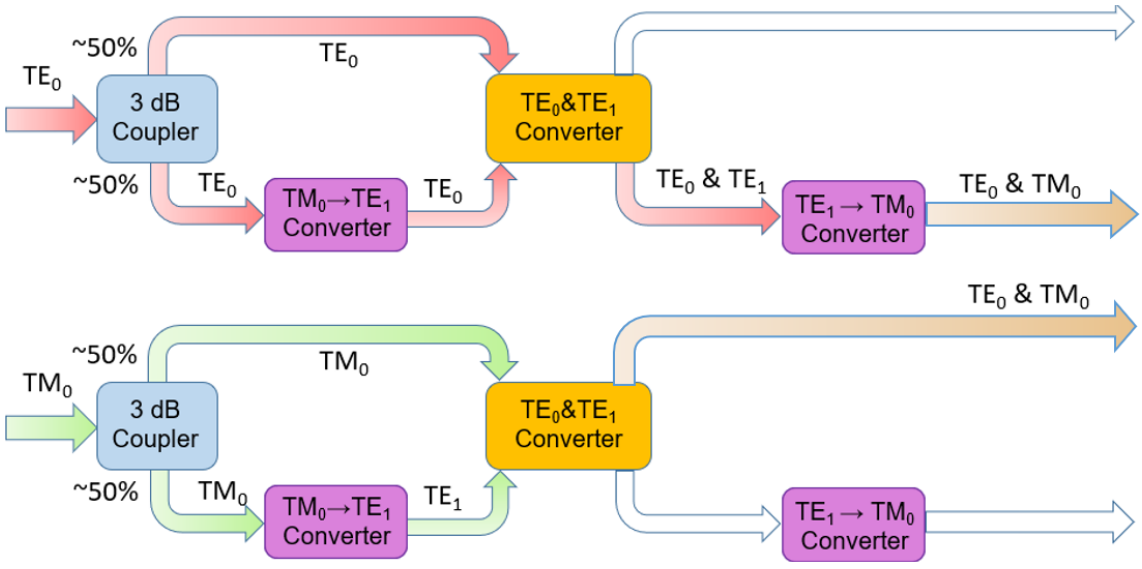


Fig.5-1 Mode conversion process in an SOI-based polarization-independent isolator based on half-mode conversion.

Therefore, combining the design inspirations from the above two chapters, we

proposed a polarization-independent half-mode converter designed by employing a polarization-independent 3-dB coupler and a $TE_1$-mode-intermediated PRC. The overall mode conversion diagram is shown in Fig.5-1. By such a mode conversion process, both TE- and TM-polarized inputs could be converted to equal-energy $TE_0$ and $TM_0$ modes in the individual nonreciprocal phase shifters for polarization-independent isolation operation.

Here we will discuss the working principle, design of the device, and the idea of reducing intermode crosstalk in the experiment; demonstrated the measured device performance; finally, conduct a theoretical analysis based on the device performance.

## 5.2 Device structure and operation principle

Figure 5-2 shows the structure of the proposed device. The device was designed on an SOI substrate with a 220-nm-thick patterned planar Si waveguide on a 3-μm-thick $SiO_2$ buried layer, and a bonded Ce:YIG/SGGG chip as upper cladding. The mode converters and couplers employed in the device were designed based on the idea of mode evolution, so the non-planar waveguide structure required by 90°-PR was not needed [1-3]. The device consisted of two polarization-independent half-mode converters on both the input and output side to divide the input light into $TE_0$ and $TM_0$ modes equally and couple them into one MO waveguide or interfere the phase-modulated light for output; and two nonreciprocal phase shifters to transmit the converted $TE_0$ and $TM_0$ mode under TE- and TM-polarized light inputs and accumulate the NRPS of $\pi$ required for the isolation operation after the MO material was magnetized by an external magnetic field.

There was a tricky design where the light propagation direction in the mode coupler and mode converter was orthogonal to that in the nonreciprocal phase shifter. Based on the theory in Chapter 2, under such a design the TE-TM hybrid mode in the mode conversion process would not contribute to the overall NRPS, but only the $TM_0$ mode in the nonreciprocal phase shifter could. On the one hand, this design simplified the calculation difficulty of the NRPS; on the other hand, ensured that the NRPS under TE- and TM-polarized inputs were consistent.

The polarization-independent half-mode converter consisted of a polarization-independent 3-dB coupler and a PRC [4]. The energy of the incident $TE_0$ or $TM_0$ mode would be divided equally into the two arms by the 3-dB coupler, after which the

polarization of mode in one arm was rotated and coupled into the other arm by the PRC to achieve the designed polarization-independent half-mode conversion operation as shown in Fig.5-3.

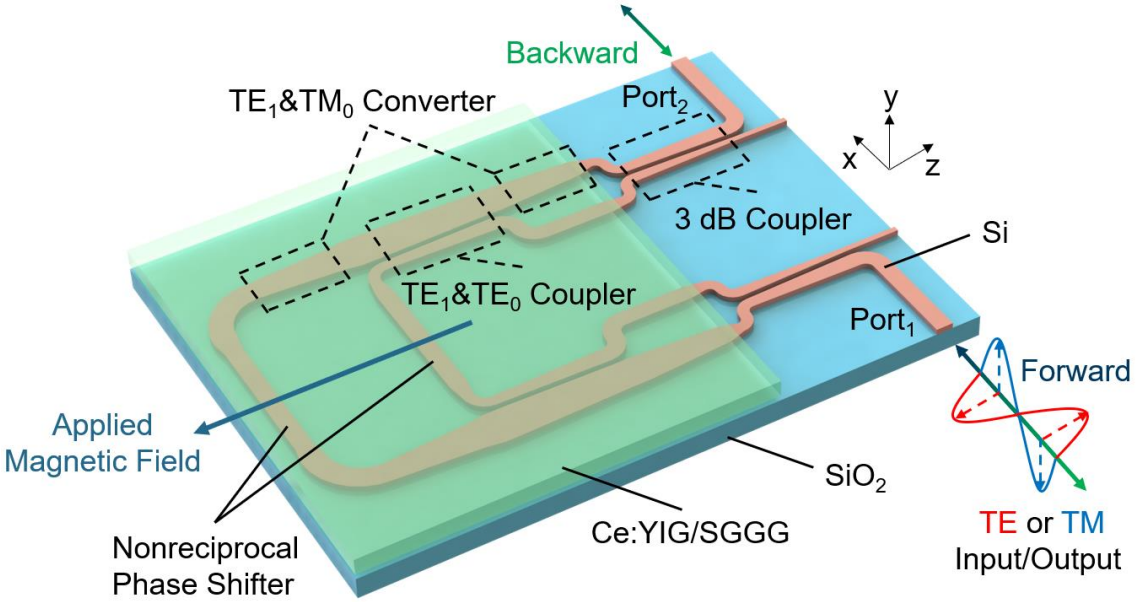


Fig.5-2 The device structure. The blue arrows indicate the direction of the applied magnetic field.

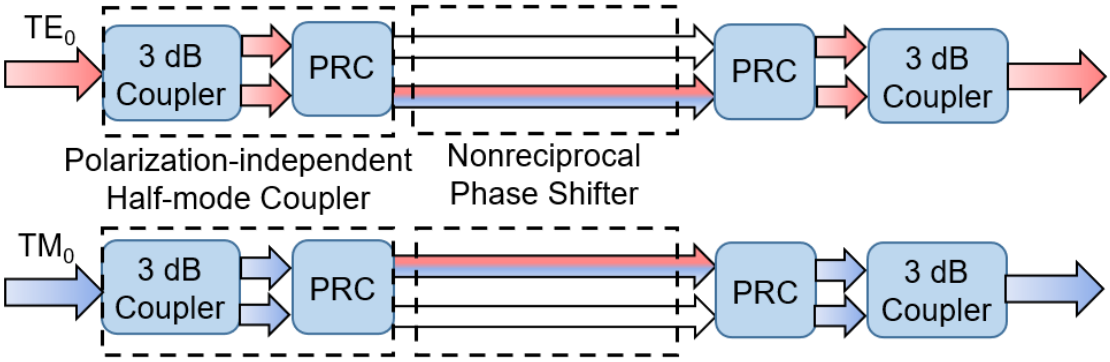


Fig.5-3 Mode conversion of the device under TE- and TM-polarized input.

By introducing the $TE_1$ mode as an intermediary to achieve the desired PRC. The specific mode conversion process of TE- or TM-polarized input light is shown in Fig.5-4 (a). The red and blue arrows corresponded to the mode conversion process corresponding to the TE- and TM-polarized input, respectively. The two interference modes were defined as $mode_1$ (upper-arm) and $mode_2$ (lower-arm), represented by

light and dark colors, respectively. When the $TE_0$ mode (as shown in Fig.5-4 (b))was input to the 3-dB coupler, due to the width difference between the two waveguides at the input end, only the $TE_0$ mode in the wide waveguide would be excited, and then the width of the two waveguides gradually approached by the adiabatically tapered waveguide, and the input $TE_0$ mode would be converted into $TE_{even}$ mode and evenly divided into two arms by the bending waveguide. The two-arm waveguides after width adjustment converged to the $TE_1$&$TE_0$ coupler, where the $TE_0$ mode of the upper-arm waveguide coupled and converted to the $TE_1$ mode (as shown in Fig.5-4 (e)) of the lower-arm waveguide, while the $TE_0$ mode (as shown in Fig.5-4 (d)) in the lower-arm waveguide propagated straightly. Finally, by the $TE_1$&$TM_0$ converter, the equal-energy $TE_0$ and $TM_0$ modes (as shown in Figs.5-4 (f) and (g)) were realized and entered the nonreciprocal phase shifter from *Position E*.

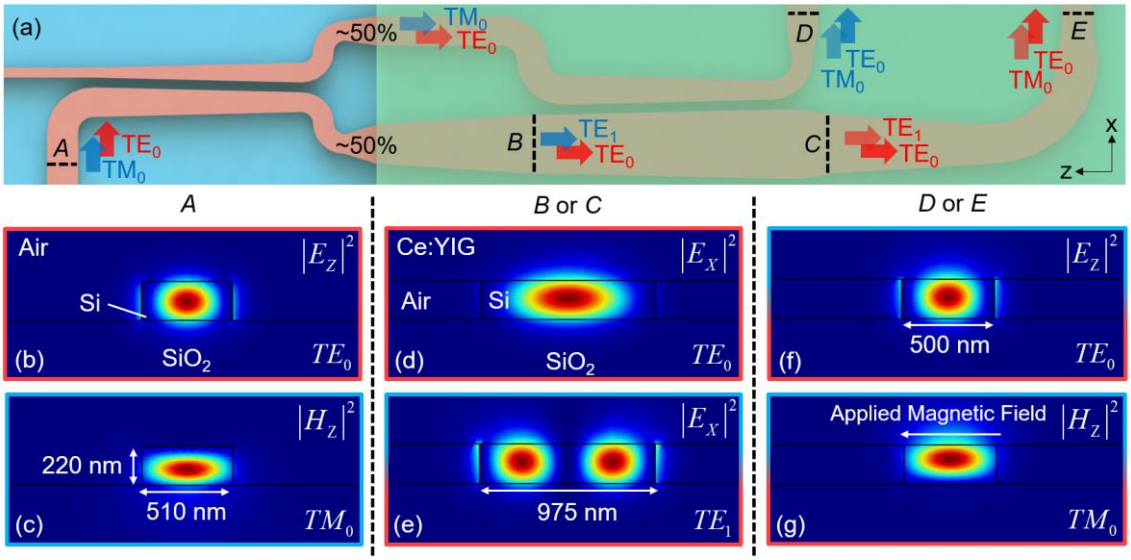


Fig.5-4 (a)The mode conversion process of TE- and TM-polarized input of the device. The mode field distributions at a specific location were shown: (b) $TE_0$ mode and (c) $TM_0$ mode of the input waveguide; (d) $TE_0$ mode and (e) $TE_1$ mode in the wider waveguide at both ends of the mode coupler; (f) $TE_0$ mode and (g) $TM_0$ mode in the nonreciprocal phase shifter.

When the $TM_0$ mode (as shown in Fig.5-4 (c)) was input, it was also converted to the $TM_{even}$ mode at the 3-dB coupler and evenly divided. After that, the $TM_0$ mode of the lower-arm waveguide was converted to the $TE_1$ mode by the $TE_1$&$TM_0$ converter,

and finally coupled and converted to the $TE_0$ mode in the upper-arm waveguide by the $TE_1$&$TE_0$ coupler and reunited with the $TM_0$ mode. Finally, entered the nonreciprocal phase shifter from *Position D*. Table.5-1 shows the mode conversion process of the PRC at the input side.

Table.5-1 Mode conversion processes of the input PRC

| Modes | TE-polarized input | TM-polarized input |
|---|---|---|
| $Mode_1$ | $TE_0 \rightarrow TE_1 \rightarrow TM_0$ | $TM_0$ |
| $Mode_2$ | $TE_0$ | $TM_0 \rightarrow TE_1 \rightarrow TE_0$ |

The two nonreciprocal phase shifter for each polarization of the input light had the same design. After the reverse mode conversion process, the phase-modulated modes interfered with the same polarization at the output 3-dB coupler. In-phase part energy excited the even mode and converted into the output mode; while out-of-phase part energy excited the odd mode and finally converted into the cladding mode for evanescent.

## 5.3 Simulation and parameter design

The materials parameter used in the simulation were $n_{Si} = 3.48$, $n_{SiO_2} = 1.444$, and $n_{Ce:YIG} = 2.2$. The FR of Ce:YIG was assumed as 4500 °/cm.

As the blue area shown in Fig.5-5 (a), for the $TE_1$&$TM_0$ converter, its structural parameters were consistent with that in Chapter 4 and would not be repeated here.

For the $TE_1$&$TE_0$ coupler, the widths of the two waveguides were defined as $W_1$ and $W_2$, respectively, with a gap of 150 nm. We first determined one end widths of two tapered waveguides of 975 nm and 510 nm, corresponding to the widths of the mode converter and single-mode MO waveguide. As the waveguide width varied, the $TE_0$ mode in the narrower waveguide and the $TE_1$ mode in the wider waveguide would have the same $n_{eff}$ somewhere to achieve mode coupling (as the green area shown in Fig.5-5 (a)). The width of the other end of the coupler was designed to be 1025 nm and 460 nm respectively to ensure that there was no energy coupling between the waveguides.

For the 3-dB coupler design, the width at one end of the coupler was fixed at

$W_1$=$W_2$=430 nm with a gap of 150 nm to support $TE_{even}$ and $TM_{even}$ modes. The $n_{eff}$ of the propagating mode in the coupler with different widths was simulated as shown in Fig.5-5 (b), and the $n_{eff}$ of the $TE_{even}$ mode ($mode_0$) and the $TE_{odd}$ mode ($mode_1$) were close around $W_1$=$W_2$, where was prone to crosstalk. So, the tapered waveguide was designed into two parts. The first part $W_1$/$W_2$ gradually tapered to 415 nm/445 nm, this part required a gentler tapered waveguide design to meet the adiabatic condition. In the second part, $W_1$/$W_2$ was tapered to 350 nm/510 nm, which further increased the width difference between the two waveguides. The 510-nm-wide waveguides are connected to the input/output port of the isolator.

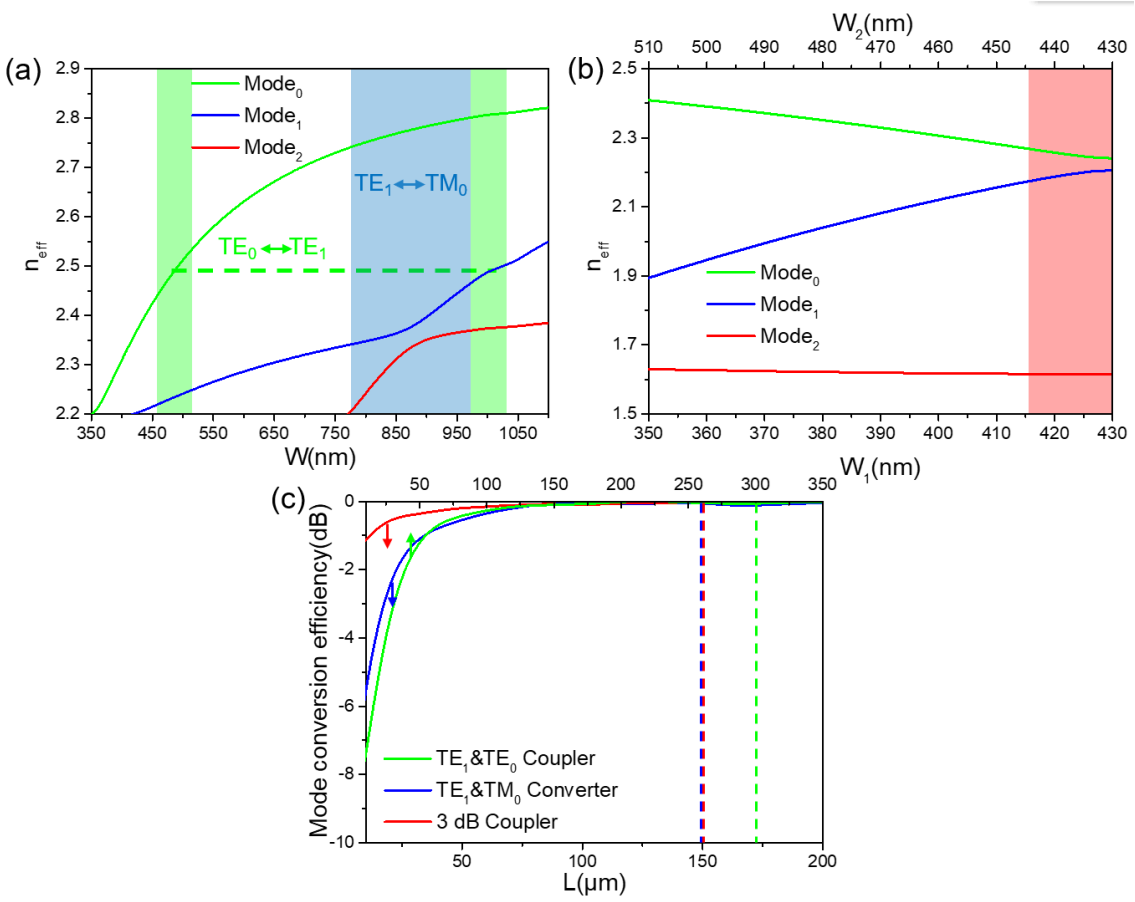


Fig.5-5 $n_{eff}$ in (a) a single MO waveguide and (b) an air-clad 3-dB coupler with different waveguide widths. (c) Mode conversion efficiency corresponds to different taper lengths.

The length of the mode coupler and mode converter was designed by simulating the mode conversion efficiency corresponding to different tapered lengths (as shown

in Fig.5-5 (c)). Under the requirement that the mode conversion efficiency was ~99%, The lengths of the $TE_1$&$TM_0$ converter, $TE_1$&$TE_0$ coupler, and the first part of the 3-dB coupler were designed to be 150 μm, 300 μm, and 150 μm, respectively. The length of the second part of the 3-dB coupler was designed to be 50 μm to achieve a negligible IL. The overall device structure parameters are shown in Table.5-2.

Table.5-2 Structural parameters

| Components | W or $W_1$/$W_2$(nm) | L(μm) |
|---|---|---|
| $TE_1$&$TE_0$ coupler | 510/975 → 460/1025 | 300 |
| $TE_1$&$TM_0$ converter | 775 → 975 | 150 |
| 3-dB coupler | 350/510 → 415/445 → 430/430 | 50/150 |

Then we will discuss the integration position of Ce:YIG chip. Ideally, the phase difference between $mode_1$ and $mode_2$ should be $2n\pi$ in forward transmission and $(2n-1)\pi$ in backward transmission, corresponding to the NRPS of $\pi$. In this case, the interference transmission efficiency of Eq.3-1 could be simplified as

$$\begin{aligned} T_{forward} &= \frac{\alpha_1 + \alpha_2 + 2\sqrt{\alpha_1\alpha_2}}{4} \\ T_{backward} &= \frac{\alpha_1 + \alpha_2 - 2\sqrt{\alpha_1\alpha_2}}{4} \end{aligned}, \tag{5-1}$$

where $\alpha_1$, $\alpha_2$ were the the transmission efficiency of $mode_1$ and $mode_2$. So for a lower IL, $\alpha_1$ and $\alpha_2$ should approach 1; and for a higher IR, $\alpha_1$ and $\alpha_2$ should be approximately equal. Therefore, to lower the MO loss, the Ce:YIG/SGGG chip ideally only covered the nonreciprocal phase shifter, but under such a design, $mode_1$ and $mode_2$ would be $TM_0$ and $TE_0$ modes at the edge of Ce:YIG, respectively. The junction loss of the two modes had a huge difference of 2.5 dB and 0.2 dB per edge, which would cause $T_{backward}$ to be non-zero and reduce IR. To balance the IL of $mode_1$ and $mode_2$, we designed an air-cladding 3-dB coupler, and light would enter the MO waveguide before the mode conversion to ensure that the ILs of the two modes were approximately the same.

Finally, the NRPS of the $TM_0$ mode in the nonreciprocal phase shifter was calculated to be 5.2 rad/mm, corresponding to a MO waveguide length of 600 μm. Considering the NRPS of bending waveguide and material performance errors, the final length of the nonreciprocal phase shifter was designed to be 550 μm.

In the preliminary experiments, we found that there was still intermode crosstalk. The problem from the mode coupling at the ends of the $TE_1$&$TE_0$ coupler as shown in Fig.5-6 (a). If we directly separated waveguides by a bending waveguide, unexpected mode crosstalk would be introduced. Therefore, we added a 50-μm-long gradient structure making the gap wider from 150 nm to 650 nm to suppress crosstalk. As shown in Fig.5-6 (b), such a design could completely avoid the crosstalk problem in the simulation.

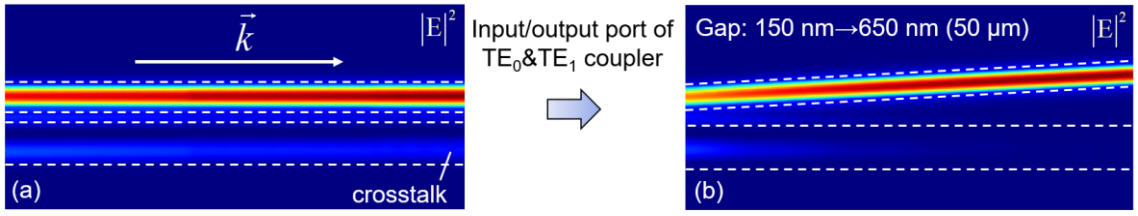


Fig.5-6 Mode energy distribution in the waveguides at the ends of the mode coupler (a) without and (b) with a tapered gap.

## 5.4 Experiment and device characterization

After the preparation process shown in Fig.5-7, we fabricated the designed device.

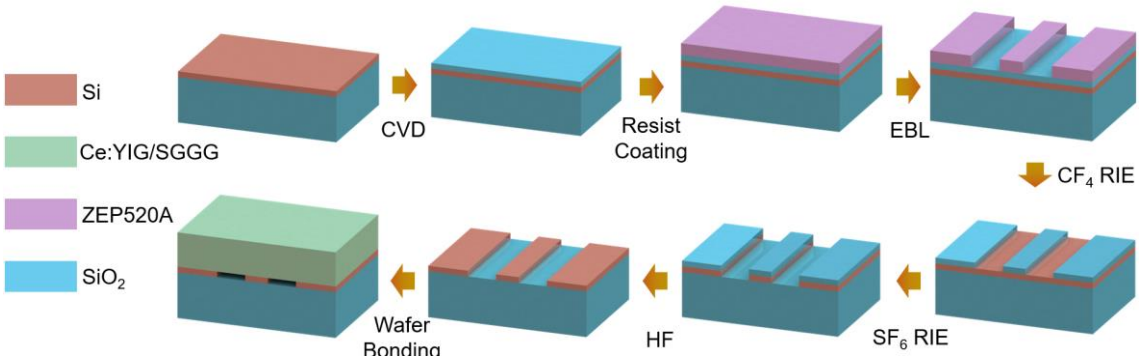


Fig.5-7 Processing flow.

The micrograph of the experimentally prepared device is shown in Fig.5-8 (a), the green square area was the bonded Ce:YIG/SGGG chip. The focal lengths of the MO-cladding and air-cladding areas were different to clearly show the device structure. The reference waveguide is shown in Fig. 5-8 (b), which contained only one S-bend waveguide without any additional loss mechanism.

The SEM photographs of the junction of the port of the 3-dB coupler and the edge of the Ce:YIG/SGGG chip is shown in Figs.5-8 (c) and (d). The actual waveguide width at the 3-dB coupler port was ~357 nm/516 nm, which matched the design value of 350 nm/510 nm, proving that the fabrication error was within the acceptable range. And the junction at the edge of the Ce:YIG was almost flat, so no additional junction losses would be introduced from the chip edge irregularities.

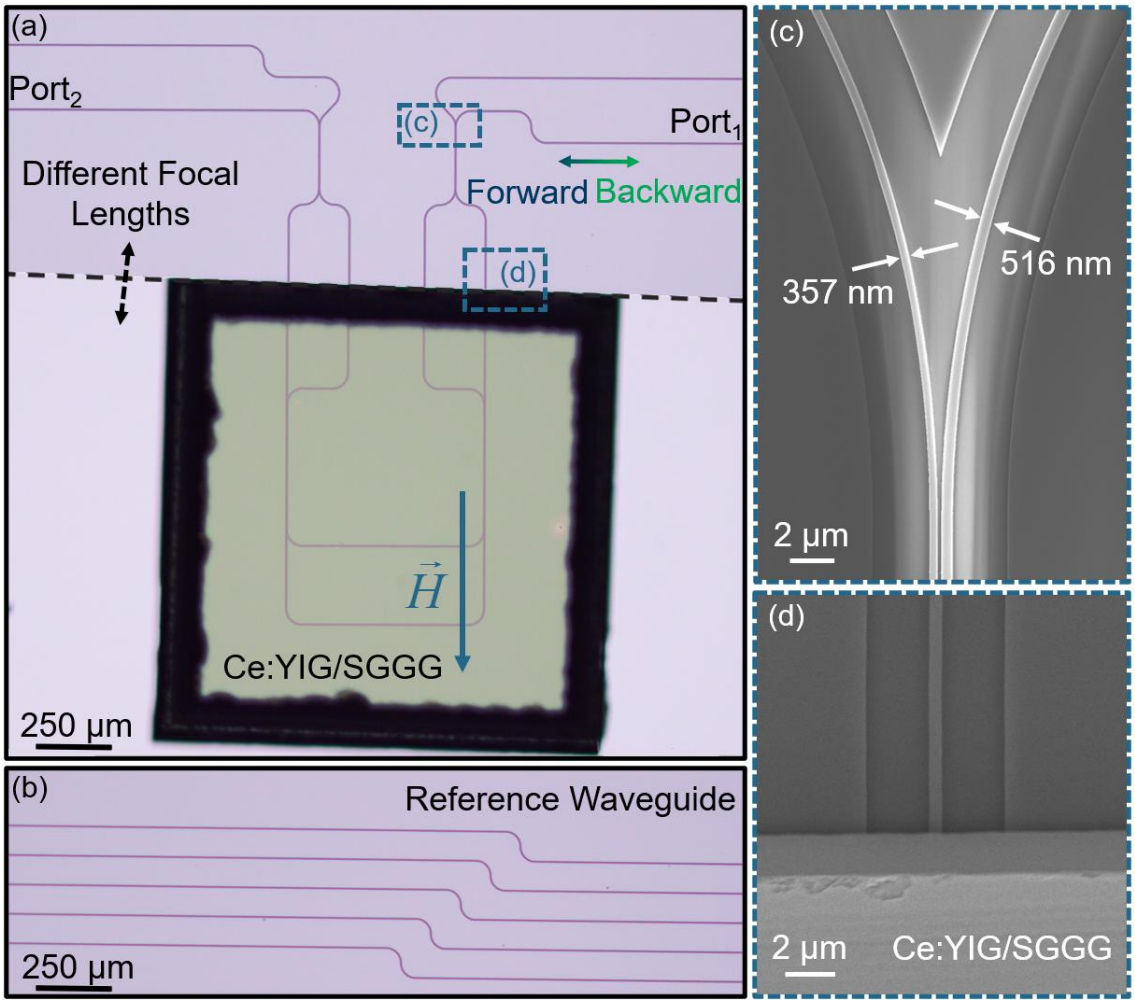


Fig.5-8 Micrographs of (a) the devices and (b) the reference waveguides. SEM photos of (c) the port of 3-dB coupler and (d) the junction between the MO waveguide and the non-MO waveguide.

After magnetizing the MO material by applying an external magnetic, the forward and backward transmission spectra under TE- and TM-polarized inputs were measured as shown in Figs. 5-9 (a) and (b). Under TE-polarized input, the device

exhibited a 20-dB IR, a 4.6-dB IL, and a 10-dB isolation bandwidth of 0.35 nm at a wavelength of 1577.1 nm; and a 12-dB IR, an 8.2-dB IL and a 10-dB isolation bandwidth of 0.45 nm at a wavelength of 1576.3 nm under TM-polarized input.

The operating wavelength inconsistency under TE- and TM- polarized input was difficult to avoid only by device structure design because the center wavelength was very sensitive to fabrication errors. Generally, optical isolators required further calibration to match the wavelength of the light source in the optical system. A general solution was to arrange metal electrodes around the waveguide to control the operation wavelength by the thermo-optic effect. In the proposed configuration, the operation wavelengths could be independently controlled by employing electrodes around two nonreciprocal phase shifters under TE- and TM- polarized inputs to meet application requirements [5-9].

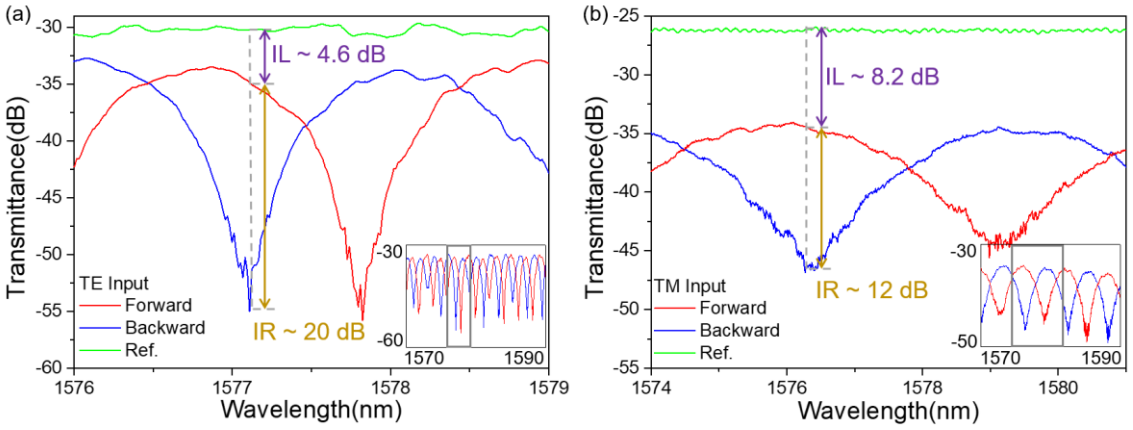


Fig.5-9 Transmission spectra of the isolator in forward and backward transmission for (a) TE- and (b) TM-polarized input. And transmission spectrum of the reference waveguide.

## 5.5 Discussion

The theoretical free spectral range (FSR) of the device could be calculated by the intermode dispersion between mode$_1$ and mode$_2$. We first simulated the dispersion of the modes in a single MO waveguide and TE$_1$&TE$_0$ couplers as shown in Figs. 5-10 (a) and (b). Combined with the device length, the dispersion of mode$_1$ and mode$_2$ under TE-polarized input were -27.5 rad/nm and -24.3 rad/nm, respectively; and were -19.3 rad/nm and -20.4 rad/nm under TM polarized input. The calculated FSRs were

2.0 nm and 5.6 nm, respectively, which were in line with the measured FSRs of ~2 nm and ~6 nm.

The theoretical MO loss could be estimated by the confinement factor as in the previous chapters. In this work, we optimized the plasma treatment process in wafer bonding: from the $N_2$ plasma treatment for 20 s to the $O_2$ plasma treatment for 30 s. While maintaining the success rate of bonding, the damage to the surface of Ce:YIG chips and the topwall of the waveguide could be reduced. Therefore, the experimentally calculated $\alpha_{Ce:YIG}$ was 40 dB/cm, and $\alpha_{Si}$ was 3 dB/cm. By simulating the confinement factors in Ce:YIG and Si layers under different waveguide widths of a single MO waveguide and $TE_1$&$TE_0$ couplers, the propagation loss of modes was calculated as shown in Figs.5-11 (a) and (b). Combining with device length, the MO loss of $mode_1$ and $mode_2$ under TE-polarized input was 4.6 dB and 2.3 dB; 7.3 dB and 3 dB under TM-polarized input, respectively. The total MO loss was 3.4 dB and 4.9 dB for TE- and TM-polarized input, respectively.

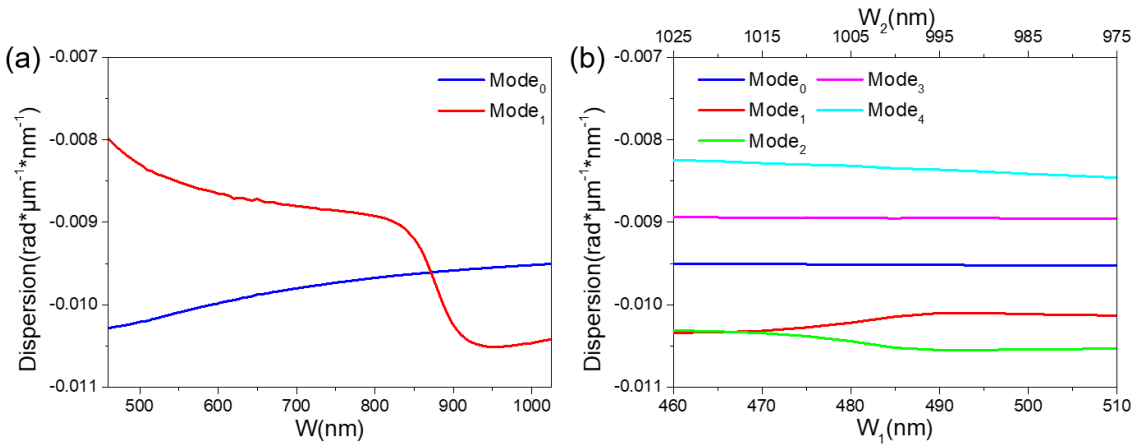


Fig.5-10 Mode dispersions in (a) a single MO waveguide and (b) the coupler varies with waveguide width.

Another source of IL was the junction loss at the edge of Ce:YIG. Due to the limitation of wafer bonding precision, we designed a straight waveguide with a width of 510 nm and a length of 300 μm as a buffer area, as long as the Ce:YIG edge was in this area the device could work as the design expected. The corresponding junction losses for the $TE_0$ and $TM_0$ modes were 0.2 dB and 2.5 dB per edge respectively under the waveguide size in the buffer area.

Adding the extra Si waveguide propagation loss of 0.2 dB and 0.1 dB under TE-

and TM-polarized input respectively due to the difference in length of the air-clad silicon waveguide between the device and the reference waveguide, the overall loss budget of the device is shown in Table.5-3. By Eq.5-1, the theoretical IR and IL of the device were 17.3 dB and 4.0 dB under TE-polarized input; and 12.3 dB and 10.0 dB under TM-polarized input, respectively, which were in line with the measured result. Performance error mainly came from that in the simulation we assume that the junction was at the center of the buffer area, however, the position was always biased in the fabrication, resulting in performance errors.

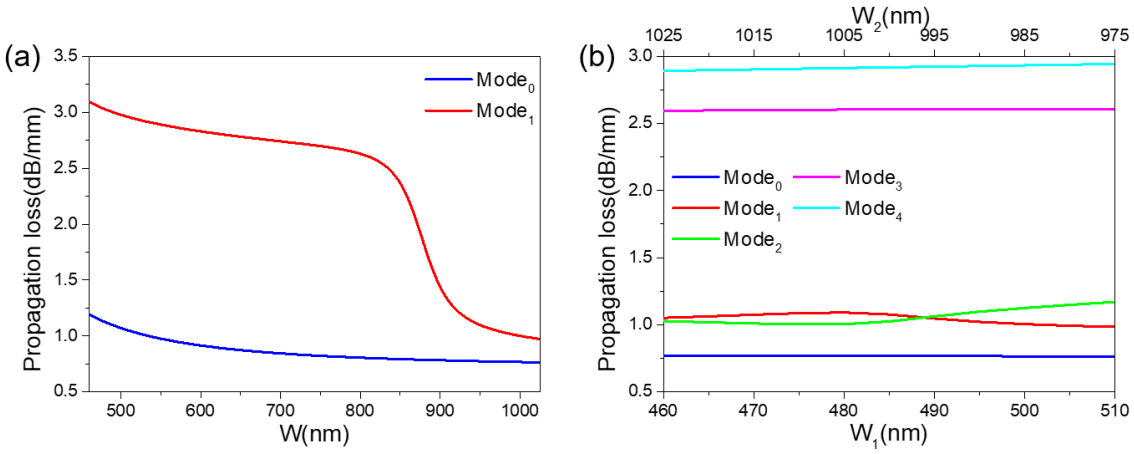


Fig.5-11 Mode propagation losses in (a) a single MO waveguide and (b) the coupler varies with waveguide width.

Table.5-3 Loss budget

| Origin of loss | Value (dB) | |
|---|---|---|
| | TE | TM |
| MO waveguide | 3.4 | 4.9 |
| Additional silicon waveguides | 0.2 | 0.1 |
| Ce:YIG edge junction | 0.2×2 | 2.5×2 |
| Total | 4.0 | 10.0 |

The theoretical IR was worse for TM-polarized input because the intermode loss imbalance was mainly caused by the significant difference in MO loss of TE and TM modes. Under TM-polarized input, such a loss difference existed before the $TE_1$&$TE_0$ coupler; while under TE-polarized input, such a loss difference did not exist until the nonreciprocal phase shifter.

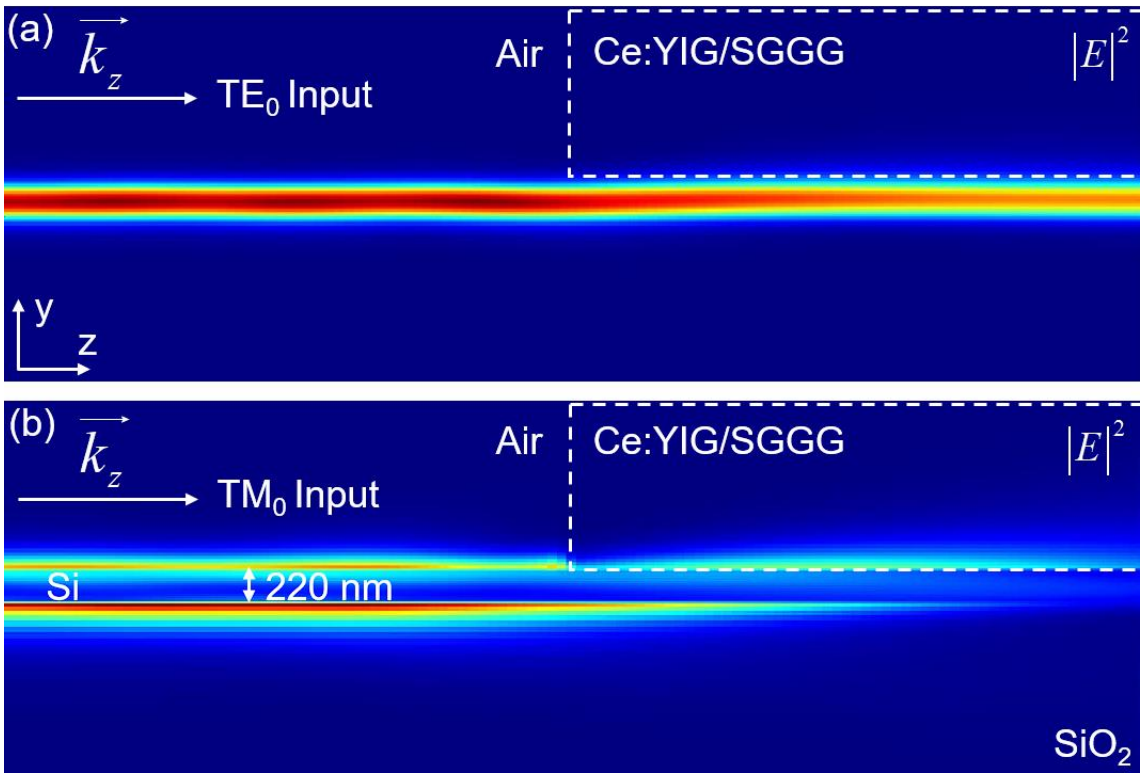


Fig.5-12 The simulated field distribution at the junction structure at the edge of Ce:YIG chip with (a) TE- and (b) TM-polarized input.

Then we simulated and analyzed the reflection loss at the edge of Ce:YIG. The field distribution under $TE_0$ mode input is shown in Fig.5-12 (a), the junction loss was 0.2 dB and the reflection was only -42 dB, so the negative impact on the isolation operation could be ignored; The field distribution when the $TM_0$ mode was input is shown in Fig.5-12(b). The junction loss was 2.5 dB, and the reflection was -32 dB, so the energy was also mainly evanescent in the form of cladding mode.

## 5.6 Summary

In this chapter, we successfully designed and experimentally demonstrated a polarization-independent silicon-based integrated MO isolator by half-mode conversion. The isolator finally exhibited 20-dB IR and 4.6-dB IL under TE-polarized input; 12-dB IR and 8.2-dB IL under TM-polarized input.

The performance of the proposed isolator is expected to be further improved. If we can further improve the bonding precision, such as using μ-transfer printing technology, and making the MO material only covers the nonreciprocal phase shifter,

the MO loss of the device will be reduced (as shown in Fig.5-13 (a)). However, due to the difference in junction loss between $TE_0$ and $TM_0$ modes, IR will be restricted by unbalanced intermode losses. But if the junction loss corresponding to $TE_0$ and $TM_0$ modes can be reduced to a negligible level, such as by designing gradient junction structure or tapered MO material integrated window structures, and only the MO loss of a 600-μm long nonreciprocal phase shifter is considered, the ideal IL of 1.2 dB and IR of 24 dB under both TE- and TM-polarized input will be achieved (as shown in Fig.5-13 (b)). In general, the device was a milestone as the first integrated polarization-independent isolator [10].

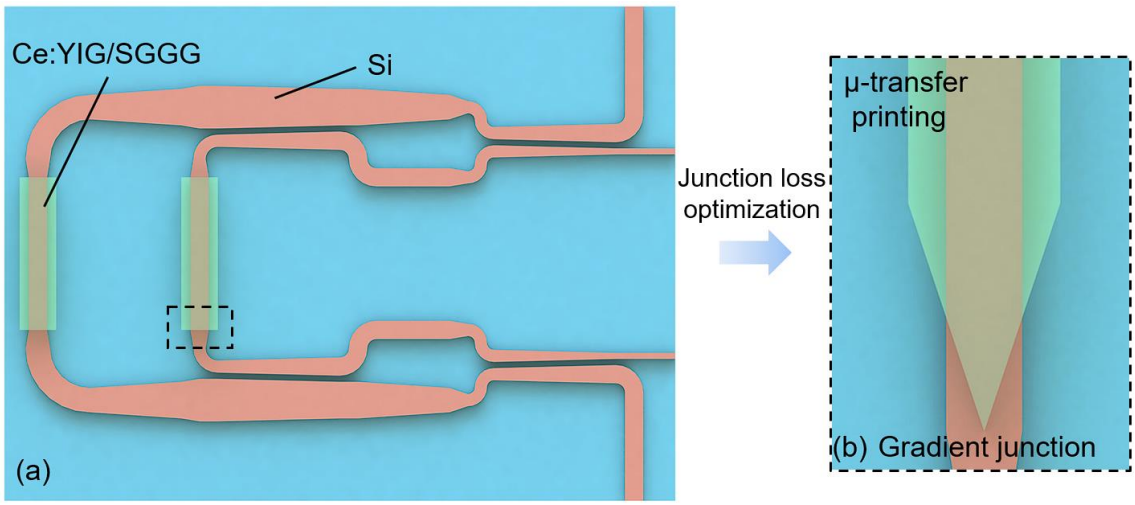


Fig.5-13 (a) Schematic diagram of MO loss optimization and (b) junction loss optimization.

## References


1. Xie A., Zhou L., Chen J. and Li X., "Efficient silicon polarization rotator based on mode-hybridization in a double-stair waveguide." *Optics Express* 23.4 (2015): 3960-3970. DOI: 10.1364/OE.23.003960
2. Leung D.M.H., Rahman B.M.A. and Grattan K.T.V., "Numerical analysis of asymmetric silicon nanowire waveguide as compact polarization rotator." *IEEE Photonics Journal* 3.3 (2011): 381-389. DOI: 10.1109/JPHOT.2011.2140098
3. Kim S. and Qi M., "Polarization rotation and coupling between silicon waveguide and hybrid plasmonic waveguide." *Optics Express* 23.8 (2015): 9968-9978. DOI: 10.1364/OE.23.009968
4. Wang Y., Xu L., Yun H., Ma M., Kumar A., El-Fiky E., Li R., Abadíacalvo N., Chrostowski L., Jaeger N.A. and Plant D.V., "Polarization-independent mode-evolution-based coupler for the silicon-on-insulator platform." *IEEE Photonics Journal* 10.3 (2018): 1-10. DOI: 10.1109/JPHOT.2018.2835767
5. Liang Z., Liu S. and Shoji Y., "Improvement of extinction in optically-controlled silicon thermo-optic switch based on micro-ring resonator with distinct probe signal." *Japanese Journal of Applied Physics* 62.3 (2023): 032001. DOI: 10.35848/1347-4065/acbc5d
6. Densmore A., Janz S., Ma R., Schmid J.H., Xu D.X., Delâge A., Lapointe J., Vachon M. and Cheben P., "Compact and low power thermo-optic switch using folded silicon waveguides." *Optics Express* 17.13 (2009): 10457-10465. DOI: 10.1364/OE.17.010457
7. Fang Q., Song J.F., Liow T.Y., Cai H., Yu M.B., Lo G.Q. and Kwong D.L., "Ultralow power silicon photonics thermo-optic switch with suspended phase arms." *IEEE Photonics Technology Letters* 23.8 (2011): 525-527. DOI: 10.1109/LPT.2011.2114336
8. Chen S., Shi Y., He S. and Dai D., "Low-loss and broadband 2× 2 silicon thermo-optic Mach–Zehnder switch with bent directional couplers." *Optics Letters* 41.4 (2016): 836-839. DOI: 10.1364/OL.41.000836
9. Huang D., Pintus P., Shoji Y., Morton P., Mizumoto T. and Bowers J.E., "Integrated broadband Ce: YIG/Si Mach–Zehnder optical isolators with over 100 nm tuning range." *Optics Letters* 42.23 (2017): 4901-4904. DOI: 10.1364/OL.42.004901
10. Liu S., Minemura D. and Shoji Y., "Silicon-based integrated polarization-independent magneto-optical isolator." *Optica* 10.3 (2023): 373-378. DOI: 10.1364/OPTICA.483017

# Chapter VI

# Conclusion and perspective

## 6.1 Conclusion

MO nonreciprocal devices are important components in PICs, and their high-performance on-chip integration is indispensable for realizing complex function chips. Starting from device design, this dissertation proposed three novel integrated MO nonreciprocal device designs based on the temperature-compatible integration of MO materials by wafer bonding technology. Each design exhibited unique performance advantages for different applications.

For existing problems such as: integrated devices, especially TE-mode devices, have high IL; MRR devices fabricated by wafer bonding cannot work under a unidirectional magnetic field; polarization-independent optical isolators integrated on silicon have not been proved experimentally. We sequentially overcame the above problems with exhaustive and novel device designs. Due to the limitation of the MO waveguide structure under the wafer bonding process, the isolation operation of the TE mode needed to be realized by employing the NRPS of the TM mode. Therefore, the key to achieving low IL was how to achieve efficient mode conversion. So, the mode converters and mode couplers in this dissertation were all designed based on mode evolution. While achieving high mode conversion efficiency, the components also had a wide operating bandwidth and high manufacturing tolerance. The content of each chapter and the uniqueness of each device as follows:

In Chapter 1, we summarized the application requirements, development status, and challenges of integrated MO nonreciprocal devices. The research motivations were determined to improve the performance of integrated TE-mode devices, especially to optimize the IL; by structural design to ensure that the device could work in a unidirectional magnetic field to simplify the magnetic field integration process;

after the performance of the TE mode device was optimized, the design and experimental preparation of a polarization-independent MO isolator would be carried out.

In Chapter 2, starting from the determination of the permittivity tensor of MO materials, we discussed in detail the method of calculating NRPS of MO waveguides based on the perturbation theory and discussed the NRPS support of different waveguide structures for different polarization modes. Then the relationship between the FoM of the MO waveguide and its structure was discussed based on the confinement factor calculation. Finally, based on the coupled-mode theory, the mode evolution and mode coupling were compared, and the characteristics of wide operating bandwidth and high manufacturing tolerance of mode evolution devices were discussed.

Chapters 3 and 4 were for the optimization of IL and structure of broadband MMI-type and narrowband MRR-type TE-mode devices, respectively.

Broadband devices were mostly used in front of multi-wavelength light sources or in wavelength division multiplexing systems. The proposed configuration avoided the abrupt structure by the design of the mode conversion in the parallel waveguides; and utilized the hybrid mode to accumulate NRPS during the polarization rotation process to avoid additional series PRs. Finally achieved an IL of 5 dB. Additionally, the proposed device has a quasi-one-dimensional structure, which has a huge advantage in the on-chip footprint.

Narrowband devices were not suitable for multi-wavelength light sources and modulated optical systems but for single-wavelength light sources. Because MRR devices had the characteristics of high IR and low IL, they were still one of the important research directions. The configuration we proposed avoided the additional loss caused by series PRs by combining the mode converter with the coupling area of the MRR; the asymmetric microring structure realized that only one side of the microring supports NRPS of $TM_0$ mode, so the device could work under a unidirectional magnetic field. The device finally exhibited an IL of 4.3 dB, and an IR of >20 dB which initially met the application requirements.

Inspired by the design of the above two devices, we propose a polarization-independent MO isolator based on half-mode conversion in Chapter 5. The device realized half-mode conversion under both TE- and TM-polarized input by

polarization-independent 3-dB couplers and $TE_1$-mode-intermediated PRCs. And the polarization-independent isolation properties were demonstrated in the experiment successfully. The device was of great significance as the first silicon-based integrated polarization-independent isolator. The proposed device could be used in polarization multiplexing systems or long-distance inter-chip communication systems to simultaneously block TE- and TM-polarized noise signals, greatly increasing the device integration density.

For performance comparison, we summarized device performance in a form consistent with Table.1-1 as Table.6-1.

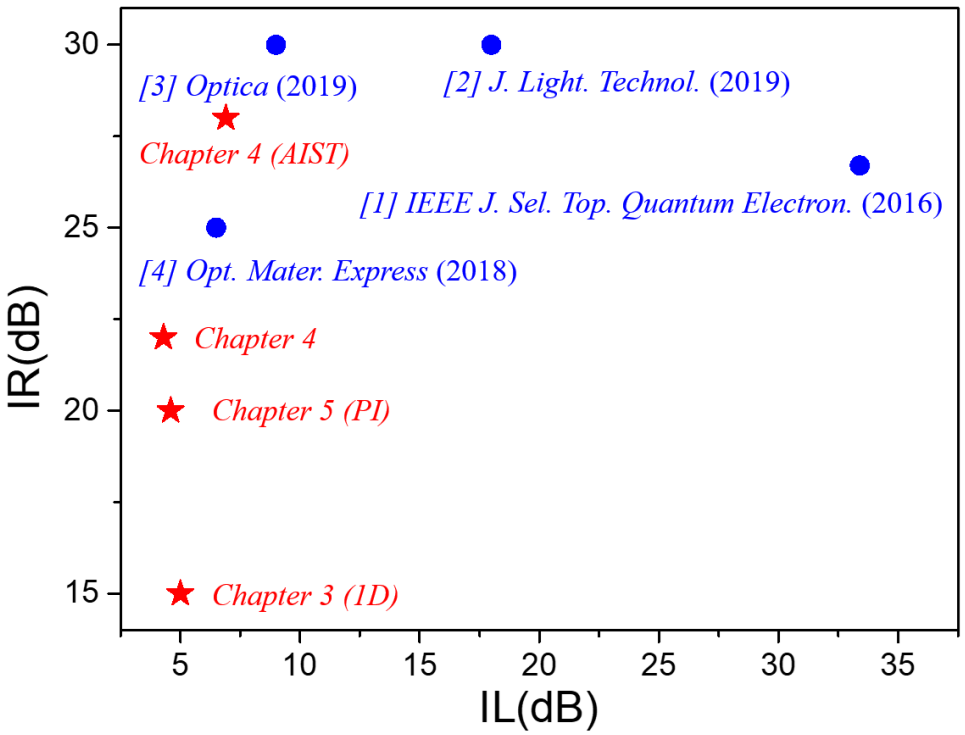


Fig.6-1 Performance comparison of TE mode MO isolators [1-4].

For the performance comparison of TE-mode isolators, we draw their IL and IR in Fig. 6-1. In terms of IL, the proposed configurations had a certain improvement compared with other works. In terms of IR, although MMI-type devices were slightly lower than MZI-type devices and MRR-type devices due to the unbalanced intermode loss, they still had novel characteristics such as quasi-one-dimensional structures or polarization independence operation, so they had unique applications.

Table.6-1 Summary of the device performance

| Type | IL (potentially improved) (dB) | IR (dB) | Polarization | 10-dB IR bandwidth (nm) | Integration |
|---|---|---|---|---|---|
| MRR | 4.3 (1.4) | 22 | TE | 0.05 | Direct Bonding |
| | 6.9 (1.4) | 28 | TE | 0.06 | Direct Bonding (AIST) |
| MMI | 5 (3.56) | 15 | TE | 2 | Direct Bonding |
| | 4.6 (1.2) | 20 | TE | 0.35 | Direct Bonding |
| | 8.2 (1.2) | 12 | TM | 0.46 | Direct Bonding |

In addition to IL, the optimization of IR and device size are also important directions for future research.

The IR for MMI-type devices depends on the balance of intermode losses. As shown in Fig.6-2 (a), to achieve an IR of 30 dB, the mode amplitude difference needs to be less than 6%; The IR of the MRR-type devices depends on the critical coupling condition. Ideally, the IR is infinite when $|t| = \alpha$; however, due to fabrication errors, the error between $|t|$ and $\alpha$ needs to be less than 4% in the actual device to achieve a 30-dB IR (as shown in Fig.6-2 (b)). Therefore, balancing the intermode losses and improving the fabrication accuracy are the key points of optimizing IR.

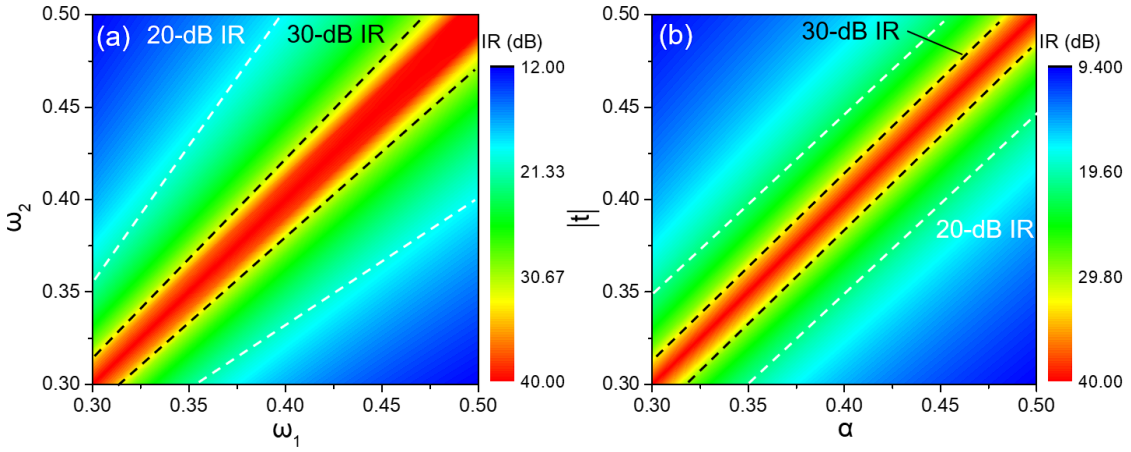


Fig.6-2 (a) The IR of MMI-type devices varies with the amplitude of the two modes for interference. (b) The relationship between IR and $|t|$ and $\alpha$ of MRR-type devices.

The optimization of the on-chip footprint can be done from two aspects. The first is to optimize the size of the bonded MO material. To facilitate the experimental operation, the size of the currently used Ce:YIG chip is 1.5 mm×1.5 mm. In practical applications, transfer printing or monolithic integration technology can be used to achieve micron-scale MO materials size; The second is to optimize the device length. Although the device has discarded the traditional PRs components and optimized the overall size, the device length is still relatively long due to the adiabatic condition of the mode evolution. If there is a requirement for the device length in practical applications, S-shaped waveguide segments can be used to compress the device size.

## 6.2 Perspective

For the development of future TE-mode nonreciprocal devices, based on my knowledge, the combination of subwavelength structures with MO materials will design interesting devices [5-8].

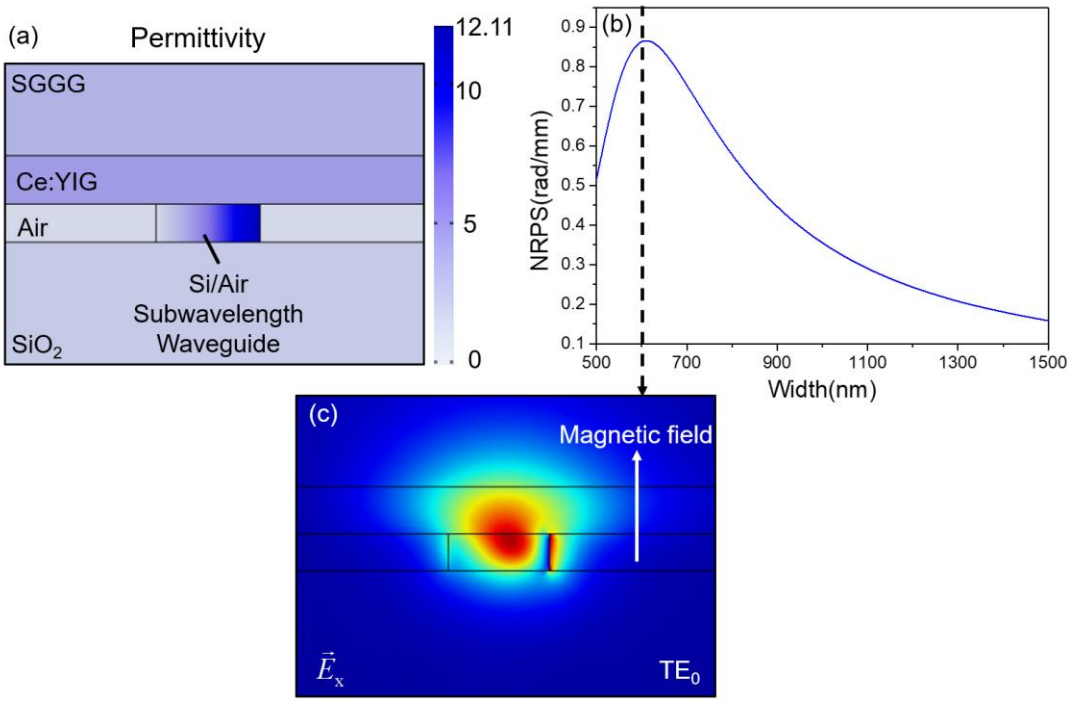


Fig.6-3 Subwavelength waveguides supporting TE-mode NRPS. (a) Waveguide structure and permittivity distribution. (b) NRPS varies with waveguide width. (c) The mode field distribution of the $TE_0$ mode with a width of 600 nm.

For subwavelength waveguides, the effective refractive index of the waveguide can be flexibly tuned by the duty cycle [9,10]. Therefore, the asymmetry of in-plane material distribution required by TE mode NRPS can be realized by subwavelength waveguides with gradient refractive index, as shown in Fig.6-3 (a). Such a refractive index of the waveguide is realized by periodically arranged subwavelength tapered elements. We assume that the structure is prepared on a standard SOI substrate. By simulating the $TE_0$ mode NRPS at different subwavelength waveguide widths as shown in Fig.6-3 (b), we can find that such a waveguide structure can support NRPS of $TE_0$ mode and the maximum NRPS of 0.89 rad/mm is achieved when the width is ~600 nm, and the corresponding mode field distribution of $TE_0$ mode is shown in Fig.6-3 (c).

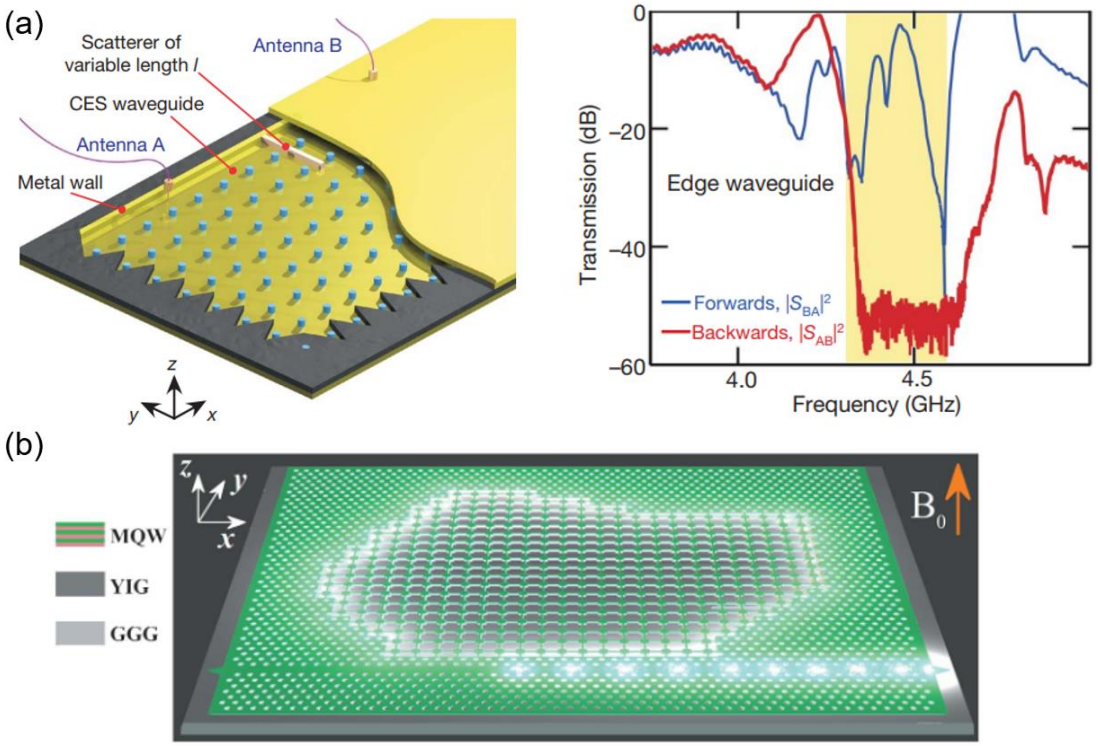


Fig.6-3 Recent achievements in MO PhC. (a) Unidirectional transmission at microwave frequency [12]. (b) Nonreciprocal laser cavities [13].

Another idea is to realize topological unidirectional waveguides by MO photonic crystals (MOPhC). The unique permittivity tensor properties of MO materials will break the time-reversal symmetry of the MOPhC and construct topologically nontrivial boundary states, resulting in only single edge state supported in the bandgap,

light can only propagate in one direction without reflection. This phenomenon has already been proved in the microwave frequency [11,12], but there are few related works in the optical frequency, and only a nonreciprocal topological cavity laser has been reported so far [13]. We believe that topological nonreciprocal devices will play an important role in PICs based on the perfection of MO materials and related theories.

## References


1. Shoji Y., Fujie A. and Mizumoto T., "Silicon waveguide optical isolator operating for TE mode input light." *IEEE Journal of Selected Topics in Quantum Electronics* 22.6 (2016): 264-270. DOI: 10.1109/JSTQE.2016.2574678
2. Pintus P., Huang D., Morton P.A., Shoji Y., Mizumoto T. and Bowers J.E., "Broadband TE optical isolators and circulators in silicon photonics through Ce: YIG bonding." *Journal of Lightwave Technology* 37.5 (2019): 1463-1473. DOI: 10.1109/JLT.2019.2896650
3. Zhang Y., Du Q., Wang C., Fakhrul T., Liu S., Deng L., Huang D., Pintus P., Bowers J.E., Ross C.A. Hu J. and Bi L., "Monolithic integration of broadband optical isolators for polarization-diverse silicon photonics." *Optica* 6.4 (2019): 473-478. DOI: 10.1364/OPTICA.6.000473
4. Huang D., Pintus P. and Bowers J.E., "Towards heterogeneous integration of optical isolators and circulators with lasers on silicon." *Optical Materials Express* 8.9 (2018): 2471-2483. DOI: 10.1364/OME.8.002471
5. Yu Z., Veronis G., Wang Z. and Fan S., "One-way electromagnetic waveguide formed at the interface between a plasmonic metal under a static magnetic field and a photonic crystal." *Physical Review Letters* 100.2 (2008): 023902. DOI: 10.1103/PhysRevLett.100.023902
6. Skirlo S.A., Lu L. and Soljačić M., "Multimode one-way waveguides of large Chern numbers." *Physical Review Letters* 113.11 (2014): 113904. DOI: 10.1103/PhysRevLett.113.113904
7. Li C., Zhang M., Xu H., Tan Y., Shi Y. and Dai D., "Subwavelength silicon photonics for on-chip mode-manipulation." *PhotoniX* 2.1 (2021): 1-35. DOI: 10.1186/s43074-021-00032-2
8. Guan X., Chen P., Chen S., Xu P., Shi Y. and Dai D., "Low-loss ultracompact transverse-magnetic-pass polarizer with a silicon subwavelength grating waveguide." *Optics Letters* 39.15 (2014): 4514-4517. DOI: 10.1364/OL.39.004514
9. Xu H., Dai D. and Shi Y., "Ultra-broadband and ultra-compact on-chip silicon polarization beam splitter by using hetero-anisotropic metamaterials." *Laser & Photonics Reviews* 13.4 (2019): 1800349. DOI: 10.1002/lpor.201800349
10. Wu H., Li C., Song L., Tsang H.K., Bowers J.E. and Dai D., "Ultra-sharp multimode waveguide bends with subwavelength gratings." *Laser & Photonics Reviews* 13.2 (2019): 1800119. DOI: 10.1002/lpor.201800119
11. Skirlo S.A., Lu L., Igarashi Y., Yan Q., Joannopoulos J. and Soljačić M., "Experimental observation of large Chern numbers in photonic crystals." *Physical Review Letters* 115.25 (2015): 253901. DOI: 10.1103/PhysRevLett.115.253901
12. Wang Z., Chong Y., Joannopoulos J.D. and Soljačić M., "Observation of unidirectional backscattering-immune topological electromagnetic states." *Nature* 461.7265 (2009): 772-775. DOI: 10.1038/nature08293

13. Bahari B., Ndao, A. Vallini, F. El Amili A., Fainman Y. and Kanté B., "Nonreciprocal lasing in topological cavities of arbitrary geometries." *Science* 358.6363 (2017): 636-640. DOI: 10.1126/science.aao4551

# Appendix

## A.1 Preparation condition

### (1) $SiO_2$ deposition

The SOI chip is deposited a 200-nm-thick $SiO_2$ as a hard mask for RIE by P-CVD. The deposition condition is as follows:

Table.A1 P-CVD condition

| Parameters | Value |
|---|---|
| TEOS flow | 3 sccm |
| $O_2$ flow | 300 sccm |
| Temperature | 280 ℃ |
| Pressure | 30 Pa |
| RF power | 70 W |
| Time | ~5 min |

### (2) Patterning

Clean the 2 mm×2 mm SOI chips as Table.A2.

Table.A2 Chip clean

| | | |
|---|---|---|
| Acetone | 80 ℃ | 5 min |
| Ultrasonic cleaning | 100 kHz | 5 min |
| IPA | room temperature | 1 min |

Then coating 300-nm-thick ZEP-520A photoresist and bake at high temperature to cure the resist film as Table.A3.

Table.A3 Resist coating and baking

| | | |
|---|---|---|
| Spin-coating | 300 rpm | 3 s |
| | 6000 rpm | 120 s |
| | slope | 3 s |
| Baking | 180 ℃ | 15 min |

Afterward, the EB lithograph process is performed as follows:

Table.A4 EBL condition

| Parameters | Value |
|---|---|
| Accelerating voltage | 50 kV |
| Beam current | 100 pA |
| Exposure dose | 130 μC/cm$^2$ |

Finally, the graphics are completed by the development process at room temperature shown in the table below.

Table.A5 Development condition

| | |
|---|---|
| ZED-N50 | 60 s |
| IPA | 20 s |

**(3) Etching**

The pattern on the photoresist layer will be transferred to the $SiO_2$ and Si layer by a two-step RIE process.

Firstly, $SiO_2$ is etched, and the condition parameters are as follows:

Table.A6 $SiO_2$ RIE

| Parameters | Value |
|---|---|
| Gas | $CF_4$ |
| Flow | 20 sccm |
| Pressure | ~3×10$^{-3}$ Torr |
| RF power | 10 W |
| Time | 24 min |

Afterward, the surface of the sample is cleaned with $O_2$ plasma to remove the

photoresist layer as

Table.A7 $O_2$ cleaning

| Parameters | Value |
|---|---|
| Gas | $O_2$ |
| Flow | 20 sccm |
| Pressure | $5\times10^{-2}$ Torr |
| RF power | 20 W |
| Time | 3 min |

Finally, employ $SiO_2$ as a mask to etch the Si layer, the conditions are as follows:

Table.A8 Si RIE

| Parameters | Value |
|---|---|
| Gas | $SF_6$ |
| Flow | 3.5 sccm |
| Pressure | $2\times10^{-3}$ Torr |
| RF power | 20 W |
| Time | 5 min |

**(4) Wafer bonding**

First, clean the SOI chip and Ce:YIG/SGGG chips and holder for arranging Ce:YIG/SGGG chips as follows:

Table.A9 Ce:YIG/SGGG chips and holder cleaning

| | | | |
|---|---|---|---|
| Cleaning(Three times) | Acetone | 80 ℃ | 5 min |
| | Ultrasonic cleaning | 100kHz | 5 min |

Table.A10 SOI cleaning

| | | | |
|---|---|---|---|
| Resist removal | Acetone | 80 ℃ | 5 min |
| | ZDMAC | 80 ℃ | 5 min |
| | IPA | 80 ℃ | 5 min |
| $SiO_2$ removal | HF(1:19) | Room temperature | ~2 min |
| | Pure water | | 15 s (twice) |
| Si surface cleaning | Acetone | 80 ℃ | 5 min |
| | IPA | 80 ℃ | 5 min |
| | HF(1:19) | Room temperature | 10 s |
| | Pure water | Room temperature | 10 s (twice) |

After that, the bonding surface is activated by plasma treatment in the vacuum chamber of the bonding machine. The process has been optimized in the work in Chapter 5. The conditions before and after optimization are as follows:

Table.A11 Plasma treatment condition

| Parameters | Value | |
|---|---|---|
| Gas | $N_2$ (Previously) | $O_2$ (Optimized) |
| Flow | 103 sccm | 103 sccm |
| Pressure | 120 Pa | 120 Pa |
| RF power | 500 W | 500 W |
| Time | 20 s | 30 s |

Then, high-temperature pressurization bonding process conditions are as follows:

Table.A12 Wafer bonding

| | | | |
|---|---|---|---|
| Bonding | Pressurize | 10 MPa | 2 hours |
| | Temperature | 75 ℃ → 200 ℃ | 30 min |
| | | 200 ℃ | 60 min |
| | | 200 ℃ → 75 ℃ | 30 min |
| Cool down | | 75 ℃ → Room temperature | > 4 hours |

## A.2 Simulation parameters and tools

### (1) Material parameters

The material parameters used in the simulations at a wavelength of 1550 nm are as follows:

Table.A13 Material parameters

| Parameters | Value |
|---|---|
| $n_{Si}$ | 3.48 |
| $n_{SiO_2}$ | 1.444 |
| $n_{Ce:YIG}$ | 2.2 |
| $n_{SGGG}$ | 1.93 |
| FR of Ce:YIG | -4500 deg/cm |

When the simulation is in a wide range of wavelengths, we also need to consider material dispersion as shown in Fig.A1.

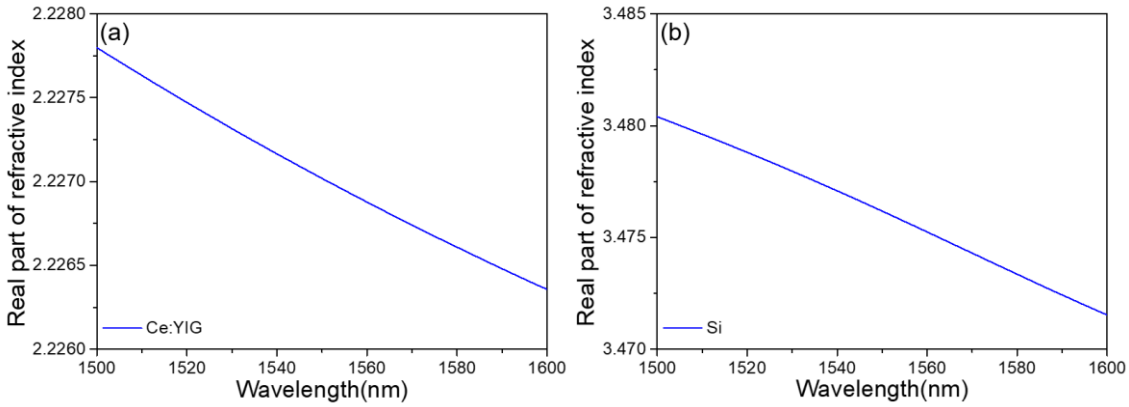


Fig.A1 Real part dispersion of refractive index of (a) Ce:YIG and (b) Si.

### (2) $n_{eff}$, NRPS, and confinement factor - COMSOL FEM

For the simulation of $n_{eff}$, NRPS, and confinement factor, we use the finite element method (FEM) of COMSOL for calculation. Its advantages are: triangular mesh can be divided, and $n_{eff}$ calculation accuracy is high; off-diagonal elements of material permittivity tensor can be directly defined, which is convenient for MO material setting; the sensitivity to the imaginary part of the refractive index is high, and an

accurate confinement factor can still be obtained when an extremely small imaginary part is assumed.

### (3) Mode field distribution, overlap, and TE ratio - Lumerical FDE

We choose the finite-difference eigenmode (FDE) module in Lumerical Mode Solution to calculate the mode field distribution. While solving the mode field, the group refractive index, TE ratio, and other information of the eigenmodes can also be obtained. At the same time, the solver is integrated with the overlap calculation function, which can conveniently calculate the mode excitation efficiency and junction loss.

### (4) Adiabatic conditions - Lumerical EME

For the length design of each tapered waveguide, we use the eigenmode expansion (EME) module in the Lumerical Mode Solution. The advantage is that it is not necessary to recalculate the mode distribution of each cross-sectional cell when changing the tapered waveguide length, so the mode conversion efficiency can be verified extremely quickly. And the transmission field distribution and S-matrix can also be obtained to determine the crosstalk.

### (5) Transmission - Lumerical var-FDTD

For device transmission field analysis or bandwidth analysis, we rarely use 3D-FDTD in the design process, because its simulation consumes too many resources. Therefore, the 2.5D variational FDTD (var-FDTD) simulation in Lumerical Mode Solution is better. On the one hand, its calculation result is very close to 3D-FDTD, but its simulation time is greatly shortened; on the other hand, increasing the wavelength range or wavelength resolution of the light source will add little to the simulation time.

# Acknowledgement

From the first time I landed in Japan three years ago to the successful completion of my doctoral dissertation now, I have gained a lot in my academic life in the past three years. As an important stage in my life, I have been very fortunate to have met many friendly and knowledgeable professors, colleagues, and friends. Their unwavering support, guidance, and encouragement have been invaluable to me, and I would like to express my heartfelt gratitude to all those who have been instrumental in the completion of my doctoral research.

First and foremost, I extend my deepest appreciation to my supervisors, Prof. Shoji and Prof. Mizumoto, for their outstanding mentorship, patience, and expertise. I am truly grateful for the opportunities they provided me to join a leading laboratory and conduct cutting-edge research. Their rigorous attitude, innovative thinking, and persistent research are the benchmarks for me as both a researcher and an individual.

Improvement of the final quality of this dissertation would also like to thank the reviewers Prof. Nishiyama, Prof. Nakagawa, Prof. Uenohara, Prof. Miyamoto, and Prof. Saitoh. Thanks for their constructive comments and suggestions and their precious time.

Due to the coronavirus that lasted for several years, the collective activities in the laboratory have decreased in the past three years, but the help of my group members has not decreased. Thanks to experienced senior members Hara, Yajima, Neranjith, Mario, and Murai, who guided me in the experimental method when I first entered the laboratory; Thanks to Yokoi, Tange, Taniguchi, and Minemura who have similar research direction to me and helped me conduct many experiments; I would also like to thank Sato, Shimotsu, Chihara and Tsuchiya for providing an enriching and collaborative research environment. Finally, I also want to acknowledge the long-term company in life and work of Tong, Ni, Liang, and Wang who are also from China. They have provided a lot of help to me who is not fluent in Japanese, and they also accompanied me to spend many unforgettable spare time around Japan. I firmly

believe that even after graduation, we will be lifelong friends.

To my dear girlfriend Shen, whose constant understanding and encouragement have been a source of strength for keeping me motivated during the challenging times of this doctoral pursuit. Congratulations to you as well for successfully obtaining your degree.

My heartfelt thanks to my mother for her unwavering support and trust. The unexpected three-year-long absence finally paid off.

*衷心感谢母亲坚定不移的支持和信任*

Lastly, I would like to extend my appreciation to all the professors, mentors, colleagues, and friends who have played a role, no matter how small, in shaping my academic and personal growth. Your support has left an indelible mark on my life, and

*I am forever grateful.*

# List of publication

## Journal Papers

1. **Liu S.**, Minemura D. and Shoji Y., "Silicon-based integrated polarization-independent magneto-optical isolator." *Optica* 10.3 (2023): 373-378. DOI: 10.1364/OPTICA.483017
2. Liang Z., **Liu S.** and Shoji Y., "Improvement of extinction in optically-controlled silicon thermo-optic switch based on micro-ring resonator with distinct probe signal." *Japanese Journal of Applied Physics* 62.3 (2023): 032001. DOI: 10.35848/1347-4065/acbc5d
3. **Liu S.**, Shoji Y. and Mizumoto T., "TE-mode magneto-optical isolator based on an asymmetric microring resonator under a unidirectional magnetic field." *Optics Express* 30.6 (2022): 9934-9943. DOI: 10.1364/OE.454751
4. **Liu S.**, Shoji Y. and Mizumoto T., "Mode-evolution-based TE mode magneto-optical isolator using asymmetric adiabatic tapered waveguides." *Optics Express* 29.15 (2021): 22838-22846. DOI: 10.1364/OE.427914
5. Minemura D., **Liu S.**, Shoji Y. and Mizumoto T., "Polarization coupler for polarization-rotating Mach-Zehnder interferometer." *IEICE Electronics Express* 18.10 (2021): 20210176-20210176. DOI: 10.1587/elex.18.20210176

## Conference Paper

6. Minemura D., **Liu S.**, Shoji Y. and Mizumoto T., "Tunable Mode Converter Based on Mach-Zehnder Interferometer." 2021 26th Microoptics Conference (MOC). IEEE, 2021. DOI: 10.23919/MOC52031.2021.9598090

## Oral Presentations

7. **Liu S.** and Shoji Y., "TE-mode Magneto-optical Isolator Based on An Asymmetric Microring." JSAP-Optica Joint Symposia. Optica Publishing Group, 2022.
8. **Liu S.**, Shoji Y. and Mizumoto T., "Silicon-based Integrated TE Mode Magneto-optical Isolator." JSAP-OSA Joint Symposia. Optical Society of America, 2021.

## Poster

9. **Liu S.**, Shoji Y. and Mizumoto T., “Silicon-based integrated high-performance TE mode magneto-optical isolator,” International Symposium on Photonics and Electronics Convergence (ISPEC), 2021.